

2012/2 vol.9



ACTA GEO TECHNICA SLOVENICA

2012/2

s. Lenart et al.

SOIL LIQUEFACTION IN THE TONE RIVER BASIN DURING THE 2011 EARTHQUAKE OFF THE PACIFIC COAST OF TOHOKU

M. sazzad & K. Suzuki

A COMPARISON BETWEEN CONVENTIONAL TRIAXIAL AND PLANE-STRAIN COMPRESSION ON A PARTICULATE SYSTEM USING 3D DEM

I. Ikhza & H. F. Schweiger

NUMERICAL MODELING OF FLOATING PREFABRICATED VERTICAL DRAINS IN LAYERED SOIL

M. R. zareifard & Ahmad Rahimifar

A NEW SOLUTION FOR SHALLOW AND DEEP TUNNELS BY CONSIDERING THE GRAVITATIONAL LOADS

K. toufik & M. bachir

PROBABILISTIC STUDY OF THE PHENOMENON OF CRUSHED GRAINS USING THE MODEL OF WEIBULLS

B. jha & D. N. Singh

ZEOLITIZATION CHARACTERISTICS OF FLY ASHES FROM WET- AND DRY- DISPOSAL SYSTEMS

ISSN 1854-0171

ustanovitelji **founders**

Univerza v Mariboru, Fakulteta za gradbeništvo
University of Maribor, Faculty of Civil Engineering

Univerza v Ljubljani, Fakulteta za gradbeništvo in geodezijo
University of Ljubljana, Faculty of Civil and Geodetic Engineering

Univerza v Ljubljani, Naravoslovnotehniška fakulteta
University of Ljubljana, Faculty of Natural Sciences and Engineering

Slovensko geotehniško društvo
Slovenian Geotechnical Society

Društvo za podzemne in geotehniške konstrukcije
Society for Underground and Geotechnical Constructions

izdajatelj **publisher**

Univerza v Mariboru, Fakulteta za gradbeništvo
University of Maribor, Faculty of Civil Engineering

odgovorni urednik **editor-in-chief**

Ludvik Trauner University of Maribor

uredniki **co-editors**

Bojana Dolinar	University of Maribor
Borut Macuh	University of Maribor
Stanislav Škrabl	University of Maribor
Helena Vrecl Kojc	University of Maribor
Damijana Zlatolas	University of Maribor
Bojan Žlender	University of Maribor

posvetovalni uredniki **advisory editors**

Darinka Battelino	University of Trieste
Heinz Brandl	Vienna University of Technology
Chandrakant. S. Desai	University of Arizona
Pedro Seco e Pinto	National Laboratory of Civil Engineering

lektor **proof-reader**

Paul McGuinness

naklada **circulation**

300 izvodov - issues

cena **price**

25 EUR/izvod - 25 EUR/issue; (50 EUR for institutions/za institucije)

tisk **print**

Tercia tisk d.o.o. Ptuj

Revija redno izhaja dvakrat letno. Članki v reviji so recenzirani s strani priznanih mednarodnih strokovnjakov. Baze podatkov v katerih je revija indeksirana: SCIE - Science Citation Index Expanded, JCR - Journal Citation Reports / Science Edition, ICONDA - The international Construction database, GeoRef. Izid publikacije je finančno podprla Javna agencija za knjigo Republike Slovenije iz naslova razpisa za sofinanciranje domačih periodičnih publikacij.

uredniški odbor **editorial board**

József Farkas	Budapest University of Technology and Economics
Theodoros Hatzigogos	Aristotle University of Thessaloniki
Rolf Katzenbach	Technical University Darmstadt
Nasser Khalili	The University of New South Wales, Sydney
Zlatko Langof	University of Sarajevo
Jakob Likar	University of Ljubljana
Janko Logar	University of Ljubljana
Bojan Majes	University of Ljubljana
Milan Maksimović	University of Belgrade
Borut Petkovšek	Slovenian National Building and Civil Engineering Institute
Mihael Ribičič	University of Ljubljana
César Sagaseta	University of Cantabria
Patrick Selvadurai	McGill University
Stephan Semprich	University of Technology Graz
Devendra Narain Singh	Indian Institute of Technology, Bombay
Abdul-Hamid Soubra	University of Nantes
Kiirchi Suzuki	Saitama University
Antun Szavits-Nossan	University of Zagreb
Ivan Vaniček	Czech Technical University in Prague
Jianhua Yin	The Hong Kong Polytechnic University

naslov uredništva **address**

ACTA GEOTECHNICA SLOVENICA
Univerza v Mariboru, Fakulteta za gradbeništvo
Smetanova ulica 17, 2000 Maribor, Slovenija
Telefon / Telephone: +386 (0)2 22 94 300
Faks / Fax: +386 (0)2 25 24 179
E-pošta / E-mail: ags@uni-mb.si

spletni naslov **web address**

<http://www.fg.uni-mb.si/journal-ags/>

The journal is published twice a year. Papers are peer reviewed by renowned international experts. Indexation data bases of the journal: SCIE - Science Citation Index Expanded, JCR - Journal Citation Reports / Science Edition, ICONDA - The international Construction database, GeoRef. The publication was financially supported by Slovenian Book Agency according to the Tender for co-financing of domestic periodicals.

VSEBINA

2	Ludvik Trauner UVODNIK
4	stanislav Lenart in drugi UTEKOČINJENJE TAL V POREČJU REKE TONE MED POTRESOM OB VZHODNI OBALI JAPONSKE 2011
16	md. Mahmud sazzad in kiichi suzuki PRIMERJAVA MED OBIČAJNIM TRIOSNIM IN RAVNINSKO-DEFORMACIJSKIM STISKANJEM V POSEBNEM SISTEMU S 3D MDE
24	ikhya ikhya and helmut f. schweiger NUMERIČNO MODELIRANJE PLAVAJOČIH MONTAŽNIH NAVPIČNIH DRENAŽ V VEČPLASTNI ZEMLJINI
36	mohammad a. zareifard in ahmad fahimifar NOV NAČIN ANALIZIRANJA PLITKIH IN GLOBO- KIH TUNELOV OB UPOSTEVANJU GRAVITACIJE
50	kheffache toufik in melbouci bachir VERJETNOSTNA ŠTUDIJA POJAVA DROBLJENJA ZAN PO METODI WEIBULL
62	ghagwanjee jha in d. n. singh ZEOLITIZACIJA ELEKTROFILTRSKEGA PEPELA PRI ODSTANJEVANJU PO MOKREM IN SUHEM POSTOPKU
76	SKUPNI DOKTORSKI PROGRAM GEOINŽENIARSTVO IN UPRAVLJANJE Z VODAMI
86	NAVODILA AVTORJEM

CONTENTS

Ludvik Trauner EDITORIAL	3
stanislav Lenart et al. SOIL LIQUEFACTION IN THE TONE RIVER BASIN DURING THE 2011 EARTHQUAKE OFF THE PACIFIC COAST OF TOHOKU	5
md. Mahmud sazzad & kiichi suzuki A COMPARISON BETWEEN CONVENTIONAL TRI- AXIAL AND PLANE-STRAIN COMPRESSION ON A PARTICULATE SYSTEM USING 3D DEM	17
ikhya ikhya and helmut f. schweiger NUMERICAL MODELING OF FLOATING PREFABRI- CATED VERTICAL DRAINS IN LAYERED SOIL	25
mohammad a. zareifard & ahmad fahimifar A NEW SOLUTION FOR SHALLOW AND DEEP TUNNELS BY CONSIDERING THE GRAVITATIONAL LOADS	37
kheffache toufik & melbouci bachir PROBABILISTIC STUDY OF THE PHENOMENON OF CRUSHED GRAINS USING THE MODEL OF WEIBULLS	51
ghagwanjee jha & d. n. singh ZEOLITIZATION CHARACTERISTICS OF FLY ASHES FROM WET- AND DRY- DISPOSAL SYSTEMS	63
JOINT DOCTORAL PROGRAM GEO-ENGINEERING AND WATER MANAGEMENT	76
INSTRUCTIONS FOR AUTHORS	87

UVODNIK

Cenjene bralce mednarodne revije Acta Geotechnica Slovenica (AGS) z velikim veseljem obveščamo, da smo dne 28. novembra 2012 svečano odprli novi Skupni doktorski program Geoinženirstvo in upravljanje z vodami (JPhD:GE-WM), ki ga bodo skupaj izvajale Tehnična univerza v Gradcu (TUG), Univerza v Zagrebu (UZ), Univerza v Mariboru (UM) in Tehnična univerza v Budimpešti (TUB). Pobudo za ustanovitev (JPhD:GE-WM) so dali profesorji: dr. Harald Kainz (TUG), dr. Božidar Biondić (UZ) in dr. Ludvik Trauner (UM). Ideja o sodelovanju se je rodila pri skupnem raziskovalnem projektu «K-net Wasser» med Gradcem (Avstrija), Varaždinom (Hrvaška) in Mariborom (Slovenija). Posebna predavanja JPhD:GE-WM se bodo izvajala dvakrat letno po 1 mesec na skupnih delavnicah v februarju in juliju.

Informacije o JPhD:GE-WM so podane na zadnji strani te revije oz. tudi dostopne na spletni strani: www.jdp.tugraz.at.

V tej številki objavljamo 6 znanstvenih prispevkov:

V prvem članku avtorji, Stanislav Lenart, Junichi Koseki in Yukika Miyashita, poročajo o primerih utekočinjenja tal v porečju reke Tone zaradi potresa ob vzhodni obali Japonske leta 2011. Predstavljeni so primeri pojava peščenih vrelcev, poškodbe na rečnih nasipih, posedki in nagibanja objektov, dvizki lahkih podzemnih objektov in bočno razziranje površja. Vsebino članka je dr. Stanislav Lenart, kot vabljeni predavatelj, uspešno predstavil na letošnjih 13. Šukljjetovih dnevih (Lipica, 14.–15. junij 2012).

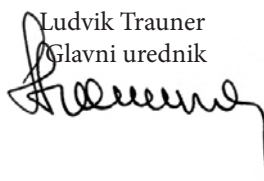
V drugem članku sta avtorja, Md. Mahmud Sazzad in Kiichi Suzuki, primerjala obnašanje sipkih materialov v pogojih običajne triosne stisljivosti (OTS) in ravninsko napetostno-deformacijske stisljivosti (RNS) z uporabo 3D metode ločilnih elementov (MLE). Z uporabo periodičnih robov je bilo iz 8000 delcev numerično pripravljenih enakosmerno stisljivih vzorcev. S tem vzorcem so bili simulirani OTS in RNS preizkusi s ciljem primerjanja in preučevanja makro- in mikro-mehanskega odziva sipkega materiala, pri čemer začetne teksture numeričnega vzorca niso bile spremenjene. Simulirani napetostno-deformacijski odzivi so kvalitativno v skladu z odzivi iz eksperimentalnih študij.

V tretjem članku sta avtorja, Ikhya Ikhya in Helmut F. Schweiger, prikazala primerjavo terenskih meritev in numerični model posedanja nasipov na mehki zemljini v okviru indonezijskega projekta Cirebon Power Plant, kjer so bile nameščene montažne vertikalne drenaže (MVD). Za določitev optimalne penetracijske globine namestitve drenaž so bile z numeričnim modelom preučene plavajoče MVD v dvo-plastnih zemljinah pri pogojih dreniranja v eni in obeh plasteh.

V četrtem članku avtorja, Mohammad Reza Zareifard in Ahmad Fahimifar, predstavljata novo analitično-numerično rešitev za krožni tunel v deformacijsko popuščajoci in Hoek-Brownovi skali, ob upoštevanju pogojev osne simetrije. Izpeljani so izrazi za določitev sprememb začetne napetosti in robnih pogojev površine tal v različnih smereh okrog tunela.

V petem članku sta avtorja, Kheffache Toufik in Melbouci Bachir, izdelala eksperimentalno študijo drobljenja posameznih zrn apnenca ter večzrnatih vzorcev, ki so bili podvrženi eno-osni obremenitvi, s čimer se je ugotovilo vpliv obremenitve in velikosti zrn na odnos lomljenja. S statistično metodo Weibull je problem modeliran in določen je odnos lomljenja za oba primera.

V šestem članku sta avtorja, Bhagwanjee Jha in D. N. Singh, preučevala fizikalne, kemične, mineraloške in morfološke lastnosti usedlin elektrofiltrskega pepela, zbranega v usedalnih bazenih in silosih termoelektrarne po hidrotermalni obdelavi. Preiskava z okoljskim vrstičnim elektronskim mikroskopom in rentgenska difrakcijska analiza usedlin sta pokazali, da ima pepel v silosu izredno dobro kationsko izmenjavo in visoko razmerje $\text{SiO}_2/\text{Al}_2\text{O}_3$ (SAR), kar ustreza tvorjenju večjih zeolitov elektrofiltrskega pepela v primerjavi z mokrim postopkom.

Ludvik Trauner
Glavni urednik


EDITORIAL

Dear readers of the international journal Acta Geotechnica Slovenica (AGS), we are pleased to announce that on November 28th 2012 we inaugurated the new interdisciplinary Joint Doctoral Program: Geo-Engineering and Water Management (JPhD:GE-WM) which will be implemented jointly by the Technical University of Graz (TUG), University of Zagreb (UZ), University of Maribor (UM) and the Technical University of Budapest (TUB). The initiative to establish (JPhD: GE-WM) came from professors: dr. Harald Kainz (TUG), dr. Božidar Biondić (UZ) and dr. Ludvik Trauner (UM). The idea for this collaboration was born in a research project between Graz (Austria), Varaždin (Croatia) and Maribor (Slovenia) within the research network "K-net Wasser". Specialised courses at the PhD level will be offered in the Joint Schools. Joint Schools JPhD:GE-WM will be offered twice a year in February and July, and they will last for 1 month each.

More information about the JPhD:GE-WM can be found on the last page of this journal and on the website: www.jdp.tugraz.at

In this issue we have published six scientific contributions:

In the first article, the authors Stanislav Lenart, Junichi Koseki and Yukika Miyashita present a brief report of the liquefaction damage in the Tone river basin caused by the 2011 earthquake off the Pacific coast of Tohoku. It includes sand boiling, damage to the river's dikes, settlement and tilt of superstructures, uplift of light underground structures and lateral spreading. The content of this article was successfully presented as an invited lecture by dr. Stanislav Lenart at the 13th Lujo Šuklje Memorial Day (Lipica, 14–15 June 2012).

In the second article, the authors Md. Mahmud Sazzad and Kiichi Suzuki aim at comparing the behavior of granular materials under conventional triaxial compression (CTC) and plane-strain compression (PSC) conditions using a 3D discrete-element method. An isotropically compressed, dense sample consisting of 8000 spheres was prepared numerically using the periodic boundaries. CTC and PSC tests were simulated using the same isotropically compressed dense sample to compare and explore the macro- and micro-mechanical responses of granular materials without any bias from the initial fabric of the numerical sample. Qualitatively, the simulated stress-strain responses are consistent with that observed in the experimental studies.

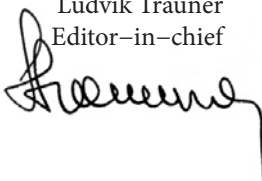
In the third article, the authors Ikhya Ikhya and Helmut F. Schweiger present a comparison of field measurements and a numerical model of the settlements based on the construction of an embankment on soft soil for the Cirebon Power Plant Project in Indonesia, where prefabricated vertical drains (PVDs) were installed. In the numerical model, floating PVDs in two soil layers for two- and one-way drainage conditions are examined in order to determine the optimum penetration depth.

In the fourth article, by Mohammad Reza Zareifard and Ahmad Fahimifar, a new elasto-plastic analytical-numerical solution, considering the axial-symmetry condition, for a circular tunnel excavated in a strain-softening and Hoek–Brown rock mass is presented. To examine the effect of the initial stress variations, and also the boundary conditions at the ground surface, the formulations are derived for different directions around the tunnel.

In the fifth article, the authors Kheffache Toufik and Melbouci Bachir present the results of an experimental study made on the crushing of individual grains of limestone and samples consisting of multiple grains subjected to a uniaxial loading in order to highlight the influence of the loading and the grain size on the rate of crushing. A statistical study using the Weibull method allowed us to model the problem and quantify the rate of breakage for the two cases.

In the sixth article, by Bhagwanjee Jha and D. N. Singh, investigations were conducted to study the physical, chemical, mineralogical and morphological characteristics of the residues of fly ashes, collected from the lagoons and hoppers of the same thermal power plant, after their hydrothermal treatment. Field-emission-gun scanning electron microscopy and X-ray diffraction analyses of these residues, demonstrate that the hopper ash attains an exceptionally higher cation-exchange capacity and $\text{SiO}_2/\text{Al}_2\text{O}_3$ ratios, which correspond to the formation of major fly-ash zeolites, as compared to its counterpart.

Ludvik Trauner
Editor-in-chief



UTEKOČINJENJE TAL V POREČJU REKE TONE MED POTRESOM OB VZHODNI OBALI JAPONSKE 2011

STANISLAV LENART, JUNICHI KOSEKI IN YUKIKA MIYASHITA

o avtorjih

Stanislav Lenart
Zavod za gradbeništvo Slovenije
Dimičeva 12, 1000 Ljubljana, Slovenia
e-pošta: stanislav.lenart@zag.si

Junichi Koseki
Institute of Industrial Science (IIS), The University of Tokyo
4-6-1 Komaba, Meguro-ku, Tokyo, Japonska
e-pošta: koseki@iis.u-tokyo.ac.jp

Yukika Miyashita
Institute of Industrial Science (IIS), The University of Tokyo
4-6-1 Komaba, Meguro-ku, Tokyo, Japonska
e-pošta: ymiya@iis.u-tokyo.ac.jp

izvleček

Članek na kratko poroča o primerih utekočinjenja tal v porečju reke Tone zaradi potresa ob vzhodni obali Japonske leta 2011. Predstavljeni so primeri pojava kipčih peskov, poškodbe na rečnih nasipih, posedki in nagibanja objektov, dvižki lahkih podzemnih objektov in bočno razrivanje površja. Za lažje razumevanje vzrokov pojava velikega števila primerov utekočinjenja tal na melioriranih področjih, je na kratko predstavljena zgodovina poteka melioracij ob reki Tone. V članku so presojani zapisi premikov tal na območju reke. Izvedena je njihova primerjava s premiki iz območij bližje žarišču potresa. Prispevek razpravlja tudi o vplivih lokacije in sestavi tal na največje pospeške temeljnih tal.

ključne besede

potres ob vzhodni obali Japonske 2011, utekočinjenje, študija primera

SOIL LIQUEFACTION IN THE TONE RIVER BASIN DURING THE 2011 EARTHQUAKE OFF THE PACIFIC COAST OF TOHOKU

STANISLAV LENART, JUNICHI KOSEKI and YUKIKA MIYASHITA

about the authors

Stanislav Lenart
Slovenian National Building and Civil Engineering Institute (ZAG)
Dimičeva 12, 1000 Ljubljana, Slovenia
(formerly IIS, The University of Tokyo)
E-mail: stanislav.lenart@zag.si

Junichi Koseki
Institute of Industrial Science (IIS), The University of Tokyo
4-6-1 Komaba, Meguro-ku, Tokyo, Japan
E-mail: koseki@iis.u-tokyo.ac.jp

Yukika Miyashita
Institute of Industrial Science (IIS), The University of Tokyo
4-6-1 Komaba, Meguro-ku, Tokyo, Japan
E-mail: ymiya@iis.u-tokyo.ac.jp

abstract

A brief report about the liquefaction damage in the Tone river basin, caused by the 2011 earthquake off the Pacific coast of Tohoku, is presented. It includes sand boiling, damage to river dikes, the settlement and tilt of super-structures, the uplift of light underground structures and lateral spreading. A history of land reclamation along the Tone river is briefly presented to understand why extensive liquefaction took place predominantly in reclaimed land. The recorded ground motions near the river were analyzed

and compared to near-source ground motions. The effects of the site location and the ground conditions during the peak ground acceleration are discussed.

keywords

2011 earthquake off the Pacific coast of Tohoku, liquefaction, case history

1 INTRODUCTION

HISTORY OF TONE RIVER BASIN

The Tone river (in Japanese, Tone-gawa) originates in the volcanic area of the northwestern Kanto region and flows approximately 320 km southeast, crosses the Kanto Plain with the Tokyo Metropolitan area, and finally enters the Pacific Ocean at Choshi City. No other river in Japan has been so modified by human activity [1]. Its course has been altered and its entire length is confined by dikes. The ancient Tone river flowed to Tokyo Bay; however, its course was diverted to the Pacific Ocean during the 17th century (Fig. 1). Although the main purpose of the project was to protect the capital of Japan, Tokyo, from floods, there have been infinitely many floods in the rest of river basin since then.



Figure 1. Eastward diversion of Tone river (modified from [2]): original course (left) and diverted course (right).

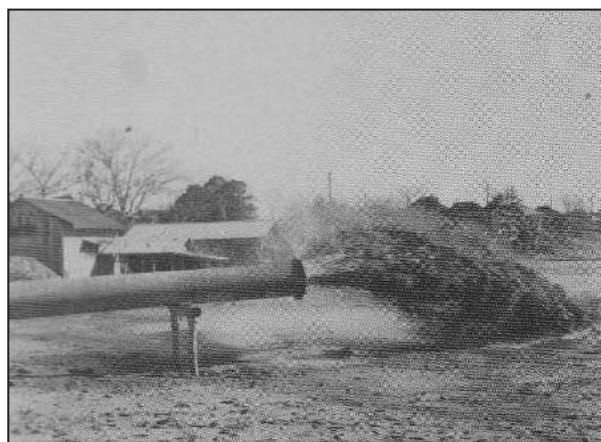


Figure 2. "Kirisho-numa" swamp (left) and its reclamation using dredged soils (right) [3].

One of the floods caused the breaching of the Tone river dike near Fusa, Abiko city in Chiba prefecture in 1870 [2]. The embankment for controlling the waters of the river collapsed over a length of more than 80 m and submerged the whole Fusa area. A large swamp called "Kirisho-numa" with an area of more than 5 ha was created. This area suffered from frequent flood disasters. Therefore, a project to improve the Tone river channel and the dike was initiated in 1952. The dredged soil was transported through pipes to reclaim the swamp. Finally, the reclaimed area was converted into a residential area. The "Kirisho-numa" swamp and the process of its reclamation using dredged soils are shown in Fig. 2.

2011 EARTHQUAKE OFF THE PACIFIC COAST OF TOHOKU

One of the world's largest recorded earthquakes in history, with a moment magnitude $M_w = 9.0$, occurred and affected the east part of Japan on the 11th of March 2011 at 14:46 local time. It was caused by tectonic movements of the North American plate and the Pacific plate. The Geospatial Information Authority of Japan [4] constructed a fault model using co-seismic, surface-displacement data observed by the GPS Earth Observation Network System. A fault model that consists of two rectangular faults with a uniform slip in an elastic half-space shows that the total major rupture length reached approximately 380 km with a fault width of 90-130 km. The slip amounts of the northern and southern segments were estimated to be ~25 m and ~6 m, respectively [4].

Fig. 3 shows the surface displacements caused by the main shock. A star indicates the epicenter of an earthquake. Two rectangular faults were assumed. The circles indicate the epicenters of the aftershocks determined until the 15th of March. There have been 408 aftershocks

with a magnitude of 5.0 or above up until the 15th of March at 5 p.m. [5], indicating a tendency of tectonic plates and faults to stabilize ground conditions, which have been greatly altered by the earthquake.

The existence of two faults might be proved by the near-source acceleration waveforms. Two remarkable distinct phases of ground motion can be seen on the earthquake ground-motion records from seismographs in the north part of Honshu island [6], which are the closest to the epicenter, while on the acceleration waveforms recorded in the south, in the Tone river basin, the first phase is not visible at all (Fig. 6).

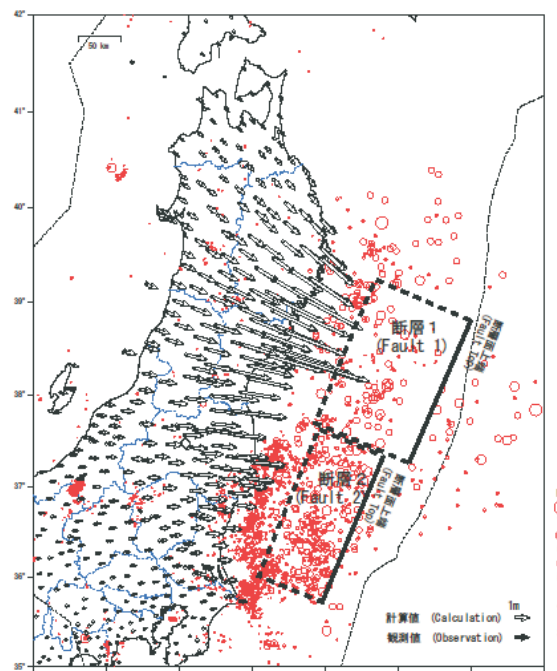


Figure 3. Calculated and observed co-seismic horizontal surface displacements [4].

2 GROUND-MOTION CHARACTERISTICS DURING THE 2011 EARTHQUAKE OFF THE PACIFIC COAST OF TOHOKU

THE EFFECT OF SITE LOCATION

Although the damage due to the great Tohoku earthquake occurred at many places on the east part of Honshu island, only five typical sites with liquefaction occurrence in the Tone river basin are presented in this paper. Their locations are shown in Fig. 4b. Fig. 4a presents the overall location of the earthquake's hypocenter, the Tone river basin and the seismographs, the records of which are discussed in this paper.

To understand the transfer of ground shaking from near-source to more distant sites, we compare the earthquake motion records from six sites of the Japanese seismograph network. The seismographs CHB004, IBR016, MYG004 and MYG010 are part of K-NET, a Japanese,

nation-wide, strong-motion seismograph network. They are all installed on the ground surface. Seismograph CHBH13 is part of KiK-net, a Japanese, strong-motion, seismograph network, which consists of pairs of seismographs installed in a borehole as well as on the ground surface. Basic data about these seismographs are listed in Table 1. Their location is shown in Fig. 4a and Fig. 4b.

It is evident from Table 1 that the levels of ground shaking recorded during the 2011 earthquake off the Pacific coast of Tohoku were very high and the values of the peak ground accelerations (PGAs) at some seismograph locations, e.g., $PGA \approx 3.0g$ at MYG 004, exceeded all reasonable expectations. It is difficult to explain such values, particularly as there was no extra damage observed on bridges or buildings in Tsukidate, where this record was made [8]. It is supposed that the design values of the PGAs less than $1.0g$ were used in the design. A detailed insight into the acceleration record shows a sharp spike. It might not be caused directly by seismic-induced ground motions, but by some other impacts that happened nearby (some banging) during the earthquake's

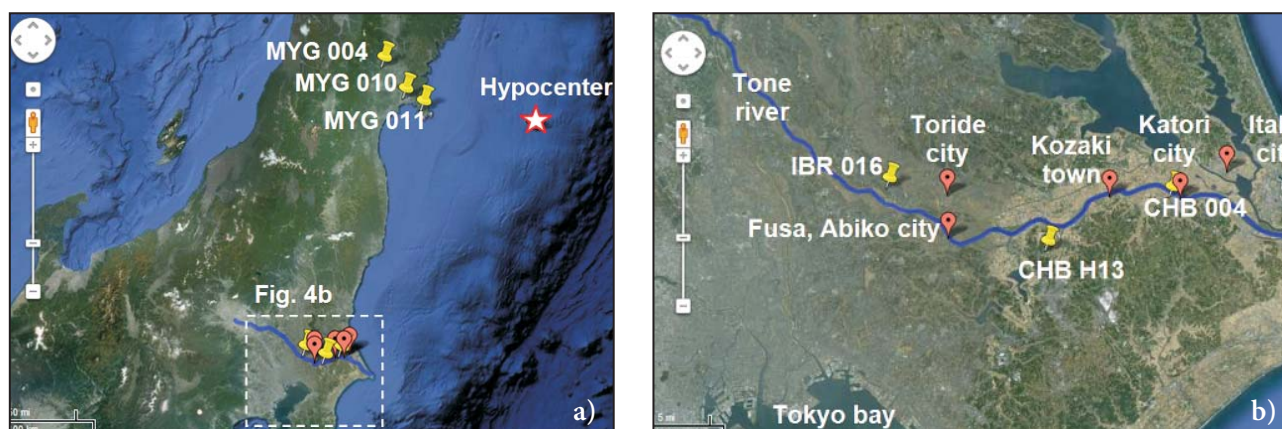


Figure 4. Map of the sites discussed in the paper (a) and their detailed locations (b) along the Tone river (modified from <http://maps.google.com>).

Table 1. Details about the K-NET and KiK-net seismographs [7].

Seismograph	Epicentral distance [km]	Altitude [m]	Peak acceleration* [cm/s ²]	Depth [m]	Base
CHB 004	323	13.9	300.7	surface	Ash clay, sandy soil
CHB H13	340	12	233.9	surface	sandstone, siltstone, mudstone and conglomerate (surface)
			56.9	1300	Chert (bedrock)
IBR 016	350	20.4	516.7	surface	Ash clay, sand
MYG 004	175	40	2699.9 (spike)	surface	Clay, rock
MYG 010	143	2	458.2	surface	Sand
MYG 011	121	13.2	921	surface	Rock

* maximum value of NS/EW components

duration. If this spike is eliminated the maximum PGA of this record is reduced by more than half.

The subsoil condition with a firm base in the cases of two extreme PGA values (MYG 004 and MYG 011) differs slightly from the subsoil conditions at the other discussed locations, where sandy soil is observed in the base. There is no evidence that this could be a reason for the sharp spike phenomenon in the case of MYG 004. Sharp spikes could also be caused by another kind of source, e.g., some banging near the instrument. In general, these kinds of spiky accelerations can be safely ignored as they do not allow sufficient time to cause large deformations. On the other hand, seismograph MYG 011 is located on a slope, suggesting possible topographical amplifications [9], while seismograph MYG 004 is located on flat ground.

Nevertheless, we can also observe high PGA values at all the other listed locations, on average almost 0.4g. It should be noted that the PGA at the near-source location (Miyagi prefecture) is comparable to

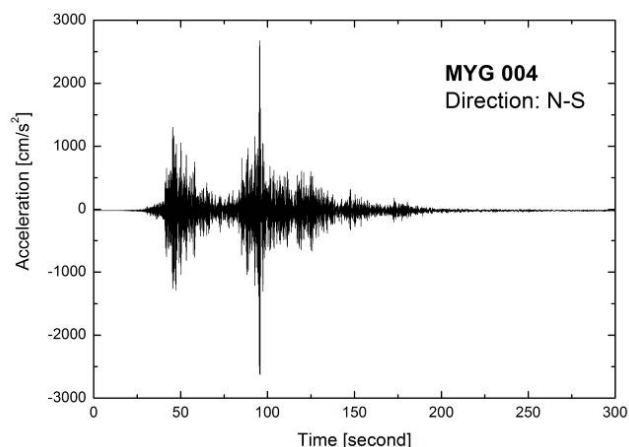


Figure 5. Ground-motion record with the largest observed peak ground acceleration $PGA=2699.9 \text{ cm/s}^2$ during to the 2011 earthquake off the Pacific coast of Tohoku, K-NET seismograph MYG 004.

the PGA recorded at the locations in the Tone river basin, although the epicentral distance in the case of the latter is almost twice as large as in the case of the

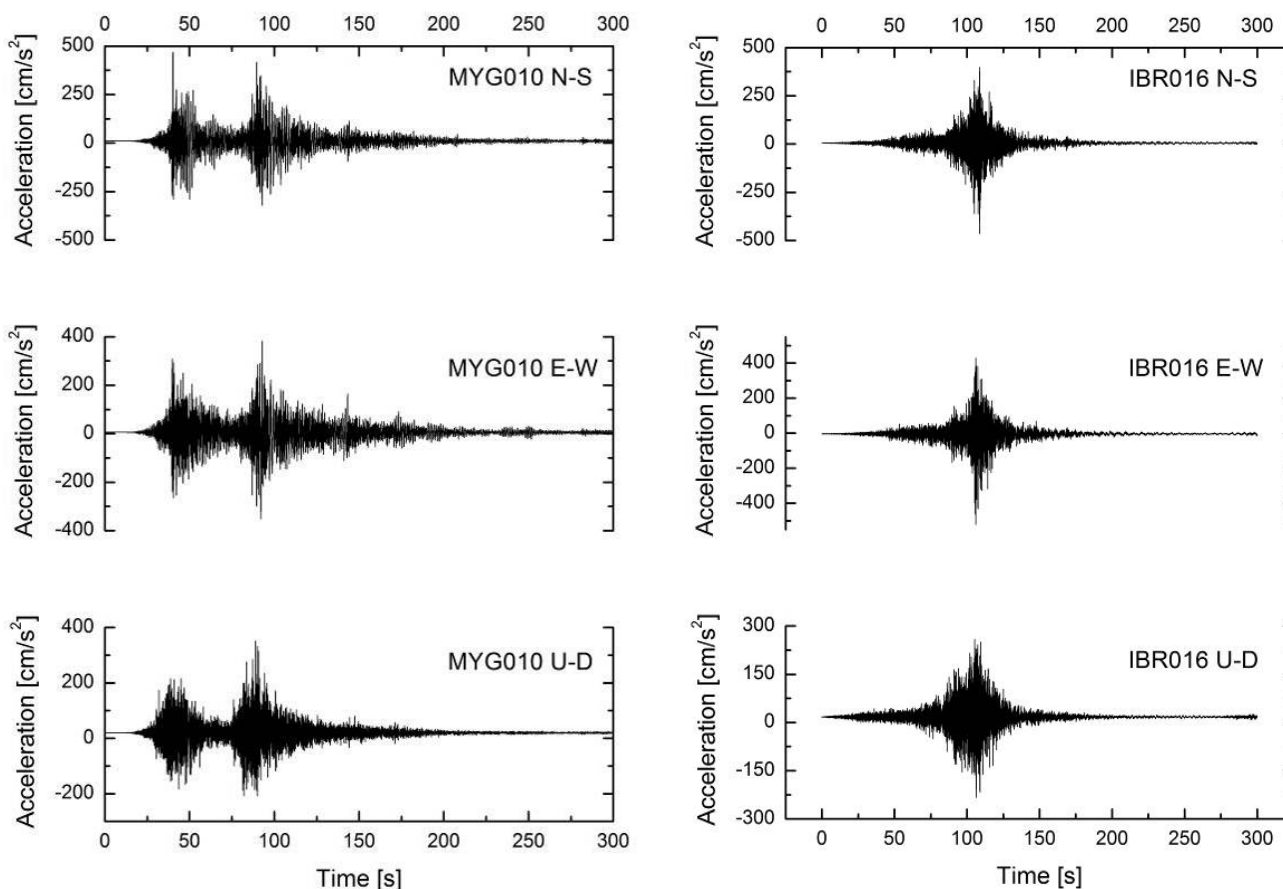


Figure 6. Ground-acceleration records at (left) the near-source K-NET seismograph (MYG 010) and (right) the K-NET seismograph near the Tone river (IBR 016).

Miyagi prefecture. One should refer to Fig. 3, where the assumed faults are shown. A similar distance to rupture is evident for both locations.

Spectral analyses of the ground acceleration records are shown in Fig. 7. It is clear that the dominant period ranges up to 2 s at the near-source sites in Miyagi prefecture, while the dominant frequency increases up to a period of nearly 0.2 s at sites near the Tone river.

THE EFFECT OF THE AMPLIFICATION OF MOTION IN THE SURFACE ALLUVIUM

Ground motion records at two selected K-NET stations and one selected KiK-net station near the Tone river do not differ a lot. The durations of the shakings were rather long, 100-200 s, suggesting that the soil was subjected to a large number of load reversals. The selected stations are located at soft alluvium soils with shear-wave velocities of less than 500 m/s in the upper 20 m. The soil profiles

are similar, consisting of sand or sandy soil covered by volcanic ash clay (Fig. 8). Considering the high level of ground water, as the Tone river is near, these ground conditions combined with a large number of load cycles are sufficient for triggering the liquefaction.

The seismograph CHBH13 is part of the KiK-net network, and the motion records at the surface and at the bedrock (1300 m deep) are available. Soil profile from deep borehole of seismograph CHBH13 is presented in Fig. 9, while Fig. 10 shows the effect of surface alluvium layers on the wave propagation. A clear amplification of the acceleration in the top soft soil layers can be seen. Results of spectral analysis of ground motion records at bedrock and surface are compared on Fig. 11. Besides the amplification, one can observe that surface record results dominant period close to 0.2 s which is very similar to those obtained in other locations near Tone river (Fig. 7), while slightly smaller dominant period ranges of nearly 0.1 s is achieved at the bedrock.

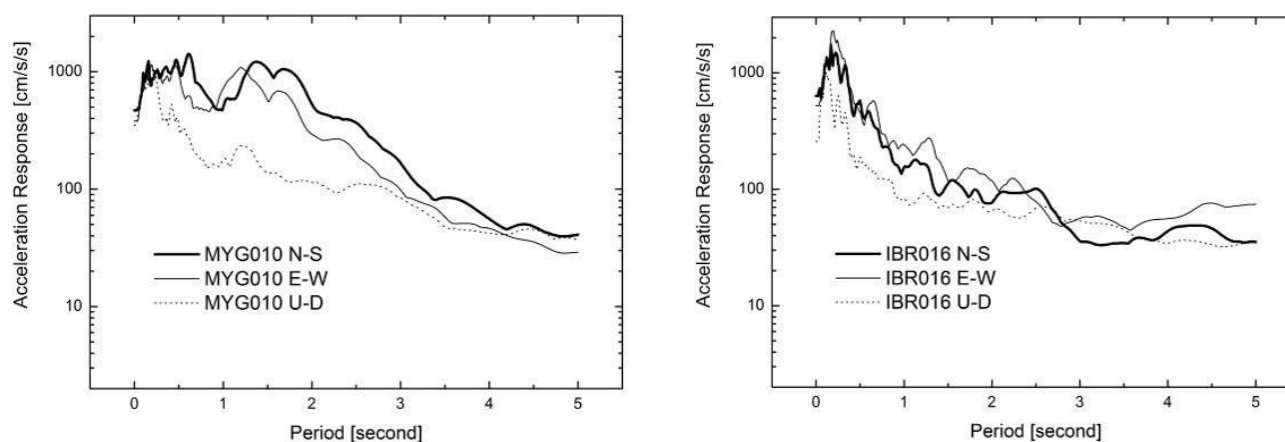


Figure 7. Spectral analysis of ground-motion data (5% damping) at (left) the near-source K-NET seismograph (MYG 010) and (right) the K-NET seismograph near the Tone river (IBR 016).

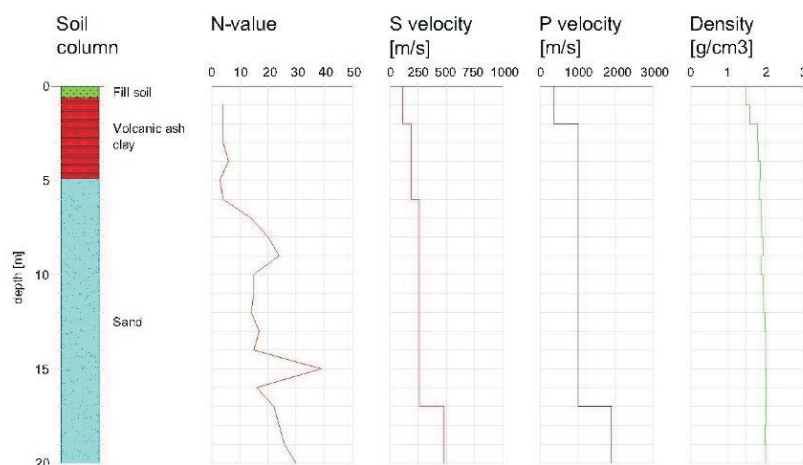


Figure 8. Typical shallow (20 m) soil profile along the Tone river, K-NET station IBR 016 (data from [7]).

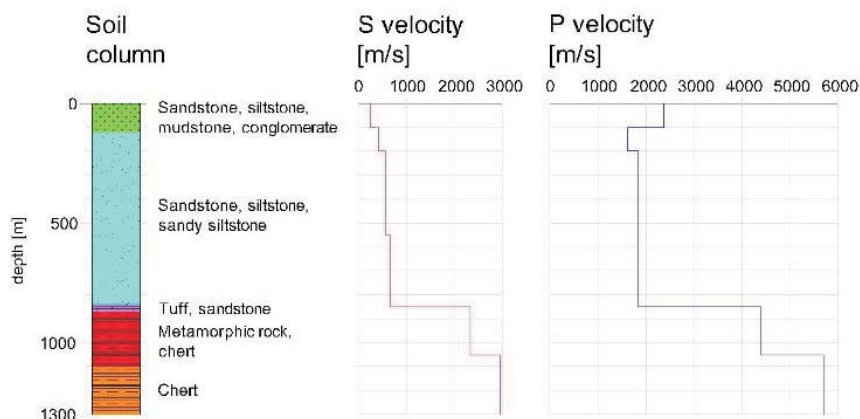


Figure 9. Soil profile from the deep borehole (1300 m) at the KiK-net station CHB H13 (data from [7]).

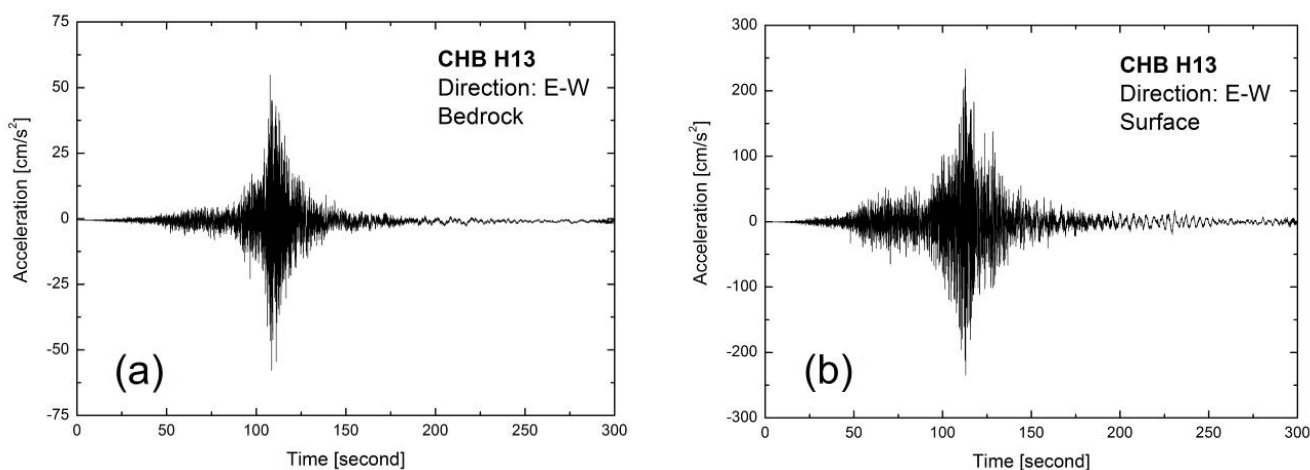


Figure 10. Amplification of ground motion as evidenced from (a) ground motion recorded at the bedrock and (b) ground motion recorded at the surface at CHB H13 location (KiK-net).

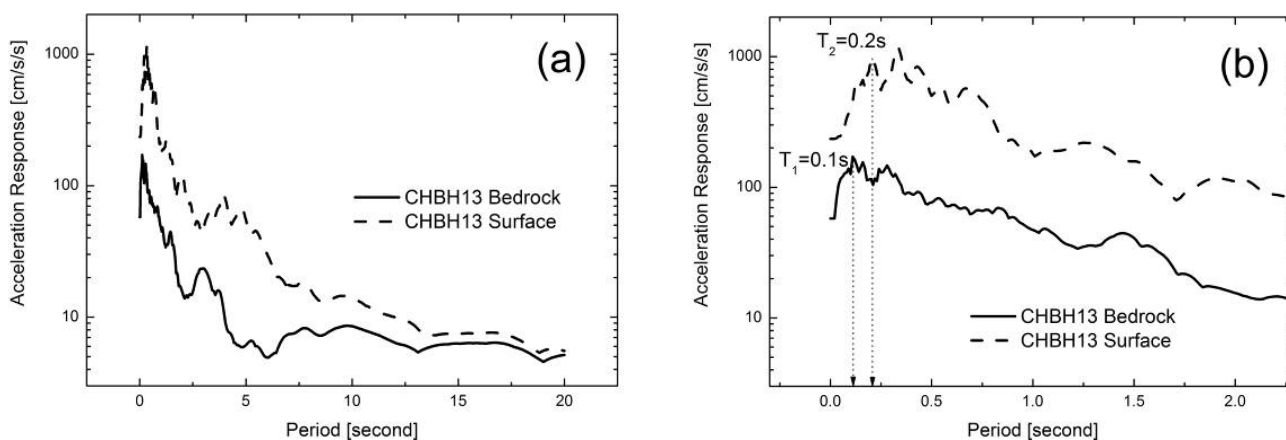


Figure 10. Comparison of the spectral analysis of ground motion data (5% damping) recorded at bedrock and surface at CHB H13 location: (a) overall and (b) close look (KiK-net).

3 LIQUEFACTION OCCURRENCE ALONG THE TONE RIVER AND ITS EFFECTS

The following photographs were taken during a post-earthquake survey [10, 11] at five sites (see Fig. 4) with liquefaction occurrence in the Tone river basin. The consequences of liquefaction are briefly described.

SAND BOILING

Sand boiling was observed almost everywhere that the liquefaction occurred. If the ground is covered by a less permeable layer, e.g., volcanic ash clay, small cracks or

channels are formed to dissipate the seismically induced, excess pore-water pressure. The water velocity was sufficient in cases presented in Fig. 12 to carry fine sand to silt soil particles to the surface. The gradation curves of the samples from several locations of sand boiling are presented in Fig. 18.

DAMAGE TO RIVER DIKES

The settlement and cracking of the Tone river dike occurred at many places, mostly due to the shear failure of the slope itself or the liquefaction of subsoil layers and/or a submerged part of the dike itself. The damaged dikes were temporarily rehabilitated against possible high water and protected against rainfall infiltration (Fig. 13).



Figure 12. Extensive sand boiling (a) at the rice field in Toride city and (b) between residential houses in Abiko city.



Figure 13. Extensive protection of the damaged Tone river dike (Sakae town) against rainfall.

SETTLEMENT AND TILT OF HEAVY STRUCTURES

Liquefaction-induced ground-surface settlements are caused by the volumetric strain that develops as a consequence of sand boiling and the re-consolidation of the liquefied soil layers. As superstructures with shallow foundations are often of asymmetric self-weight or subsoil conditions are not perfectly uniform, settlements might be accompanied by tilt (Fig. 14b). The average range of settlements noticed at the described sites was between 10 and 30 cm, but might be up to 1 m in some extreme cases (Fig. 14a).



UPLIFT OF LIGHT UNDERGROUND STRUCTURES

Many manholes, sewerage pipelines and other underground structures with small self-weight were popped out of the ground due to the upward buoyancy force generated by the liquefaction of the surrounding soil (Fig. 15). Based on the observed damage, we can see that good backfill material is needed to avoid the uplift of light underground structures due to the liquefaction of backfill material. Other kinds of countermeasures should be taken if this is not possible. Some sewage manholes have been protected by adding a mass to increase the self-weight, or adding a drainage capacity, among others.



Figure 14. Residential houses in Itako city settled (a) evenly or (b) with tilting.



Figure 15. Uplift of (a) pipeline in reclaimed land of Itako city and (b) underground tank in Kozaki town.



Figure 16. Lateral spreading with a maximum horizontal displacement of about 1 m in Katori city.

LATERAL SPREADING

Lateral flow occurs in the case of very gently sloped ground underlain by a liquefied layer, or a liquefied soil layer at the back of a quay wall or a revetment that undergoes a residual outward displacement. It was observed to a limited extent in some areas facing towards a river or pond (Fig. 16).

DIFFERENTIAL SETTLEMENTS

In general, superstructures supported on deep foundations, e.g., a pile foundation, in the case of important infrastructure, e.g., viaducts, bridges, and multi-storey buildings, performed well, even when the subsoil lique-



Figure 17. Settlements of the ground around buildings with deep foundations in Katori city.

fied. Many of these kinds of foundations were designed in Japanese practice by considering the possible effects of liquefaction. However, liquefaction-triggered uneven settlements of the surrounding ground caused a lot of damage to connecting pipes (Fig. 17).

4 DISCUSSION

As stated above, samples from sand boiling at several places were collected and their gradation curves were defined. They were compared to three European soils with an estimated liquefaction potential [12, 13, 14]. The results are all presented in Fig. 18. It is clear that the gradation curve of the Bostanj silty sand [13] fits very well with the gradation curves obtained from the sand-boiling samples, while gradations of other two soils noticeable differ from the gradation of sand-boiling samples.

We do not know the initial state of the liquefied soil layers. By analyzing the exact location of the liquefied sites from past earthquakes the reoccurrence of liquefaction was noticed on the same sites during the recent earthquake. Wakamatsu [15] reports that liquefaction took place to limited extents along the Tone river basin in the 1987 Chibaken-Toho-oki earthquake with a moment magnitude $M_w = 6.7$. This earthquake had a much closer epicenter with much smaller magnitude than the 2011 earthquake off the Pacific coast of Tohoku, thus the strong motion records were in general smaller than the ones recorded in 2011. As far it is known to the authors, there are no other records of previous liquefaction through the natural soil deposits in this area.

It is difficult to understand the existence of a liquefied site just next to a non-liquefied site, as shown in Fig. 19a in the case of Abiko city. Both of liquefied sites and non-liquefied sites were confirmed by the survey [11] and located on recent aerial photo (Fig. 19a). Their location was transformed from a current map into an old map, that was compiled based on survey results conducted in 1928 before the time of the reclamation of the "Kirishonuma" swamp (see Fig. 2) and the other swamps, the old river channels, etc., in the Tone river basin [2, 11]. The reclaimed land was later developed as residential area, where liquefaction occurred during the recent 2011 earthquake off the Pacific coast of Tohoku. From Fig. 19b it seems that the occurrence of liquefaction is greatly affected by the insufficient compaction of dredged soils during land reclamation.

5 CONCLUSION

The 2011 earthquake off the Pacific coast of Tohoku caused liquefaction, triggering on enormous number of sites along the Tone river. It induced damage to houses, lifeline facilities and river dikes. In general, good performance of the structures supported by deep foundations was observed.

Most of the sites affected by the liquefaction were reclaimed land, which used to be old river beds or swamps before the reclamation. Liquefaction reoccurrences were noticed during the recent earthquake on several sites when compared to the affected sites from previous earthquakes. The boiled sands were mostly fine sands, which could originate from the material dredged from the Tone river during the reclamation works.

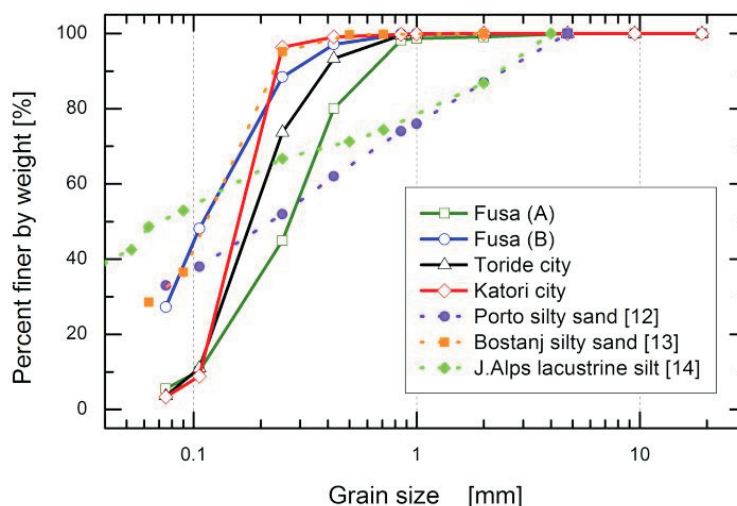


Figure 18. Gradation of samples retrieved from the sand-boiling sites near the Tone river.

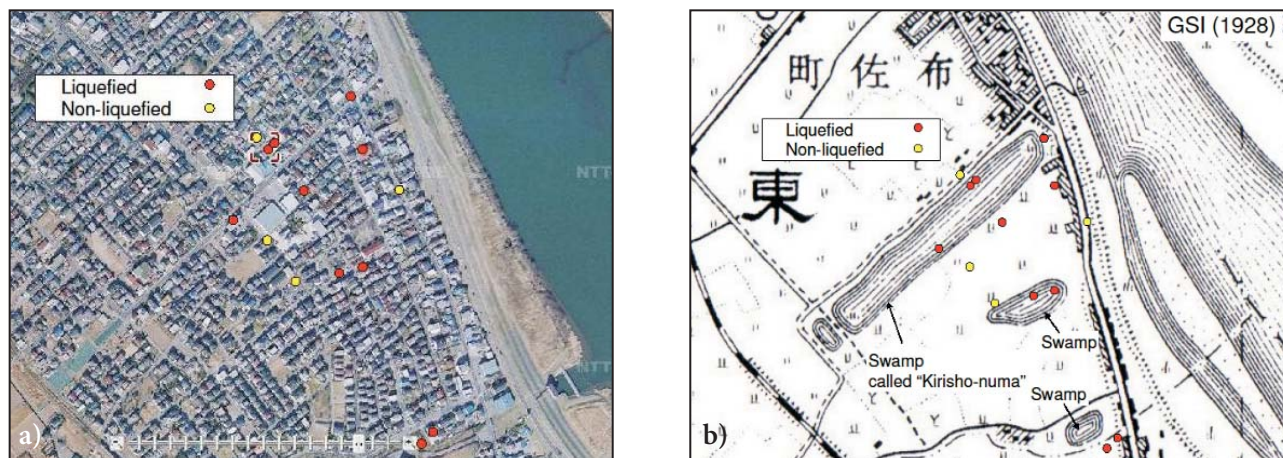


Figure 19. Location of liquefied and non-liquefied sites confirmed by the survey in Abiko city are plotted on (a) recent aerial photo and on (b) old map made by GSI in 1928.

ACKNOWLEDGMENTS

The authors would like to thank the Japan Society for the Promotion of Science (JSPS) for the financial support of the first author's postdoctoral research work at the Institute of Industrial Science, the University of Tokyo.

REFERENCES

- [1] Ibbitt R., Takara K., Desa M.N.M. and H. Pawitan (2002). *Catalogue of rivers for southeast Asia and the Pacific*, vol. IV, 11. Tone-gawa, UNESCO-IHP Publication
- [2] Wikipedia (2012). Tone River, http://en.wikipedia.org/wiki/Tone_River
- [3] Harada, K., (2004). *Kirisho swamp and flood control in Abiko, "Abiko-from your photo albums-"* (in Japanese)
- [4] Geospatial Information Authority of Japan - GSI (2012). *Crustal deformation and fault model obtained from GEONET data analysis*, <http://www.gsi.go.jp/cais/topic110313-index-e.html>
- [5] Japan Meteorological Agency - JMA (2012). *The 2011 off the Pacific coast of Tohoku Earthquake -Portal-*, http://www.jma.go.jp/jma/en/2011_Earthquake.html
- [6] National Research Institute for Earth Science and Disaster Prevention - NIED (2011). *Preliminary report on the recorded strong ground motions*, http://www.kyoshin.bosai.go.jp/kyoshin/topics/TohokuTaiheiyo_20110311/nied_kyoshin2e.pdf
- [7] National Research Institute for Earth Science and Disaster Prevention- NIED (2012). *Strong-motion Seismograph Networks*, <http://www.kyoshin.bosai.go.jp/>
- [8] Towhata I. (2011). Geotechnical damage caused by the recent gigantic earthquake in Japan, *3rd International Conference on Geotechnical Engineering for Disaster Mitigation and Rehabilitation (GEDMAR)*, Indonesia
- [9] Towhata I. (2008). *Geotechnical Earthquake Engineering*, Springer
- [10] Koseki J., Miyashita Y., Deng J. and Araki H. (2011). Effects of liquefaction in Kanto region caused by the 2011 off the Pacific coast of Tohoku earthquake, *Bulletin of ERS*, No.42
- [11] Koseki, J., Miyashita, Y., Deng, J.L. and Araki, H. (2011). Liquefaction along Tone river basin in Japan, caused by the 2011 off the Pacific coast of Tohoku earthquake, *Proc. 2nd International Conference on Performance-based Design in Earthquake Geotechnical Engineering*, Taormina, Italy
- [12] Amaral, M.F., Rios, S. and Viana da Fonseca, A. (2012). Yielding in the isotropic compression of Porto silty sand, *Acta Geotechnica Slovenica*, 9, 1, 30-45
- [13] Lenart, S. (2008). The response of saturated soils to a dynamic load, *Acta Geotechnica Slovenica*, 5, 1, 37-49
- [14] Žlender, B. and Lenart, S. (2005). Cyclic liquefaction potential of lacustrine carbonate silt from Julian Alps, *Acta Geotechnica Slovenica*, 2, 1, 23-31
- [15] Wakamatsu, K. (2012): Recurrent Liquefaction Induced by the 2011 Great East Japan Earthquake, *Journal of Japan Association for Earthquake Engineering*, Vol.12, No.5, pp.69-88, 2012 (in Japanese)

PRIMERJAVA MED OBIČAJNIM TRIOSNIM IN RAVNINSKO-DEFORMACIJSKIM STISKANJEM V POSEBNEM SISTEMU S 3D MDE

MD. MAHMUD SAZZAD IN KIICHI SUZUKI

o avtorjih

vodilni avtor

Md. Mahmud Sazzad
Rajshahi University of Engineering & Technology,
Department of Civil Engineering
Rajshahi-6204, Bangladeš
e-pošta: mmsruet@gmail.com

Kiichi Suzuki
Saitama University,
Department of Civil and Environmental Engineering
Saitama 338-8570, Japonska

izvleček

Sipki materiali, kot npr. pesek, so podvrženi različnim napetostnim glede na terenske pogoje. Sipek sistem pod temelji je, na primer, podvržen običajni triosni stisljivosti (OTS), pri cestnih nasipih pa ravninski napetostno-deformacijski stisljivosti (RNS). Zaradi različnih napetostnih poti je obnašanje sipkih materialov različno. V članku je primerjano obnašanje sipkih materialov v OTS in RNS pogojih z uporabo 3D metode ločenih elementov (MLE). Z uporabo periodičnih robov je bilo iz 8000 delcev numerično pripravljenih enakosmerno stisljivih vzorcev. S tem vzorcem so bili simulirani OTS in RNS preizkusi s ciljem primerjanja in preučevanja makro- in mikro-mehanskega odziva sipkega materiala, pri čemer začetne teksture numeričnega vzorca niso bile spremenjene. Simulirani napetostno-deformacijski odzivi so kvalitativno v skladu z odzivi iz eksperimentalnih študij. V študiji je bilo ugotovljeno, da prožnostni indeks ni odvisen od napetostnih poti. Vrednost b (definirana kot $b = (\sigma_2 - \sigma_3) / (\sigma_1 - \sigma_3)$, kjer je σ_1 , σ_2 oz. σ_3 pritisk v smeri x_1 , x_2 oz. x_3) – krivulja osne deformacije – je pri triosnih preizkusih podobna krivulji razmerja napetosti-osne deformacije. Razvoj koordinatnega števila in drseče kontaktne frakcije ni odvisen od smeri napetosti. Opažena je povezava med makro in mikro količinami in edinstveno makro-mikro razmerjem, ne glede na napetostne poti, uporabljene v tej študiji.

ključne besede

običajna triosna stisljivost, ravninsko-deformacijska stisljivost, mikro dovzetnost, metoda ločenih elementov (MLE)

A COMPARISON BETWEEN CONVENTIONAL TRIAXIAL AND PLANE-STRAIN COMPRESSION ON A PARTICULATE SYSTEM USING 3D DEM

MD. MAHMUD SAZZAD and KIICHI SUZUKI

about the authors

corresponding author

Md. Mahmud Sazzad
Rajshahi University of Engineering & Technology,
Department of Civil Engineering
Rajshahi-6204, Bangladesh
E-mail: mmsruet@gmail.com

Kiichi Suzuki
Saitama University,
Department of Civil and Environmental Engineering
Saitama 338-8570, Japan

abstract

Granular materials such as sand are subjected to different stress paths depending on the in-situ conditions. For example, a granular system under the foundations experiences conventional triaxial compression (CTC), while it experiences plane-strain compression (PSC) in the case of the embankment of roads. Due to the difference in the stress paths, the behavior of granular materials also becomes different. This paper aims at comparing the behavior of granular materials under CTC and PSC conditions using the 3D discrete-element method (DEM). An isotropically compressed dense sample consisting of 8000 spheres was prepared numerically using periodic boundaries. The CTC and PSC tests were simulated using the same isotropically compressed dense sample to compare and explore the macro- and micro-mechanical responses of granular materials without any bias from the initial fabric of the numerical sample. Qualitatively, the simulated stress-strain responses are consistent with that observed in the experimental studies. The dilatancy index is found to be independent of the stress paths used in the present study. The b value (defined as $b = (\sigma_2 - \sigma_3)/(\sigma_1 - \sigma_3)$ where σ_1 , σ_2 and σ_3 are the stresses in the x_1 , x_2 - and x_3 - directions, respectively) - axial strain curve has a close similarity with the stress ratio - axial strain curve for the PSC test. The evolution of the coordination number and the sliding contact fraction is independent of the stress paths. A link between the macro- and micro-quantities is observed and a unique macro-micro relationship is noticed, regardless of the stress paths applied in this study.

keywords

conventional triaxial compression, plane-strain compression, micro response, DEM

1 INTRODUCTION

Granular materials are often subjected to different stress paths depending on the in-situ conditions. For example, the in-situ condition below a foundation is representative of the CTC stress path (a stress path in which σ_1 increases, keeping σ_2 and σ_3 equal and constant), while the in-situ condition in the case of dams or the embankments of roads corresponds well to the PSC stress path (a stress path in which σ_1 increases, keeping σ_3 constant and the strain in x_2 - direction ε_2 zero). These variations in the stress path also alter the mechanical behavior of the granular system. Several studies have been carried out in the experimental works considering such variations in the stress path. For example, Cornforth [1] reported that the internal friction angle is more than 4° greater for the plane-strain condition than the triaxial condition in the dense state. Terzaghi et al. [2] reported similar results. In another study, Peters et al. [3] reported that shear-band initiation is easier under the plane-strain condition than the axis-symmetric condition. The above-mentioned studies reveal that the mechanical behaviors are different depending on the stress paths applied during the experiments. Although several comparison-based studies were reported earlier in the experimental works, they have several shortcomings. For example, the same sample cannot be prepared for the CTC and PSC tests in the experimental studies. However, it is important that the initial fabric of the tested samples be identical to avoid any discrepancy or biasness of the results in comparison-based studies. This inherent limitation of the experiments can be avoided by using the numerical methods such as DEM [4], which has already been recognized as a useful tool for a comprehensive study of the behavior of granular materials (e.g., [5, 6, 7, 8]). Besides, the evolution of micro features can be studied and compared exclusively

using DEM. In spite of this fact, limited studies were reported in the literature that considered CTC and PSC using DEM. For example, Ng [9] considered several stress paths with different sample preparation methods to investigate the macro and micro responses of granular materials. His result indicated that the friction angle of the PSC test simulation was the highest for all the samples. However, many macro- and micro-mechanical results were not considered in earlier DEM-based studies. The objective of this paper is to make a comprehensive study for CTC and PSC and to present a comparison of the macro and micro behaviors of granular materials exclusively for CTC and PSC using 3D DEM. The macro responses including the dilatancy index, b value, etc., are presented and the micro responses, such as the coordination number, sliding contact fraction, contact fabric, etc. are reported. The relationship between the macro stress ratio and micro fabric ratio has also been established.

2 DEM AND THE COMPUTER PROGRAM OVAL

DEM is a numerical method pioneered by Cundall and Strack [4], which has been used in different disciplines of science and engineering and proved its usefulness. The major advantage of DEM is that the kinematics of each particle can be monitored and extracted at any stage of the simulation. DEM-based studies have been widely used to enhance the understanding of granular matter's behavior and to explain the experimentally observed phenomena from the micro-mechanical point of view. A detailed explanation of DEM was reported in Cundall and Strack [4]. The basic idea of DEM is very simple. In DEM, each particle is modeled as an element. An element in DEM can make and break contact with other elements involved in the model. The calculation cycle in DEM involves the alternate use of Newton's second law of motion and a force displacement law. The translational and rotational accelerations of the particles are computed using the following expressions:

$$m\ddot{x}_i = \sum F_i, \quad i = 1, 2, 3 \quad (1)$$

$$I\ddot{\theta} = \sum M \quad (2)$$

where F_i are the force components on each particle; M is the moment on each particle; m is the mass; I is the moment of inertia; \ddot{x}_i are the components of translational acceleration; and $\ddot{\theta}$ is the rotational acceleration of the particle.

In this study, the computer program OVAL [10] is used. The program is written in FORTRAN and can run on

both the Windows and Linux platforms. The effectiveness of OVAL has already been recognized (e.g., [5, 11]). A simple contact model consisting of two linear springs, one in the normal direction and the other in the tangential direction, and a frictional slider has been incorporated. The viscosity coefficient for translational and rotational body damping used in OVAL represents a fraction of the critical damping $2\sqrt{mk_n}$ and $2r\sqrt{Ik_t}$ where r , k_n and k_t denote the radius, normal and tangential contact stiffness of the particle, respectively.

3 SAMPLE PREPARATION METHOD

A cubic sample consisting of 8000 spheres of 16 different sizes (i.e., diameters) ranging from 3 to 4.5 mm was prepared for the simulation of the CTC and PSC tests. At first the spheres were placed at the equally spaced grid points of the cubic frame. The diameters of the spheres were chosen randomly. The initial sample generated in this way was very sparse. The initial sparse sample was compressed isotropically to 100 kPa using periodic boundaries in different stages. The interparticle friction was intentionally set to zero during the preparation of the isotropically compressed sample to ensure the preparation of a dense sample. The desired interparticle friction coefficient was used later during the shear. The void ratio and coordination number of the isotropically compressed dense sample are 0.57 and 5.94, respectively.

4 SIMULATION OF CTC AND PSC TESTS

The same isotropically compressed dense sample was used for the simulation of the CTC and PSC tests so that the initial fabric of the sample prior to the shear remains the same. The simulation of the CTC test was conducted by reducing the sample height slowly downward with a small strain increment of 0.00002% in the vertical direction (x_1 - direction) while keeping the stresses in x_2 - and x_3 - directions equal and constant (i.e., 100 kPa). On the other hand, the simulation of the PSC test was carried out by reducing the sample height slowly with a small strain increment of 0.00002% in the vertical direction (x_1 - direction) downward, while maintaining the stresses in the x_3 - direction constant (i.e., 100 kPa) and keeping the strain in the x_2 - direction zero (i.e., $d\varepsilon_2 = 0$). The simulation condition of the CTC and PSC tests with reference axes is also depicted in Fig. 1 for more clarity. The DEM parameters used in the numerical simulations are presented in Table 1.

Table 1. DEM parameters used in the numerical study.

DEM parameters	Value
Normal contact stiffness (N/m)	1×10^6
Tangential contact stiffness (N/m)	1×10^6
Mass density (kg/m ³)	2650
Increment of time step (s)	1×10^{-6}
Interparticle friction coefficient	0.50
Coefficient of viscosity for translational and rotational body damping	0.05

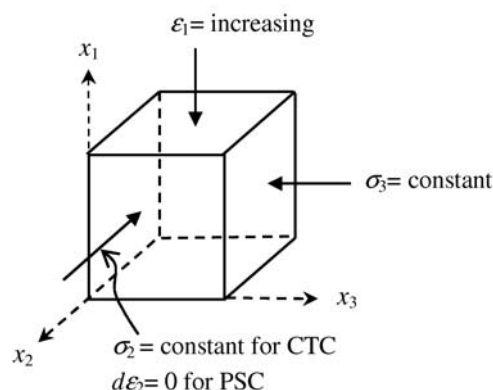


Figure 1. A cubic element with simulation conditions and reference axes.

5 MACRO-MECHANICAL BEHAVIOR

5.1 STRESS-STRAIN RESPONSES

The simulated stress-strain response for the CTC and PSC is depicted in Fig. 2. It is clear that the stress ratio σ_1/σ_3 increases with the axial strain ε_1 followed by strain softening, whatever the case may be. However, softening behavior is dominant and clear in the case of the PSC test. This tendency is consistent with the experimental evidence (e.g., [1]) in a qualitative sense. Note also that the PSC has a higher stress ratio at the peak state than CTC during the simulation.

The evolution of the strains during the CTC and PSC tests is depicted in Fig. 3 where ε_1 , ε_2 and ε_3 represent the strains in the x_1 -, x_2 - and x_3 - directions, respectively. Only 5% of ε_1 is considered in the plot. It is clear in Fig. 3 that the change of ε_2 for the PSC test remains zero throughout the test as required. The evolution of ε_3 is the same as ε_2 for the CTC test as expected. It demonstrates the ability of the DEM to simulate qualitatively the CTC and PSC tests for the dense sample.

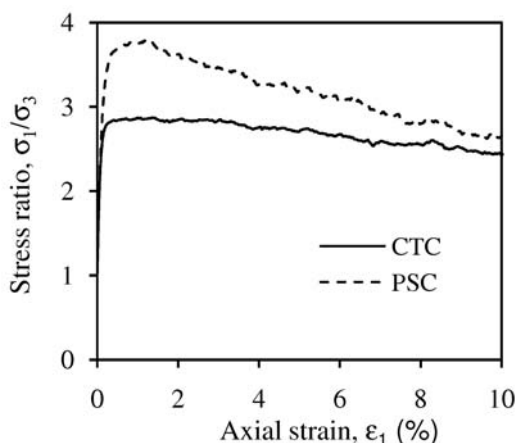


Figure 2. Stress-strain response for CTC and PSC tests.

The evolution of the volumetric strain ε_v with ε_1 for the CTC and PSC tests is shown in Fig. 4. Here, $\varepsilon_v = dV/V$ where V represents the initial volume of the dense sample prior to shear and dV represents the change of volume during the shear. A positive value ε_v in Fig. 4 represents compression, while a negative value of ε_v indicates dilation. Note that the dilation in the case of the PSC test overrides the dilation in the case of the CTC test although the difference is small.

The evolution of the dilatancy index with ε_1 is depicted in Fig. 5. The dilatancy index is defined here as $DI = -d\varepsilon_v/d\varepsilon_1$, where $d\varepsilon_v$ represents the change of the volumetric strain and $d\varepsilon_1$ represents the change of the axial strain. Note that the tendency of the evolution of the dilatancy index is independent of the stress paths applied in this study.

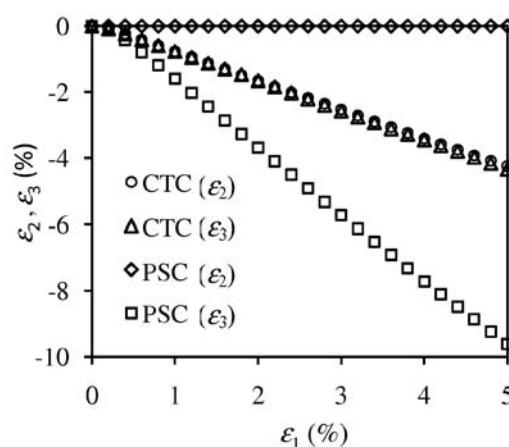


Figure 3. Evolution of strains for CTC and PSC tests.

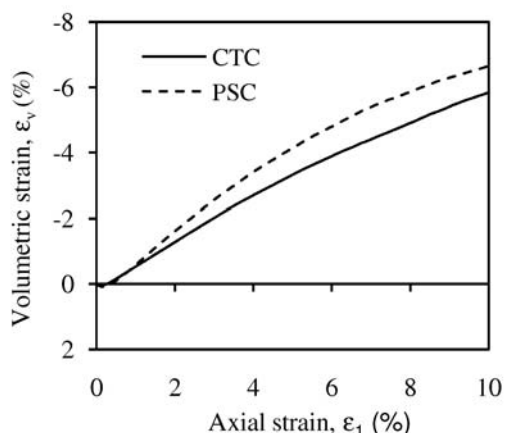


Figure 4. Evolution of volumetric strain for CTC and PSC tests.

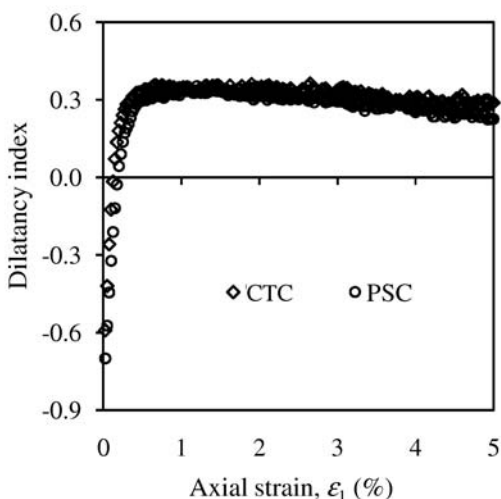


Figure 5. Evolution of dilatancy index for CTC and PSC tests.

5.2 EVOLUTION OF *b* VALUE

The term ‘*b*’ was first introduced by Habib [12] and defined in the non-dimensional form as follows:

$$b = \frac{\sigma_2 - \sigma_3}{\sigma_1 - \sigma_3} \quad (3)$$

In CTC test, $\sigma_2 = \sigma_3$. Consequently, the *b* value should be zero throughout the test. However, in the PSC test, the *b* value is not constant, rather it is variable. In the present numerical study, the evolution of the *b* value with ϵ_1 is computed and depicted in Fig. 6. It is clear that the *b* value remains constant throughout the numerical simulation for the CTC test, as expected. However, the *b* value varies with ϵ_1 for the PSC test and the evolution tendency of the *b* value with ϵ_1 has a close similarity to that of σ_1/σ_3 with ϵ_1 , at least in a qualitative sense. The *b* value gradually increases with the increase of ϵ_1 until

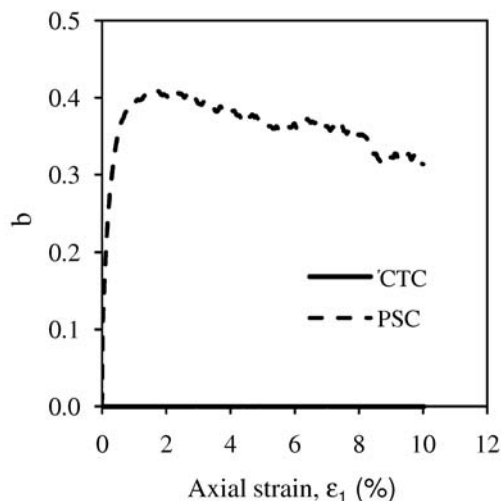


Figure 6. Evolution of the *b* value with ϵ_1 for the CTC and PSC tests.

it reaches a peak value, and beyond the peak the *b* value reduces with the increase of ϵ_1 . The *b* value at the peak stress state for PSC is 0.396, while the same at 10% axial strain is 0.314.

6 MICRO-MECHANICAL RESPONSES

6.1 EVOLUTION OF THE COORDINATION NUMBER

The evolution of the coordination number with ϵ_1 for the CTC and PSC tests is shown in Fig. 7. The coordination number is defined as twice the total number of contacts to the total number of particles used in the simulation. Note that the coordination number decreases significantly at the beginning stage of simulation, regardless of the stress paths. It is probably due to the rearrangement of the fabric when the isometrically compressed dense sample is subjected to either the CTC or PSC tests. Later, the rate of the change of coordination number becomes very small for large strain. It should also be noted that the evolution of the coordination number is independent of the stress paths applied (i.e., CTC and PSC) during the simulation.

6.2 EVOLUTION OF THE SLIDING CONTACT FRACTION

The evolution of the sliding contact fraction for the CTC and PSC tests is shown in Fig. 8. The sliding contact fraction is defined here as the number of sliding contacts to the number of contacts at a given state of the simulation.

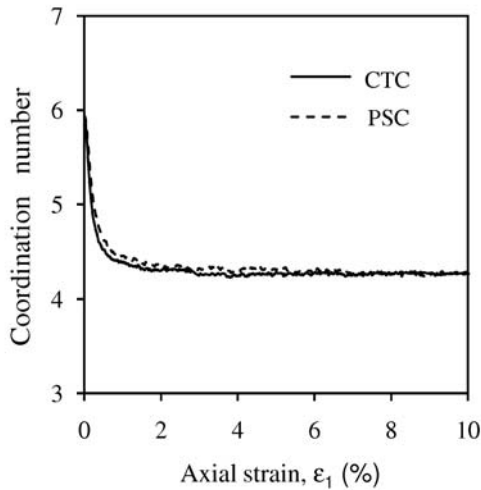


Figure 7. Evolution of coordination number with ε_1 for the CTC and PSC tests.

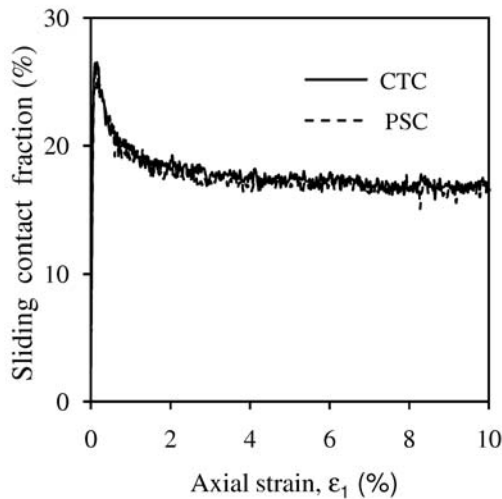


Figure 8. Evolution of sliding contact fraction with ε_1 for the CTC and PSC tests.

The sliding contact fraction in the plot is expressed as a percentage. The sliding contact fraction peaks at a very early stage of the simulation regardless of the stress paths. Note that the evolution of the sliding contact fraction is independent of the stress paths (i.e., CTC and PSC).

6.3 EVOLUTION OF THE CONTACT FABRIC

The DEM is supposed to be the best numerical method to understand the evolution of the fabric and the microstructure of granular materials, because experimentally it is not easy to measure and extract all the fabrics directly for any given state. The evolution of the contact fabric for the CTC and PSC tests is reported in this

section. The evolution of the contact fabric is usually quantified using the fabric tensor given by Satake [13], considering all the contacts as follows:

$$H_{ij} = \frac{1}{N_c} \sum_{\alpha=1}^{N_c} n_i^\alpha n_j^\alpha, \quad i, j = 1, 2, 3 \quad (4)$$

where n_i^α is the i -th component of the unit normal vector at the α -th contact and N_c is the number of contacts. The contacts in a granular system can be further characterized as the strong contacts and the weak contacts in order to quantify their individual roles (e.g., [8, 14]). In the present study, a contact is defined as a strong contact if the normal contact force for a given contact is greater than the average normal contact force, while a contact is defined as a weak contact if the normal contact force for a given contact is less than or equal to the average normal contact force. The average normal contact force is calculated as follows:

$$f_{ave}^n = \frac{1}{N_c} \sum_{i=1}^{N_c} f_i^n \quad (5)$$

where f_i^n is the normal contact force at the i -th contact and f_{ave}^n is the average normal contact force considering all the contacts. Based on the classification of the total contacts into strong and weak contacts, two additional fabric tensors for the strong and weak contacts can be defined. The fabric tensor for strong contacts can be defined as follows [10]:

$$H_{ij}^s = \frac{1}{N_c^s} \sum_{s=1}^{N_c^s} n_i^s n_j^s, \quad i, j = 1, 2, 3 \quad (6)$$

where n_i^s is the i -th component of the unit normal vector at the s -th strong contact and N_c^s is the number of strong contacts. Similar to the fabric tensor for strong contacts, the fabric tensor for the weak contacts can also be defined as follows:

$$H_{ij}^w = \frac{1}{N_c^w} \sum_{w=1}^{N_c^w} n_i^w n_j^w, \quad i, j = 1, 2, 3 \quad (7)$$

where n_i^w is the i -th component of the unit normal vector at the w -th weak contact and N_c^w is the number of weak contacts.

Fig. 9 shows the evolution of the fabric ratio H_{11}/H_{33} with ε_1 for the CTC and PSC tests considering all the contacts. Note that the fabric ratio H_{11}/H_{33} is almost 1.0 at the zero strain level, which indicates the isotropic distribution of the contact fabric prior to the shear. A value greater than 1.0 or less than 1.0 indicates the anisotropic distribution of the contact fabric. It should be noted that H_{11}/H_{33}

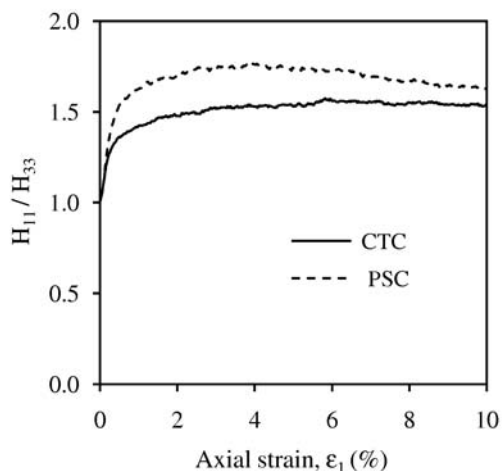


Figure 9. Evolution of H_{11}/H_{33} with ε_1 for the CTC and PSC tests.

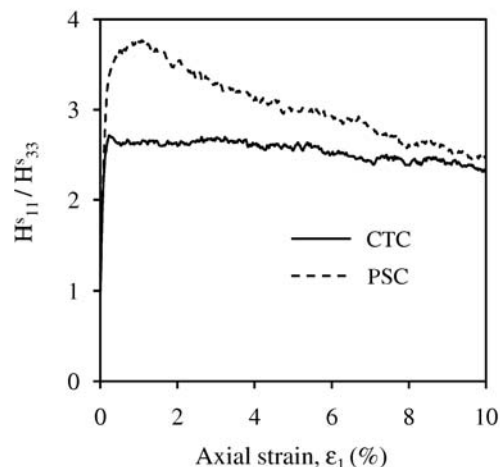


Figure 10. Evolution of H_{11}^s/H_{33}^s with ε_1 for the CTC and PSC tests.

gradually increases with ε_1 until it reaches a peak value, which is followed by a decrease in the fabric ratio, regardless of the stress path. This increase of H_{11}/H_{33} with ε_1 is the consequence of the formation of new contacts in the vertical direction (x_1 - direction) and the disintegration of contacts in lateral directions. However, the dominant evolution of H_{11}/H_{33} is noticed for the PSC condition as a constraint in the strain is applied in the x_2 - direction during the shear. A comparison of Fig. 9 with Fig. 2 shows that the shapes of the curves of these two figures do not correspond well with each other. For example, the stress ratio peaks at the small strain level as seen in Fig. 2 whereas the fabric ratio peaks at a large strain level as seen in Fig. 9 when all contacts are considered.

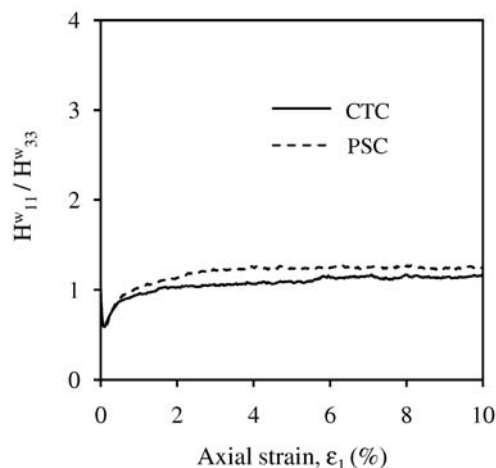


Figure 11. Evolution of H_{11}^w/H_{33}^w with ε_1 for the CTC and PSC tests.

Fig. 10, on the other hand, shows the evolution of the fabric ratio H_{11}^s/H_{33}^s with ε_1 for the CTC and PSC tests considering only the strong contacts. A comparison of Fig. 10 with Fig. 2 indicates a strong correspondence between the stress ratio-axial strain curve and the fabric ratio-axial strain curve for strong contacts, regardless of the stress paths. It should also be noted that the anisotropy induced during the PSC test is higher than that during the CTC test. This large difference in the evolution of the induced anisotropy in the PSC test may be a consequence of the restriction of the boundary movement in the x_2 - direction. It can be presumed that the higher peak stress in the case of the PSC test may be strongly correlated with such a dominant evolution of the induced anisotropy in the case of the PSC test.

Fig. 11 shows the evolution of the fabric ratio H_{11}^w/H_{33}^w with ε_1 for the CTC and PSC tests considering the weak contacts only. Note that the fabric ratio is even smaller than 1.0 at the very early stage of the simulation. This indicates that the anisotropy induced for weak contacts at the initial stage of the simulation has an opposite

privilege direction compared to the privilege direction of the induced anisotropy considering strong contacts. However, such an evolution characteristic changes as the sample is subjected to further deformation. The fabric ratio H_{11}^w/H_{33}^w gradually increases with ε_1 and becomes greater than 1.0 as the strain increases. It indicates that the privilege direction of the induced fabric anisotropy for weak contacts gradually changes its direction as the strain increases. Note that the induced fabric anisotropy for weak contacts is also dominant in the case of the PSC test; however, the difference is small compared to the difference noticed in the case of strong contacts.

6.4 MACRO-MICRO RELATIONSHIP

A strong correlation between the stress ratio-axial strain curve (Fig. 2) and the fabric ratio-axial strain curve for strong contacts (Fig. 10) is noticed. Accordingly, it is

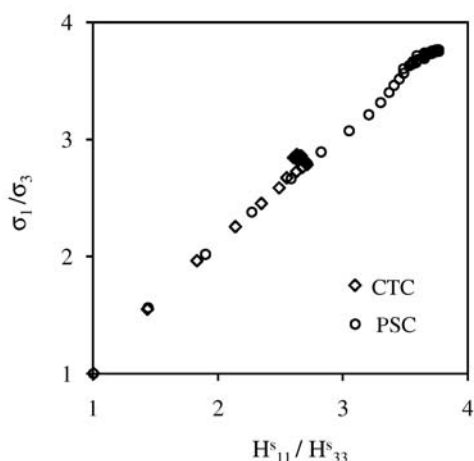


Figure 12. Relationship between σ_1/σ_3 and H_{11}^s/H_{33}^s considering strong contacts for the CTC and PSC tests.

intended to establish a relationship between the macro quantity σ_1/σ_3 and the micro quantity H_{11}^s/H_{33}^s during the CTC and PSC, considering only the strong contacts. Fig. 12 shows the relationship between the stress ratio σ_1/σ_3 and the fabric ratio H_{11}^s/H_{33}^s , considering the strong contacts. For a clear view, data up to 1% of the axial strain is shown in Fig. 12. A unique macro-micro relationship is observed, regardless of the stress paths applied in the present study.

7 CONCLUSIONS

A numerical investigation using DEM is carried out to explore and compare the macro- and micro-mechanical behaviors of granular materials. A simulation of the CTC and PSC tests was conducted on the same dense sample without any bias from the initial fabric prior to shear. Different macro results, in particular, the evolution of the b value with axial strain are reported. The evolution of different micro variables is presented as well. A link between the macro and micro quantities is also established. Some of the points of this study can be summarized as follows. These points are valid for dense samples only.

- i) The b value-axial strain curve resembles the stress ratio-axial strain curve for the PSC test.
- ii) The evolution of the coordination number and the sliding contact fraction is independent of the stress paths.
- iii) The fabric ratio that develops during the PSC test is larger than that during the CTC test, regardless of the type of contact.
- iv) The shape of the fabric ratio-axial strain curve is similar to that of the stress ratio-axial strain curve when strong contacts are considered in quantifying the fabric tensor.
- v) A unique relationship between the stress ratio and

the fabric ratio exists, regardless of the stress paths applied in the present study.

REFERENCES

- [1] Cornforth, D.H. (1964). Some experiments on the influence of strain conditions on the strength of sand. *Geotechnique*, Vol. 14, No. 2, pp. 143–167.
- [2] Terzaghi, K., Peck, R.B., Mesri, G. (1996). *Soil Mechanics in Engineering Practice*, John Wiley & Sons, New York.
- [3] Peters, J.F., Lade, P.V., Bro, A. (1988). Shear Band Formation in Triaxial and Plane Strain Tests. *Advanced Triaxial Testing of Soil and Rock*, ASTM STP977, Robert T., Donaghe, Ronald C., Chancy and Marshall L. Silver Eds., Philadelphia, pp. 604–627.
- [4] Cundall, P.A., Strack, O.D.L. (1979). A discrete numerical model for granular assemblies. *Geotechnique*, Vol. 29, No. 1, pp. 47–65.
- [5] Kuhn, M.R. (1999). Structured deformation in granular materials. *Mechanics of Materials*, Vol. 31, No. 6, pp. 407–429.
- [6] Ng, T.-T. (2001). Fabric evolution of ellipsoidal arrays with different particle shapes. *Journal of Engineering Mechanics*, ASCE, Vol. 127, No. 10, pp. 994–999.
- [7] Radjai, F., Roux, S., Moreau, J.J. (1999). Contact forces in a granular packing. *Chaos*, Vol. 9, No.3, pp. 544–550.
- [8] Sazzad, M.M., Suzuki, K. (2010). Micromechanical behavior of granular materials with inherent anisotropy under cyclic loading using 2D DEM. *Granular Matter*, Vol. 12, No. 6, pp.597–605.
- [9] Ng, T.-T. (2005). Behavior of gravity deposited granular material under different stress paths. *Canadian Geotechnical Journal*, Vol. 42, No. 6, pp. 1644–1655.
- [10] Kuhn, M.R. (2006). OVAL and OVALPLOT: Programs for analyzing dense particle assemblies with the discrete element method. http://faculty.up.edu/kuhn/oval/doc/oval_0618.pdf (last accessed: January 31, 2012)
- [11] Kuhn, M.R. (2005). Are granular materials simple? An experimental study of strain gradient effects and localization. *Mechanics of Materials*, Vol. 37, No. 5, pp. 607–627.
- [12] Habib, P. (1953). Influence of the variation of the average principal stress upon the shearing strength of soils [in French]. *Proceedings of the 3rd International Conference on Soil Mechanics and Foundation Engineering*, Vol. 1, pp. 131–136.
- [13] Satake, M. (1982). Fabric tensor in granular materials. *Proceeding of IUTAM Symposium on Deformation and Failure of Granular Materials*, Delft, Balkema, pp. 63–68.
- [14] Radjai, F., Wolf, D.E., Jean, M., Moreau, J.J. (1998). Bimodal character of stress transmission in granular packing. *Physical Review Letters*, Vol. 80, No. 1, pp. 61–64.

NUMERIČNO MODELIRANJE PLAVAJOČIH MONTAŽNIH NAVPIČNIH DRENAŽ V VEČPLASTNI ZEMLJINI

IKHYA IKHYA ĀN HELMUT F. SCHWEIGER

o avtorjih

Ikhya Ikhya
Graz University of Technology (TU Graz),
Institute for Soil Mechanics and Foundation Engineering,
Computational Geotechnics Group
Rechbauerstrasse 12, 8010 Graz, Avstrija
e-pošta: ikhya@tugraz.at, ikhya@itenas.ac.id

Helmut F. Schweiger
Graz University of Technology (TU Graz),
Institute for Soil Mechanics and Foundation Engineering,
Computational Geotechnics Group
Rechbauerstrasse 12, 8010 Graz, Avstrija
e-pošta: helmut.schweiger@tugraz.at

izvleček

Članek prikazuje primerjavo terenskih meritev in numerični model posedanja nasipov na mehki zemljini v okviru indonezijskega projekta Cirebon Power Plant, kjer so bile nameščene montažne vertikalne drenaže (MVD). Za določitev optimalne globine namestitve drenaž so bile z numeričnim modelom preučene plavajoče MVD v dvoslojnih tleh pri pogojih dreniranja v eni in obeh plasteh. Študija je pokazala dobro ujemanje terenskih meritev posedanja z numeričnimi napovedmi. Zanimiv rezultat študije je, da razlike v togosti in/ali prepustnosti neizboljšane zemljine pod konico MVD pomembno vplivajo na optimalno penetracijsko globino (L/H) v dvoslojnih tleh. Numerična študija je pokazala, da se lahko plavajoče MVD uporabijo za enojno drenažo, če je druga plast bolj toga in/ali bolj prepustna kot prva plast.

ključne besede

dvoslojna tla, plavajoče montažne vertikalne drenaže, dvojna in enojna drenaža, numerični model, mehka glina, konsolidacija

NUMERICAL MODELING OF FLOATING PREFABRICATED VERTICAL DRAINS IN LAYERED SOIL

IKHYA IKHYA and HELMUT F. SCHWEIGER

about the authors

Ikhya Ikhya
Graz University of Technology (TU Graz),
Institute for Soil Mechanics and Foundation Engineering,
Computational Geotechnics Group
Rechbauerstrasse 12, 8010 Graz, Austria
e-mail: ikhya@tugraz.at, ikhya@itenas.ac.id

Helmut F. Schweiger
Graz University of Technology (TU Graz),
Institute for Soil Mechanics and Foundation Engineering,
Computational Geotechnics Group
Rechbauerstrasse 12, 8010 Graz, Austria
e-mail: helmut.schweiger@tugraz.at

abstract

This paper presents a comparison of field measurements and a numerical model of settlements based on the construction of an embankment on soft soil for the Cirebon Power Plant Project in Indonesia, where prefabricated vertical drains (PVDs) were installed. In the numerical model, floating PVDs in two soil layers for two- and one-way drainage conditions are examined in order to determine the optimum penetration depth. In this study, good agreement between the field measurements of the settlements and the numerical prediction could be achieved. An interesting result of this study is that the differences in the stiffness and/or the permeability in the unimproved area below the PVD tip have a significant influence on the optimum penetration depth (L/H) in the two-soil-layer condition. The numerical study showed that it is possible to use floating PVDs in single drainage conditions if the second layer is stiffer and/or more permeable than the first layer.

keywords

two soil layers, floating prefabricated vertical drain, double and single drainage, numerical model, soft clay, consolidation

1 INTRODUCTION

Soft soil deposits such as soft clays, organic soils, and peats are generally characterized by a low shear strength, a high compressibility, and a low coefficient of permeability, which makes them a difficult soil for engineering. Soft soil deposits can be found throughout the world, including many parts of Indonesia, which possesses one of the longest coastlines in the world, with many of them having soft soil deposits. The total area of soft soil deposits in Indonesia is around 20 million hectares, i.e., 10% of Indonesia's total land area, which is mostly located in the coastal areas [1]. There are soft clays and peats with varying depth, shown as black areas in figure 1.

Ground-improvement techniques play an important role in extending the infrastructure across the country in difficult soils. Vertical drains combined with preloading have become common practice and are among the most effective procedures for ground improvement, accelerating the consolidation process and decreasing the time to reach final settlements. The installation of vertical drains reduces the drainage path and speeds up the excess pore-water pressure dissipation generated during the application of surcharge loads in saturated, fine-grained soils, thereby resulting in the faster development of settlements and a more rapid gain of strength due to consolidation.

It seems that almost all published numerical and analytical studies of soil consolidation with floating PVDs considered a homogeneous soil layer and a two-way drainage condition [2-11], which means that none of those studies focused on evaluating the effects of inhomogeneous soil layering in two- and one-way drainage conditions.

In this study the effects of floating PVDs in two soil layers for two- and one-way drainage conditions are numerically investigated in order to determine the optimum penetration depth. The results from this study can be used for similar cases where the sub-soil condition consists of more than one soil layer with similar mechanical and hydraulic properties.

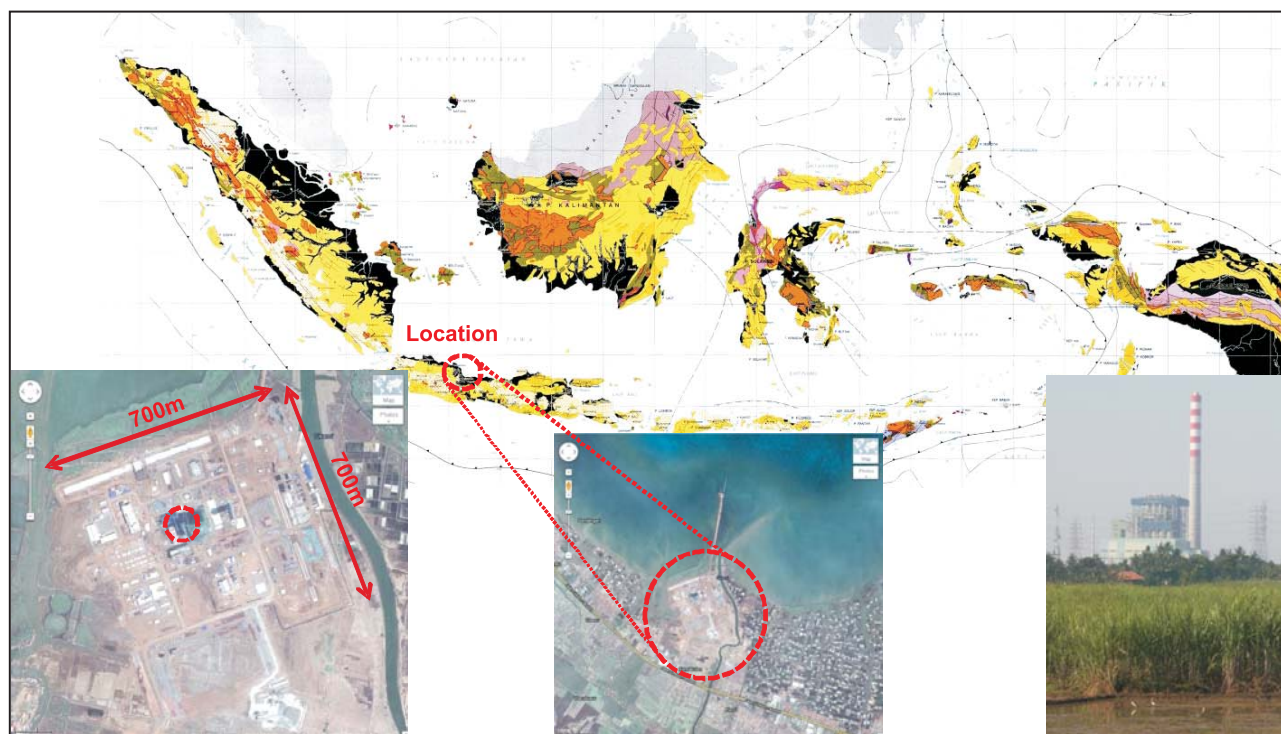


Figure 1. Soft soil areas in Indonesia and the location of the Cirebon Power Plant.

2 SITE DESCRIPTION AND GROUND CONDITION

The Cirebon Power Plant site is located on the north coastal plain of Java, near Kanci Village, which is approximately 20 kilometres to the south-east of Cirebon city and around 290 kilometres to the east of Jakarta city. The site is bounded by the Java Sea to the north, the Kanci River to the east, and the Waruduwur River to the west. The area of the single-unit 660MW coal-fired power station covers around 50 hectares. The topography of the plant site comprises a relatively flat and low-lying area with an average elevation of around +0.5 meters above mean sea level. The coast of the Cirebon area has a tidal range between 0.5 to 1.3 meters [12]. An overview of the soft soil areas in Indonesia and the location of the Cirebon Power Plant are shown in figure 1.

In order to establish a horizontal platform and to keep the site above flood level and always dry during the life time of the plant, the entire plant site area was reclaimed to reach a final elevation of +2.50 meters above mean sea level. The average thickness of the land fill is about 4 meters, including a 1.0 meter sand blanket, a 2.0 meter embankment, and 1.0 meter additional surcharge [13, 14].

The formation of the northern coast of Java, some on the North East Sumatra, and the other coastal areas of Indonesia, are normally Holocene soft clay deposits and quite similar to parts of the coasts of Singapore, Malaysia, Thailand, and in the other South East Asia countries [15, 16]. Based on the result of the soil investigation [17, 18, 14], the condition of the subsurface soils in the site area can be classified into three distinct soil layers: on top is a 6 meter very soft clay layer followed by a 6 meter soft-to-medium clay layer, which is underlain by a dense sand or a silty sand layer as the bearing strata. The ground-water table is located close to the ground surface.

To speed up the consolidation process of the top 12 meters of soft clay, PVDs together with 4.0 meters of filling material were installed, which can be considered to be a good solution in terms of cost and time efficiency. The drains were installed to a depth of 12 meters until reaching the dense soil layer with a 1.5 meter centre-to-centre spacing in a triangular grid pattern. The settlement plate and the drains were installed after the construction of a 1.0 meter sand blanket as the working area. A settlement analysis due to the areal fill was carried out around the centre of the fill [13]. The subsoil conditions, embankment thickness, PVD layout and the location of the settlement plate are shown in figure 2.

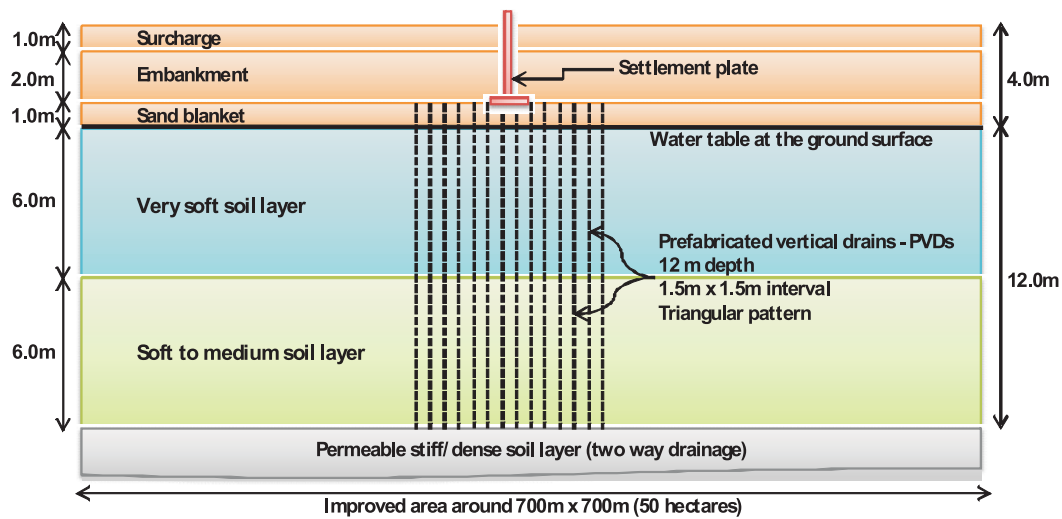


Figure 2. Subsoil and embankment condition, PVD configuration, and location of the settlement plate.

3 NUMERICAL MODEL

A Numerical model using the commercial finite-element software PLAXIS 2D 2010 was used to analyse this case study [19]. Axisymmetric conditions were chosen to simulate a unit-cell condition with a single drain at the center of the fill area. The total number of elements (15-noded triangles) in this model is 1343. The soil and the embankment were modelled using the Hardening Soil model, the advanced soil model in Plaxis for simu-

lating both soft and stiff soils [20, 19]. Four different cases are considered in the numerical simulation: without improvement, with PVD improvement but ignoring smear effects, with PVD improvement considering the effects of smear caused by PVD installation and partial penetration of PVDs. The results from this numerical model were compared with data measured in the field. Figure 3 shows the geometry of the unit cell and the finite-element mesh in the axisymmetric condition for both full and floating PVDs.

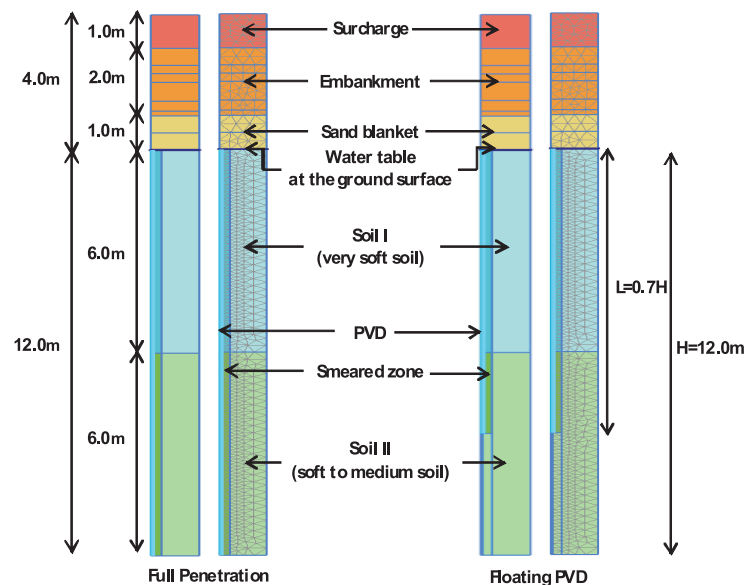


Figure 3. Geometry of unit cell and finite-element mesh for full penetration and floating PVD.

The drains were installed to a depth of 12 and 8.4 meters (L) for full and partial penetration, respectively, with a 1.5 meter spacing (S) in a triangular grid pattern. The soft clay layer to be improved was 12 meters thick (H). The equivalent influence zone diameter (the unit-cell diameter, d_e) is 1.575 meter, calculated based on the principle of equal area ($d_e=1.05 \cdot S$). The equivalent drain diameter (d_w) is 66 mm, calculated based on the equal drainage perimeter assumption proposed by Hansbo [21] $d_w = 2(a \cdot b/\pi)$, where $a = 100$ mm and $b = 4$ mm are the width and thickness of the drain. Chai and Miura [22] suggested that the equivalent smeared zone diameter (d_s) can be estimated as $d_s = 3 \cdot d_m$, where $d_m = 120$ mm is the equivalent mandrel or anchor diameter.

The horizontal and vertical soil permeability are assumed to be the same ($k_h = k_v$), which is probably slightly unrealistic, but as no further information was available and the problem is considered to be governed by k_h , with the exception of floating PVDs, this assumption has been made. The ratio of the horizontal permeability in the undisturbed soil zone to the permeability in the

smeared zone (k_h/k_s) is 2 and the well resistance is not taken into account because the drain-discharge capacity (q_w) is assumed to be large enough. The sand blanket is free draining and the bottom boundary is set to be open because a permeable soil layer is below the soft clay layer.

Hardening soil model parameters for the soil and the embankment used in the model are summarized in table 1. These parameters are based on the geotechnical report for this project and it is obvious that the values used for effective cohesion are rather optimistic for this type of soil. However, as the ultimate limit-state conditions are not considered, it can be argued that this assumption has no serious consequences for the results discussed in this study and thus the values given in the geotechnical report have been kept. In addition, one would expect the soil to exhibit creep behaviour, but this would be more relevant in the long-term assessment of settlements, which is not the topic of this investigation, although it is acknowledged that some creep may occur within the time frame analysed, but it is argued that due to the installation of the PVDs consolidation is prevailing. The calculation phases to simulate the stages of construction are shown in table 2.

Table 1. Soil and embankment properties.

HS Model Parameters	Drainage Condition	Thickness m	$\gamma_{unat}/\gamma_{sat}$ kN/m ²	$E_{50}^{ref} = E_{eod}^{ref}$ kN/m ²	E_{ur}^{ref} kN/m ²	$m(\text{power})$ -	c'_{ref} kN/m ²	φ' °	U'_{ur} -	p_{ref} kN/m ³	K_0^{nc} -	R_f -	$k_h = k_v$ m/s
Soil Layer II	Undrained	6	17/18	3000	9000	0.7	1	28	0.2	100	0.530	0.9	5.0×10^{-9}
Embankment	Drained	4	18/20	20000	60000	0.5	10	30	0.2	100	0.500	0.9	1.0×10^{-7}

Table 2. Stages of embankment construction of the Cirebon Power Plant.

No	Stage of Construction	Date	Days	2007		2008											
				November	December	January	Feb	March	April	May	June	July	August	Sept			
1	Site clearing and preparation	16 November – 25 November 2007	10	[Gantt bar]													
2	0.5m Sand Blanket (+0.5m)	26 November – 27 November 2007	2	[Gantt bar]													
3	Consolidation	28 November – 29 November 2007	2	[Gantt bar]													
4	0.5m Sand Blanket (+1.0m)	30 November 2007	1	[Gantt bar]													
5	Consolidation	01 December – 05 December 2007	5	[Gantt bar] Preparation of PVD installation													
6	PVD+Smear Installation	06 December – 08 December 2007	3	[Gantt bar]													
7	Consolidation	09 December – 10 December 2007	2	[Gantt bar] Settlement plate installation at +1.0m													
8	0.15m Embankment (+1.15m)	11 December 2007	1	[Gantt bar]													
9	0.3m Embankment (+1.45m)	12 December 2007	1	[Gantt bar] Start reading of settlement plate													
10	0.55m Embankment (+2.0m)	13 December 2007	1	[Gantt bar]													
11	Consolidation	14 December - 16 December 2007	3	[Gantt bar]													
12	0.25m Embankment (+2.25m)	17 December 2007	1	[Gantt bar]													
13	Consolidation	18 December 2007	1	[Gantt bar]													
14	0.25m Embankment (+2.5m)	19 December 2007	1	[Gantt bar]													
15	Consolidation	20 December – 27 December 2007	8	[Gantt bar] Christmas holiday													
16	0.5m Embankment (+3.0m)	28 December 2007	1	[Gantt bar]													
17	Consolidation	29 December – 04 January 2008	7	[Gantt bar] New year holiday													
18	1.0m Surcharge (+4.0m)	05 January 2008	1	[Gantt bar]													
19	119 days consolidation	06 January – 03 may 2008	119	[Gantt bar] Last day of measured													
20	Final Consolidation	04 May – 23 September 2008	141	[Gantt bar]													

The excess pore-pressure distribution along the 12 meters of soft clay layers after the construction of the 4.0 meter fill material is visualized in Figure 4. The development of the settlements and the excess pore pressures obtained from the numerical model is shown in figure 5 for all four conditions. As expected, the installation of the PVD significantly decreased the consolidation time, whereas considering the smear effects has the opposite effect and, therefore, in order to arrive at realistic predictions, this effect has to be taken into account.

The settlement plate was installed and measurements started after the installation of the 1.0 meter sand

blanket and the drains, so no settlement readings were taken for this stage of the construction. The settlements obtained from the numerical prediction and measured in the field are compared in figure 6. It can be seen that a good agreement between the field measurement and the numerical prediction could be achieved, for both full and partial penetration ($L/H=0.7$) of the PVD when taking the smear effect into account. It is clear that the length of the drain can be reduced by up to 30% without significantly affecting the consolidation process for double drainage—two soil-layer conditions when the second layer is stiffer and has a higher permeability than the first layer.

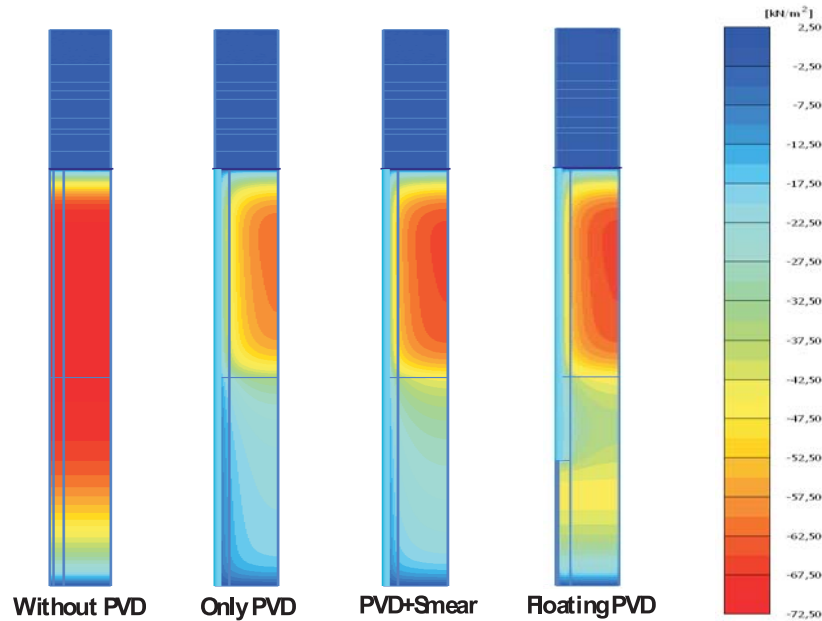


Figure 4. Excess pore-pressure distribution after the placement of 4.0 meter fill material.

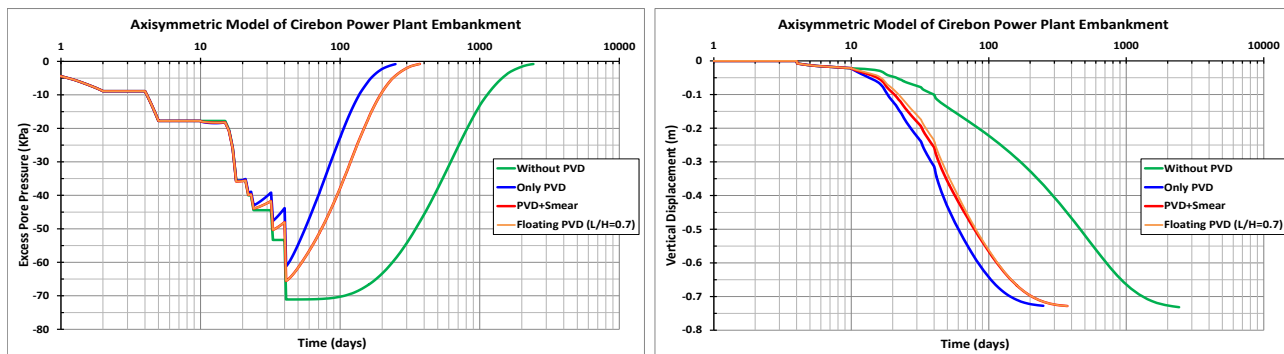


Figure 5. Excess pore-pressure and consolidation curves for all conditions.

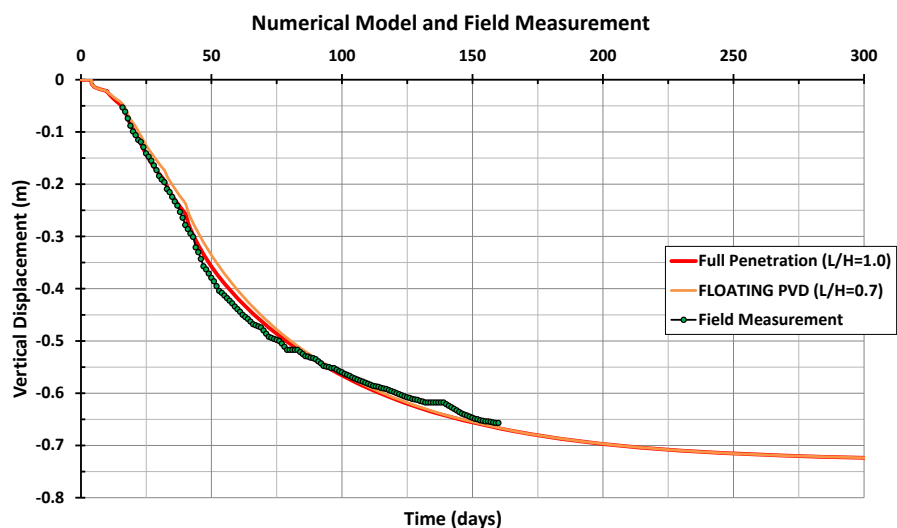


Figure 6. Comparison of settlements between the numerical prediction and field measurements.

4 FLOATING PVD IN TWO SOIL LAYERS

In this section, three different cases will be numerically investigated to look at the influence of floating PVDs on consolidation in a two-soil-layer condition. Figure 7 shows the three conditions analysed: first, a homogeneous soil layer, second, two soil layers where the lower layer is stiffer and more permeable than the upper layer, and third, the situation when the upper layer is stiffer and more permeable than the lower layer. The influence of the stiffness and the permeability will also be evaluated. Finally, the double and single drainage conditions will be examined for the above three cases. The results

from this model will be evaluated in order to determine the optimum penetration depth (L/H), without significantly affecting the consolidation process. Table 3 summarizes all the analysed combinations.

4.1 DOUBLE DRAINAGE CONDITION

In this section, the effect of floating PVDs in a double drainage, two-soil-layers condition, on consolidation is numerically investigated. Here, the bottom boundary is open for flow. The result from this model will be evaluated so as to determine the optimum penetration depth (L/H), without significantly affecting the consolidation process.

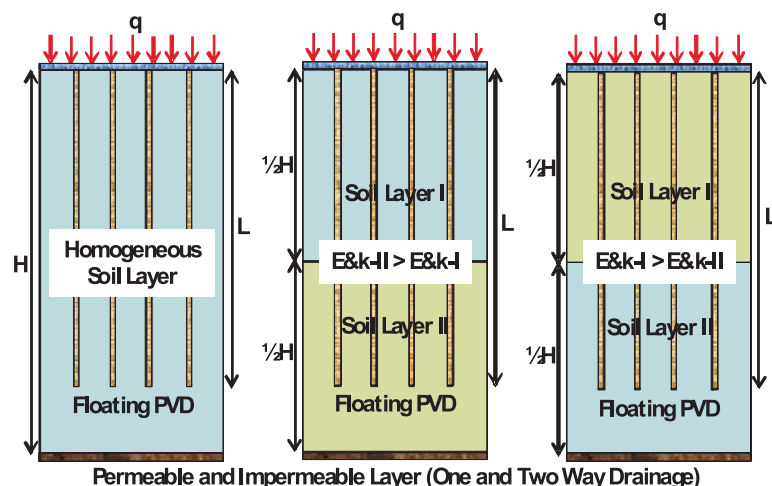


Figure 7. Illustration of three different cases of floating PVDs in two soil layers for one- and two-way drainage.

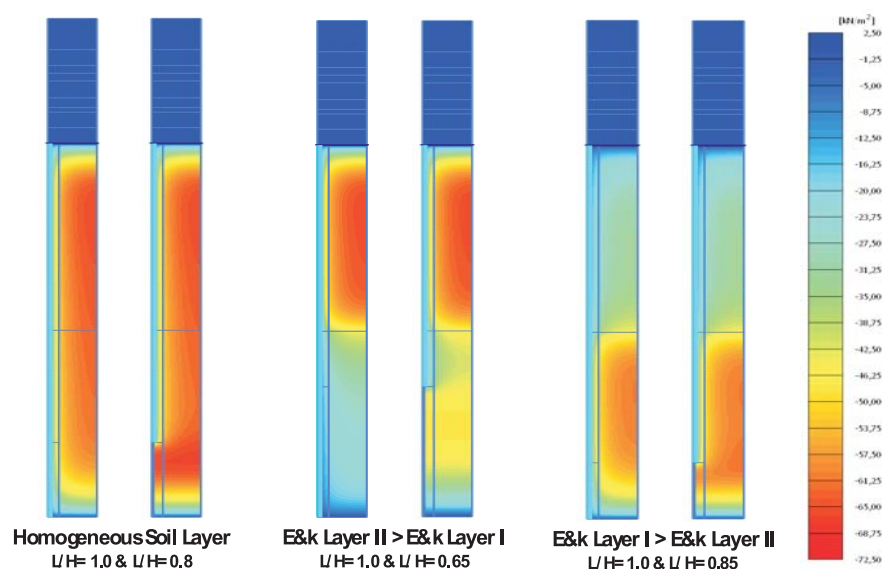
Table 3. Combination of cases for modelling floating PVDs in two soil layers for one- and two-way drainage conditions.

Model	Soil Layer I			Soil Layer II			Remarks	
	$E_{50}^{ref} = E_{oed}^{ref}$	E_{ur}^{ref}	$k_h = k_v$	$E_{50}^{ref} = E_{oed}^{ref}$	E_{ur}^{ref}	$k_h = k_v$		
	kN/m ²	kN/m ²	m/s	kN/m ²	kN/m ²	m/s		
I	<u>1000</u>	<u>3000</u>	<u>1.9×10^{-9}</u>	<u>1000</u>	<u>3000</u>	<u>1.9×10^{-9}</u>	Homogeneous soil layer	
II	A	1000	3000	1.9×10^{-9}	1000	3000	<u>5.0×10^{-9}</u>	Value of soil permeability in layer II is higher than layer I
	B	1000	3000	1.9×10^{-9}	<u>3000</u>	<u>9000</u>	1.9×10^{-9}	Value of soil stiffness in layer II is higher than layer I
	C	1000	3000	1.9×10^{-9}	<u>3000</u>	<u>9000</u>	<u>5.0×10^{-9}</u>	Value of soil stiffness and permeability in layer II are higher than layer I
III	A	1000	3000	<u>5.0×10^{-9}</u>	1000	3000	1.9×10^{-9}	Value of soil permeability in layer I is higher than layer II
	B	<u>3000</u>	<u>9000</u>	1.9×10^{-9}	1000	3000	1.9×10^{-9}	Value of soil stiffness in layer I is higher than layer II
	C	<u>3000</u>	<u>9000</u>	<u>5.0×10^{-9}</u>	1000	3000	1.9×10^{-9}	Value of soil stiffness and permeability in layer I are higher than layer II

The excess pore-pressure distributions for homogeneous and two soil layers are visualized in Figure 8. As expected, excess pore-pressure dissipation in the soil layer that has a high stiffness and permeability is faster than in the soil layer having a low stiffness and permeability. For the floating PVD conditions it is clear that the vertical flow is predominant in the unimproved area under the PVD tip, which has an influence on the consolidation time.

The settlement curves from the numerical model for PVD installation with varying the depth of penetration are shown in figures 9 and 10. It is clear that for a homogeneous layer (model 1), the drain length can be reduced by up to 20% without significantly affecting the consolidation

process ($L/H = 0.8$). This result corresponds to the report of Indraratna and Rujikiatkamjorn [7]. For the two-soil-layer condition where the second layer is stiffer and more permeable than the first layer (model 2; IIA, IIB, IIC), the drain length can be shortened by 30–40% without affecting the consolidation process ($L/H = 0.7 - 0.6$) significantly. In contrast, for the two-soil-layer condition where the first layer is stiffer and more permeable than the second layer (model 3; IIIA, IIIB, IIIC), the drain length can be reduced by only 10–20% without significantly affecting the consolidation process ($L/H = 0.9 - 0.8$). It is interesting to note that the differences in stiffness and permeability in the two-soil-layer condition have an influence on the optimum penetration depth (L/H), especially in the unimproved area below the PVD tip.

**Figure 8.** Excess pore-pressure distribution for homogeneous and two soil layers for double drainage conditions.

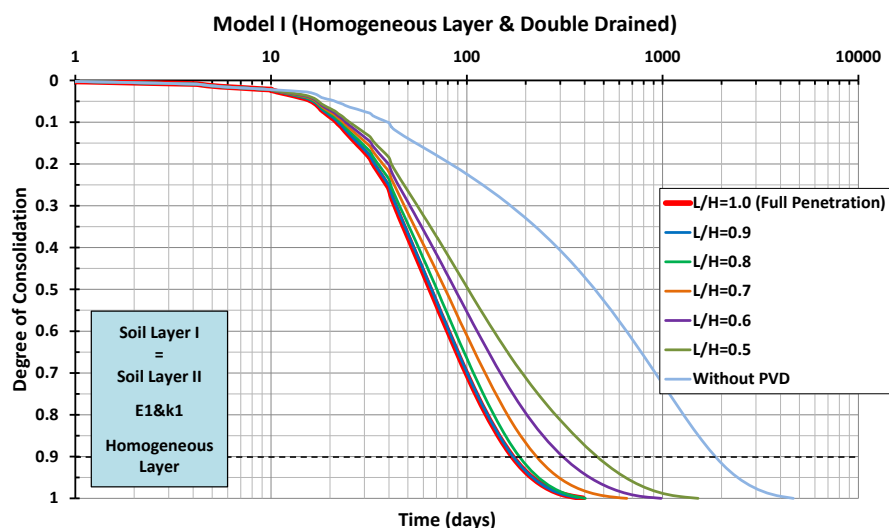


Figure 9. Settlement curves for homogeneous and double drainage conditions for varying PVD penetration depth.

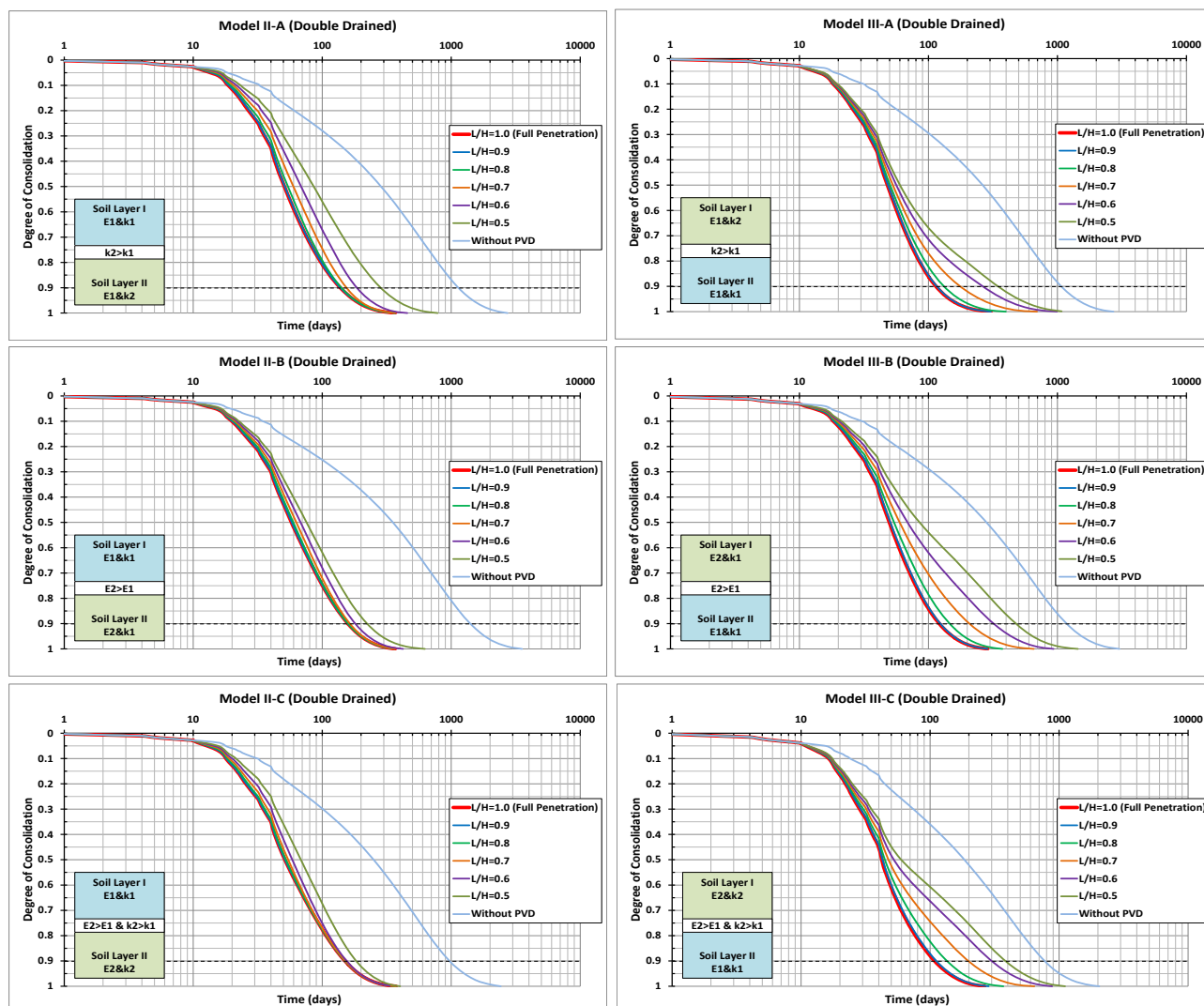


Figure 10. Settlement curves for two soil layers and double drainage conditions for varying PVD penetration depth.

4.2 SINGLE DRAINAGE CONDITION

In this section the effect of floating PVDs in single drainage, two-soil-layer conditions, on consolidation is numerically investigated. Here, no flow across the bottom boundary is allowed.

The excess pore-pressure distributions for the homogeneous and two-soil-layer conditions are shown in Figure 11. A similar picture as before is obtained, namely that the excess pore-water dissipation in the soil layer with a high stiffness and permeability is faster than in the soil layer with a low stiffness and permeability.

The settlement curves from the numerical model for a PVD installation with a varying depth of penetration are shown in figures 12 and 13. It is clear that for a homogeneous layer (model 1), the drain length can only be reduced by up to 10% without significantly affecting the consolidation process ($L/H = 0.9$). This is in line with Chai et al. [10], who suggested not choosing floating PVDs in one-way drainage conditions. For the two-soil-layer condition where the second layer is more stiff and permeable than the first layer (model 2; IIA, IIB, IIC), the drain length can be shortened by 15–25% without seriously affecting the consolidation process ($L/H = 0.85 - 0.75$). In contrast, for the two-soil-layer condition

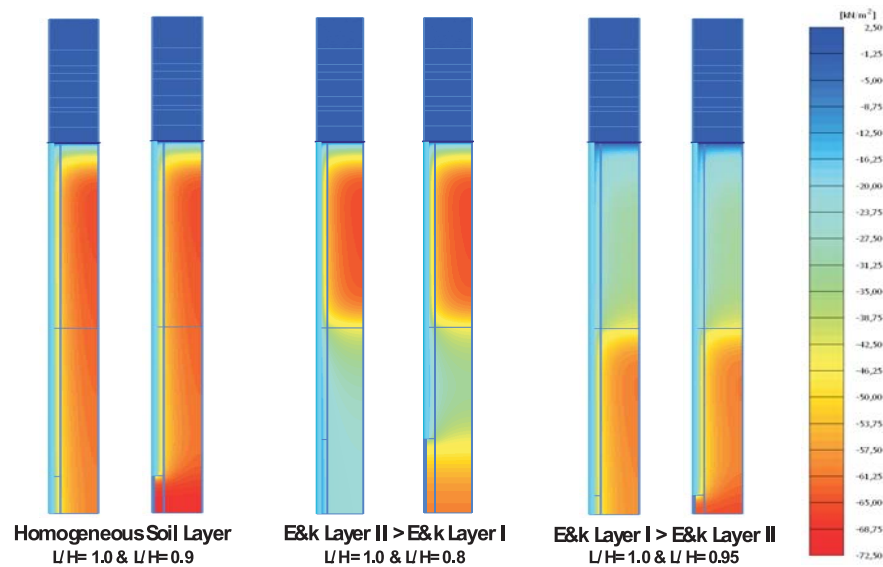


Figure 11. Excess pore-pressure distribution for homogeneous and two soil layers for single drainage condition.

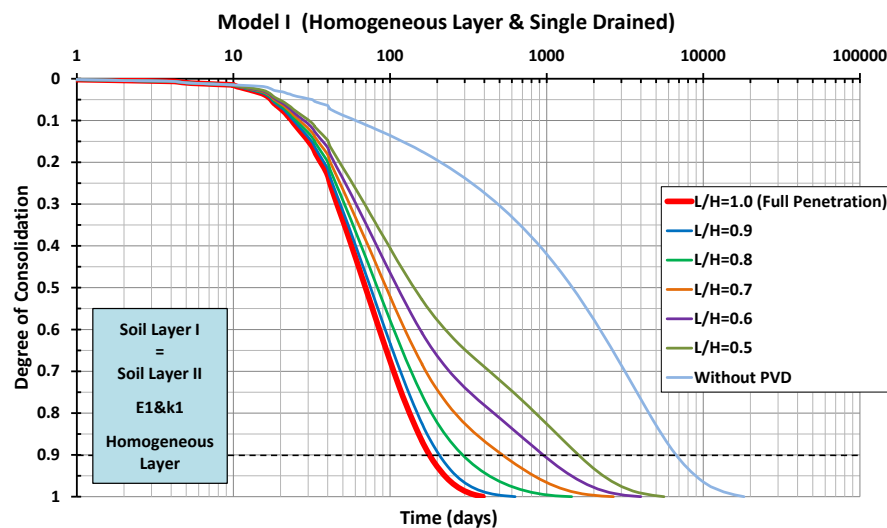


Figure 12. Settlement curves for homogeneous and single drainage conditions for varying PVD penetration depth.

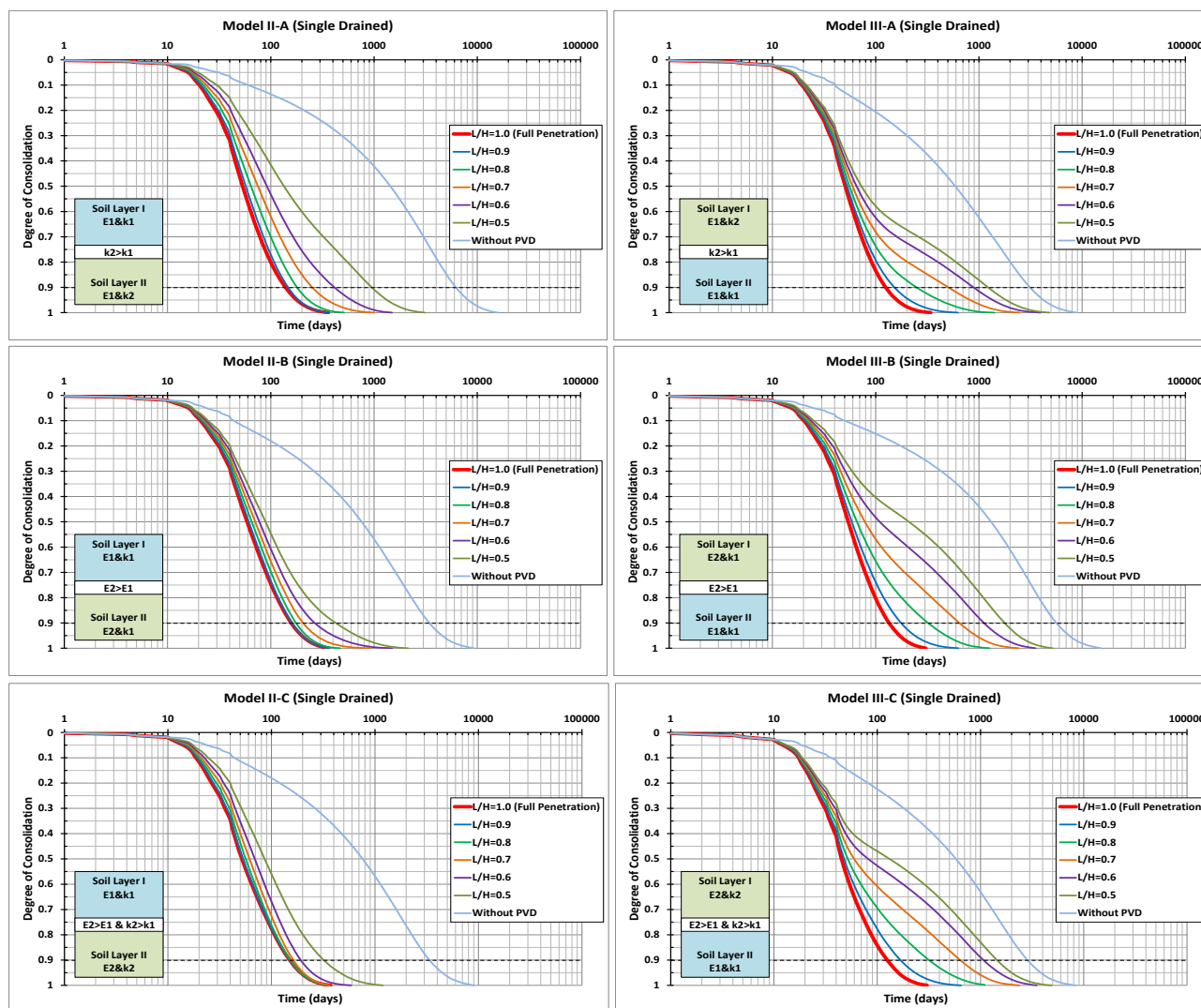


Figure 13. Settlement curves for two soil layers and single drainage condition for varying PVD penetration depth.

where the first layer is stiffer and more permeable than the second layer (model 3; IIIA, IIIB, IIIC), the drain length can only be reduced by about 10% without affecting the consolidation process ($L/H = 1.0-0.9$). Based on this numerical study it can be concluded that for single drainage conditions, only model 2, i.e., if the second layer is stiffer and more permeable than the first layer, can the use of floating PVDs be recommended.

5 CONCLUSIONS

Numerical results from a study of floating PVDs in two soil layers for double and single drainage conditions were examined to determine the optimum penetration depth for the PVDs. It is interesting to note that the differences in stiffness and permeability in the two-soil-layer condition, especially in the unimproved area below the PVD tip, have an influence on the optimum penetration depth

(L/H) in order to achieve the same consolidation time.

It was found in this study that for double drainage conditions in a homogeneous soil layer (model 1), the drain length can be reduced by up to 20% without significantly affecting the consolidation process ($L/H = 0.8$). For a two-soil-layer condition where the second layer is stiffer and more permeable than the first layer (model 2; IIA, IIB, IIC), the drain length can be shortened by 30–40% ($L/H = 0.7-0.6$). In contrast, for a two-soil-layer condition where first layer is stiffer and more permeable than the second layer (model 3; IIIA, IIIB, IIIC), the drain length can be reduced by only 10–20% ($L/H=0.9-0.8$). For single drainage conditions it is possible to use a floating PVD only if the second layer is stiffer and/or more permeable than the first layer.

This study has shown that a good agreement between field measurements and numerical predictions for settlements in both full and partial penetration conditions

can be achieved. For the presented case study the drain length could be reduced by up to 30% without significantly affecting the consolidation process ($L/H = 0.7$).

ACKNOWLEDGEMENTS

The authors wish to thank PT. Soilens, PT. Doosan Heavy Industries Indonesia, PT. Cirebon Electric Power, PT. Tripatra Engineers and Constructors for providing the case-study data in this paper. The authors would also like to thank Ir. Padmono, P.E., (PT. Soilens Bandung) for his time during a detailed discussion of the site conditions and parameters. The work reported in this paper was supported by North-South-Dialogue scholarship programme from Österreichische Akademische Austauschdienst (ÖAD) for the first author as part of a Ph.D. study at Graz University of Technology, Austria.

REFERENCES

- [1] Barry, A.J., Rahadian, H., Rachlan, A. (2002). The Indonesian geoguides. *Symposium on Geotechnical Engineering*, Bangkok.
- [2] Runesson, K., Hansbo, S., Wiberg, N.E. (1985). The efficiency of partially penetrating vertical drains. *Géotechnique Journal*, Vol. 35, No. 4, pp. 511-516.
- [3] Onoue, A. (1988). Consolidation of multilayered anisotropic soils by vertical drains with well resistance. *Journal of The Japanese Geotechnical Society: Soils and Foundations*, Vol. 28, No. 3, pp. 75-90.
- [4] Nakano, H., Okuie, H. (1991). Consolidation by using a long drainage wells with partial penetration. *Journal of The Japanese Geotechnical Society: Soils and Foundations*, Vol. 39, No. 8, pp. 23-28.
- [5] Tang, X.W., Onitsuka, K. (1998). Consolidation of ground with partially penetrated vertical drains. *International Journal of Geotechnical Engineering*, Vol. 29, No. 2, pp. 209-231.
- [6] Tang, X.W. (2004). Comparison of partially penetrated open and closed ended vertical drains. *Proceeding of the 3rd Asian Regional Conference on Geosynthetics: Now and Future of Geosynthetics in Civil Engineering*, Seoul, pp. 291-297.
- [7] Indraratna, B., Rujikiatkamjorn, C. (2008). Effects of partially penetrating prefabricated vertical drains and loading patterns on vacuum consolidation, In: Reddy, K.R., Khire, M.V., Alshawabkeh, A.N. (Eds.). *Proceeding of the GeoCongress: Geosustainability and Geohazard Mitigation*, ASCE, Orleans, pp. 596-603.
- [8] Hart, E.G., Kondner, R.L., Boyer, W.C. (1958). Analysis for partially penetrating sand drains. *Journal of Soil Mechanics and Foundation Division: Proceedings of ASCE*, Vol. 84, No. 4, pp. 1-15.
- [9] Zeng, G.X., Xie, K.H. (1989). New development of the vertical drain theories. *Proceeding of the 12th ICSMFE*, Rio de Janeiro, Vol. 2, pp. 1435-1438.
- [10] Chai, J.C., Miura, N., Kirekawa, T., Hino, T. (2009). Optimum PVD installation depth for two-way drainage deposit. *International Journal of Geomechanics and Engineering*, Vol. 1, No. 3, pp. 179-191.
- [11] Geng, X.Y., Indraratna, B., Rujikiatkamjorn, C. (2011). Effectiveness of partially penetrating vertical drains under a combined surcharge and vacuum preloading. *Canadian Geotechnical Journal*, Vol. 48, pp. 970-983.
- [12] Unsworth, R. (Eds). (2008). Marine environment report of the Cirebon IPP coal fired power station for PT. Cirebon Electric Power. Sinclair Knight Merz, Brisbane. (QE09421.02).
- [13] Padmono, P. (Eds). (2008a). Review of settlement instrumentation report of the 1x660 MW coal fired Cirebon power plant project for PT. Doosan Heavy Industries Indonesia. PT. Soilens, Bandung. (2238-B & 2428).
- [14] Padmono, P. (Eds). (2008b). Soil investigation II report of the 1x660 MW coal fired Cirebon power plant project for PT. Doosan Heavy Industries Indonesia. PT. Soilens, Bandung. (2338-B & 2428).
- [15] Barry, A.J., Rachlan, A. (2001). Embankments on soft soils in North Java. *Proceeding of International Conference on In Situ Measurement of Soil Properties and Case Histories*, Bali.
- [16] Barry, A.J., Rahadian, H., Rachlan, A. (2003). The embankments on North Java soft clay. *Proceeding of the 12th Asian Regional Conference*, Singapore.
- [17] Padmono, P. (Eds). (2006). Preliminary soil investigation report of the IPP 1x660 MW coal fired steam Cirebon power plant project for PT. Tripatra Engineers and Constructors. PT. Soilens, Bandung.
- [18] Padmono, P. (Eds). (2007). Soil investigation I report of the Cirebon thermal power plant project for PT. Cirebon Electric Power. PT. Soilens, Bandung. (2338 & 2358).
- [19] Brinkgreve, R.B.J., Swolf, W.M., Engin, E. (Eds). (2010). Plaxis 2D 2010 user manual: Finite element code for soil and rock analyses. Plaxis bv., Netherland.
- [20] Schanz, T., Vermeer, P.A., Bonnier, P.G. (1999). The hardening soil model: formulation and verification. *Proceeding of the International Symposium Beyond 2000 in Computational Geotechnics – 10 Years of Plaxis*, Amsterdam, pp. 281-296.
- [21] Hansbo, S. (1979). Consolidation of clay by band-shaped prefabricated drains. *Ground Engineering*, Vol. 12, No. 5, pp. 16-25.
- [22] Chai, J.C., Miura, N. (1999). Investigation of factors affecting vertical drain behavior. *Journal of Geotechnical and Geoenvironmental Engineering*, Vol. 125, No. 3, pp. 216-226.

NOV NAČIN ANALIZIRANJA PLITKIH IN GLOBOKIH TUNELOV OB UPOŠTEVANJU GRAVITACIJE

MOHAMMAD REZA ZAREIFARD IN AHMAD FAHIMIFAR

o avtorjih

Mohammad Reza Zareifard
Amirkabir University of Technology
Teheran, Iran
e-pošta: zareifard@aut.ac.ir

vodilni avtor

Ahmad Fahimifar
Amirkabir University of Technology
Teheran, Iran
e-pošta: fahim@aut.ac.ir

izvleček

Članek predstavlja novo analitično-numerično rešitev za krožni tunel v deformacijsko popuščajóci in Hoek-Brownovi hribini, ob upoštevanju pogojev osne simetrije. Izpeljani so izrazi za določitev sprememb začetne napetosti in robnih pogojev površine tal v različnih smereh okrog tunela. Pri tem so upoštevani tudi vplivi teže v plastični coni. Ker izpeljane diferencialne enačbe ne predstavljajo eksplicitne analitične rešitve za plastično cono, se v študiji uporablja metoda končnih razlik (MKR). Izpeljani pa so analitični izrazi za elastično cono. Učinkovitost predlagane rešitve in učinek različnih robnih pogojev sta ponazorjena z več pojasnjevalnimi primeri. Ugotovljeno je, da dajejo klasične rešitve, ki temeljijo na oddaljeni hidrostatični talni napetosti in zanemarjajo vpliv robnih pogojev na površini tal, uporabne rezultate za veliko praktičnih problemov. Vendar pa lahko neupoštevanje teže v plastični coni v analizah privede do velikih napak v izračunih.

ključne besede

krivulja odziva tal, elasto-plastična analiza, robni pogoji, osna simetrija, gravitacija

A NEW SOLUTION FOR SHALLOW AND DEEP TUNNELS BY CONSIDERING THE GRAVITATIONAL LOADS

MOHAMMAD REZA ZAREIFARD AND AHMAD FAHIMIFAR

about the authors

Mohammad Reza Zareifard
Amirkabir University of Technology
Tehran, Iran
E-mail: zareefard@aut.ac.ir

corresponding author

Ahmad Fahimifar
Amirkabir University of Technology
Tehran, Iran
E-mail: fahim@aut.ac.ir

abstract

A new, elasto-plastic, analytical-numerical solution, considering the axial-symmetry condition, for a circular tunnel excavated in a strain-softening and Hoek–Brown rock mass is proposed. To examine the effect of initial stress variations, and also the boundary conditions at the ground surface, the formulations are derived for different directions around the tunnel. Furthermore, the effect of the weight of the plastic zone is taken into account in this regard. As the derived differential equations have no explicit analytical solutions for the plastic zone, the finite-difference method (FDM) is used in this study. On the other hand, analytical expressions are derived for the elastic zone. Several illustrative examples are given to demonstrate the performance of the proposed solution, and to examine the effect of various boundary conditions. It is concluded that the classic solutions, based on the hydrostatic far-field stress, and neglecting the effect of the boundary conditions at the ground surface, give applicable results for a wide range of practical problems. However, ignoring the weight of the plastic zone in the analyses can lead to large errors in the calculations.

keywords

ground-response curve, elasto-plastic analysis, boundary condition, axial symmetry, gravitational loads

1 INTRODUCTION

A number of methods are currently used for the design and analysis of tunnels. Among them, the convergence-confinement method (the C.-C. method) has played an important role in providing an insight into the interaction between the lining support and the surrounding ground mass. The C.-C. method is based on a concept that involves an analysis of the ground-structure interaction by independent studies of the behavior of the ground and of the tunnel support. In this regard, the ground behavior is represented by a ground-response curve; which describes the ground convergence in terms of the applied internal pressure. However, to maintain simplicity, a number of simplifying assumptions are made in its derivation. These assumptions make the method applicable only to deep tunnels in hydrostatic stress fields. In the past, a number of classic solutions for determining the ground-response curve have been published. These solutions may be categorized into two groups of analytical closed-form solutions and analytical-numerical unclosed-form solutions. Although a number of closed-form solutions are available (such as that proposed by Brown et al. [1]; Sharan [2]; Carranza-Torres [3]; Park and Kim [4]), each solution suffers from a level of approximation in the sense that it incorporates various simplifying assumptions. For example, these solutions have been proposed for the rock masses with simpler behavior models, including the elastic-perfect-plastic or elastic-brittle-plastic behavior models. In fact, for more complicated behavior models obtaining an exact closed-form solution is impossible. On the other hand, in the unclosed-form solutions (Brown et al., [1]; Guan et al., [5]; Lee and Pietruszczak, [6]; Fahimifar and Zareifard, [7]), consideration of more complicated and general material-behavior models are possible.

However, all the mentioned solutions (both the closed- and unclosed-form solutions) are based on the classic assumptions made in the C.-C. method. Different aspects of the C.-C. method have been investigated by researchers, both analytically and numerically.

With the development of computer codes, numerical analyses have become common methods for the analysis of tunnels. Various cases of analyses, including two-dimensional, three-dimensional and time-dependent behaviors, can be performed using commercial codes. Nevertheless, utilizing numerical methods for investigating the C.-C. method, such as that presented by Carranza-Torres and Fairhurst [8] and that presented by Gonzalez-Nicieza et al. [9], do not easily reveal the actual effects that the simplifying assumptions have on the mechanical response of a tunnel. Therefore, analytical solutions of simpler cases, such as that proposed by Lu et al. [10], Detournay and Fairhurst [11], and Reed [12], can help to realize various aspects of the ground-response curve of tunnels much better.

In the C.-C. method the effects of the boundary conditions at the ground surface are neglected and, also, the variation of the initial stresses (i.e., in-situ stresses) are not taken into account, classically. However, for shallow tunnels, the initial stresses cannot be assumed to be constant over the tunnel section, and thus the assumption of hydrostatic, far-field stresses may not be applicable. On the other hand, in the C.-C. method, the above solutions neglect the weight of the plastic zone developed around the tunnel. However, very few works concerning the effect of gravitational forces acting on the ground have been conducted [13-15]. In fact, gravitational loading differs for various directions around the tunnel periphery, and, for the same internal pressure, convergence of the crown is expected to be larger than that of the walls, because of the weight of the failed material on the top of the tunnel.

In this paper, an unclosed-form analytical solution is presented for the stress and displacement fields

around a circular tunnel excavated in an elasto-plastic strain-softening and Hoek–Brown rock material. In this method the effects of boundary conditions at the free surface of the ground, and also the effect of the weight of the plastic zone are taken into account. For this purpose, the formulations are derived for both the horizontal and the vertical directions that are passing through the tunnel center. In addition, the gravitational loadings are considered as radial body forces being applied to the rock mass.

2 ANALYTICAL SOLUTION OF TUNNELS CONSIDERING THE GRAVITATIONAL LOADS

Fig. 1 shows the general case of a tunnel excavated in a homogeneous and isotropic rock mass under an in-situ stress field below a horizontal ground surface.

In general cases the initial stresses in the Cartesian coordinate system are $\sigma_y = \gamma y + p_s$ and $\sigma_x = \sigma_z = K\sigma_y$, where x , y and z are the Cartesian coordinate axes (as shown in Fig. 1), γ is the specific weight of the rock, K is the so-called lateral stress coefficient, and p_s is the uniform vertical stress that is applied to the ground surface from infrastructures or embankments (surcharge load). In cylindrical coordinates (r, θ, z) , the stress field around a tunnel (see Fig. 2) has to fulfill the equilibrium equations for each element of the rock mass, as in [16]:

$$\frac{\partial \sigma_{rr}}{\partial r} + \frac{1}{r} \frac{\partial \sigma_{\theta r}}{\partial \theta} - \frac{\sigma_{\theta\theta} - \sigma_{rr}}{r} + F_r = 0 \quad (1)$$

$$\frac{\partial \sigma_{r\theta}}{\partial r} + \frac{1}{r} \frac{\partial \sigma_{\theta\theta}}{\partial \theta} + \frac{\sigma_{r\theta} + \sigma_{\theta r}}{r} + F_\theta = 0 \quad (2)$$

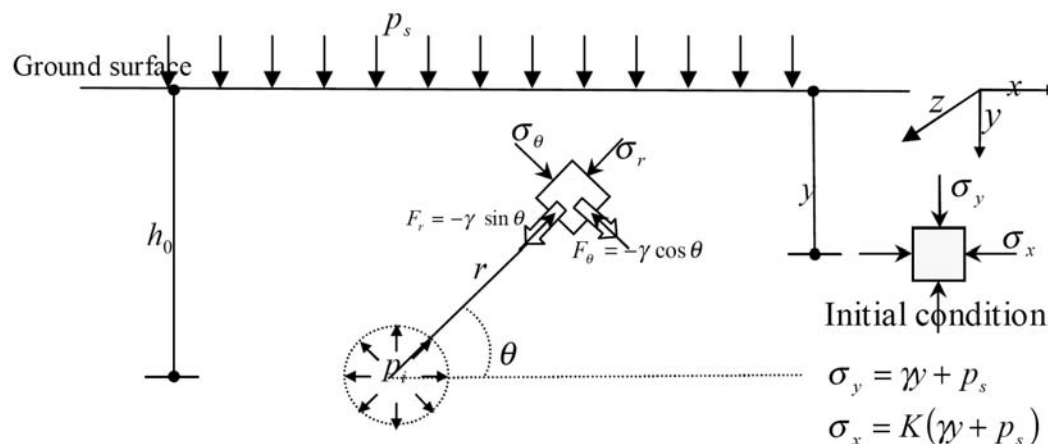


Figure 1. Circular shallow tunnel in a semi-infinite medium under an initial stress field.

where $F_r = -\gamma \sin\theta$, and $F_\theta = -\gamma \cos\theta$ are the gravitational body forces in the radial and circumferential directions, respectively, γ is the unit weight of the ground and θ is the angle measured clockwise from the horizontal direction.

Obtaining an exact elasto-plastic analytical solution for this problem is extremely complicated and even unsolvable in more cases (as shown by Detournay and Fairhurst [11]), because, in this case, the principal stresses may rotate in each direction.

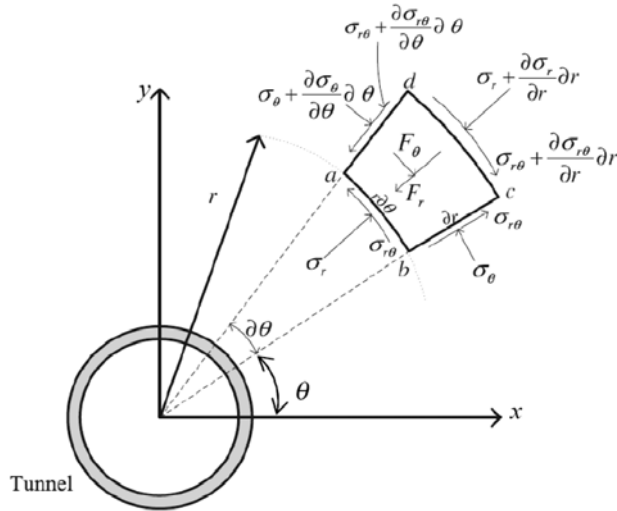


Figure 2. Body forces and stress components corresponding to an element of the rock mass.

As mentioned in the C.-C. method for simplifying the problem, the ground-response curve is constructed based on the elasto-plastic solution for a circular opening subjected to hydrostatic far-field stresses and a uniform internal pressure (see Fig. 3).

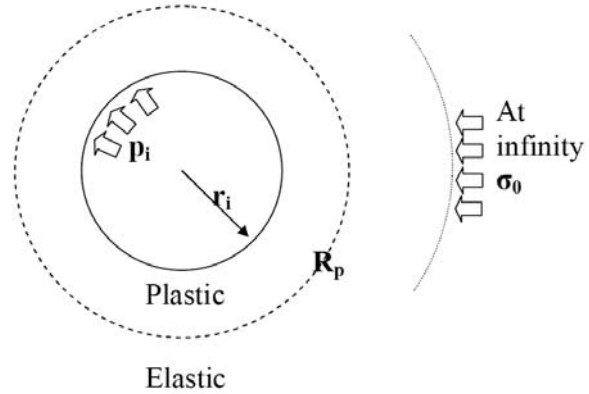


Figure 3. Circular deep tunnel excavated in a hydrostatic stress field.

Thus, in equilibrium Eq. (1) the term $\frac{1}{r} \frac{\partial \sigma_{\theta r}}{\partial \theta}$ vanishes. In this case it is assumed that the initial stresses in the vicinity of the tunnel are constant $\sigma_{y0} = \sigma_{x0} = \gamma h_0 + p_s$ and do not increase linearly.

In this paper an analytical solution for deriving the ground-response curve of a tunnel under equal initial stresses ($K = 1$) is proposed by considering the effects of the initial stress variations due to the gravitational loads and taking the effects of the boundary conditions into account at the free surface of the ground. In this solution the analyses are performed for the horizontal and the vertical directions for axial symmetry conditions (see Fig. 4). Thus, the term $\frac{1}{r} \frac{\partial \sigma_{\theta r}}{\partial \theta}$ will vanish. In this regard, the governing equilibrium equation becomes more straightforward as:

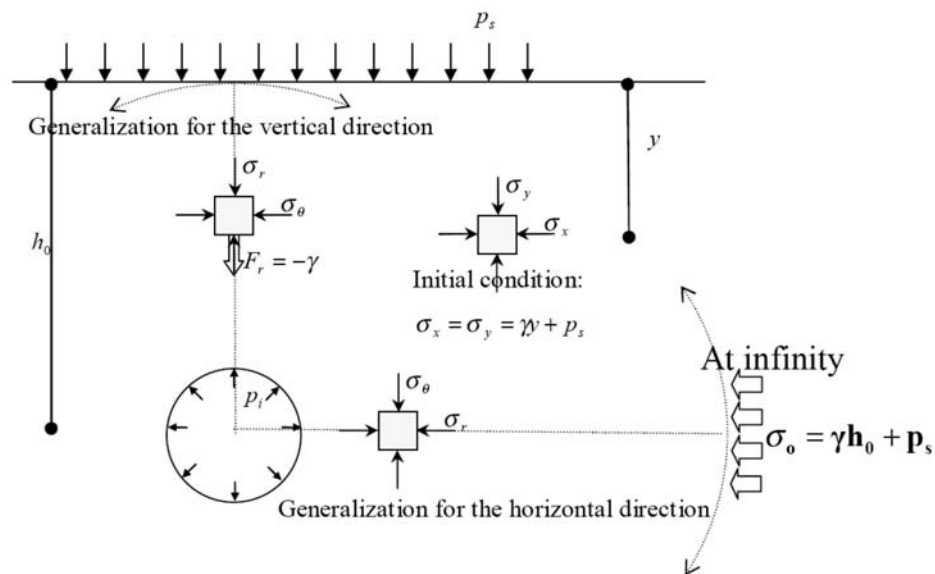


Figure 4. Analysis of the shallow tunnels along the horizontal and the vertical directions by considering the axial symmetry condition.

$$\frac{d\sigma_r}{dr} - \frac{\sigma_\theta - \sigma_r}{r} + F_r = 0 \quad (3)$$

where F_r is the applied radial body force, which depends on the gravitational loads through the considering direction. As mentioned, since the axial symmetry condition is assumed, only the radial component of the gravitational loads, i.e., $F_r = -\gamma \sin\theta$, is taken into account, and the circumferential component is neglected. Thus, $F_r = -\gamma$ for the vertical direction and $F_r = 0$ for the horizontal direction are obtained (see Fig. 4).

For the polar coordinates defined in Fig. 1, the initial equal stress field ($K = 1$) is given by:

$$\sigma_{0(r,\theta)} = \sigma_{r0(r,\theta)} = \sigma_{\theta0(r,\theta)} = \gamma y + p_s = \gamma(h_0 - r \sin\theta) + p_s \quad (4)$$

where $\sigma_{\theta0}$ and σ_{r0} are the initial circumferential and radial stresses, respectively, and p_s is the surcharge load. It should be noted that when there is a very weak or a heavily weathered layer of rock or residual soils on the upper levels, their effect can be considered as surcharge loads applied to the underlying ground.

In this study, the formulations are derived for both the horizontal (through the tunnel springline) and the vertical (through the tunnel crown) directions. In this manner, for both directions, because of the axial symmetry conditions, the geometry, boundary conditions and

the applied loads are generalized to all directions (see Fig. 4). The problem for both the horizontal and vertical directions are shown in Figs. 5(a) and 5(b), respectively.

As observed in Figs. 4 and 5(a), for the horizontal direction, the problem is similar to a circular tunnel in an infinite medium. In this case, at the tunnel radius (i.e., at $r = r_i$) the internal pressure p_i is applied, and at an infinite radius (i.e., at $r = \infty$), the pressure $\gamma h_0 + p_s$ is applied. In addition, the radial body forces through this direction are equal to zero. It is observed that this case is similar to the problem of a deep tunnel. On the other hand, as observed in Figs. 4 and 5(b), for the vertical direction, the problem of a thick-walled cylinder is the result. In this case, at the tunnel radius the internal pressure p_i is applied, and at radius $r = h_0$, the pressure p_s is applied. Furthermore, the radial body forces through this direction are $F_r = -\gamma$.

As shown in Fig. 5, two different zones may be formed around the tunnel (for both directions): the external elastic zone, and the internal plastic zone, which may be divided into the softening zone and the residual zone.

The strain–displacement relations in the polar coordinate system for the axial symmetric problem are given by [17]:

$$\varepsilon_\theta = \frac{u_r}{r}, \quad \varepsilon_r = \frac{du_r}{dr} \quad (5)$$

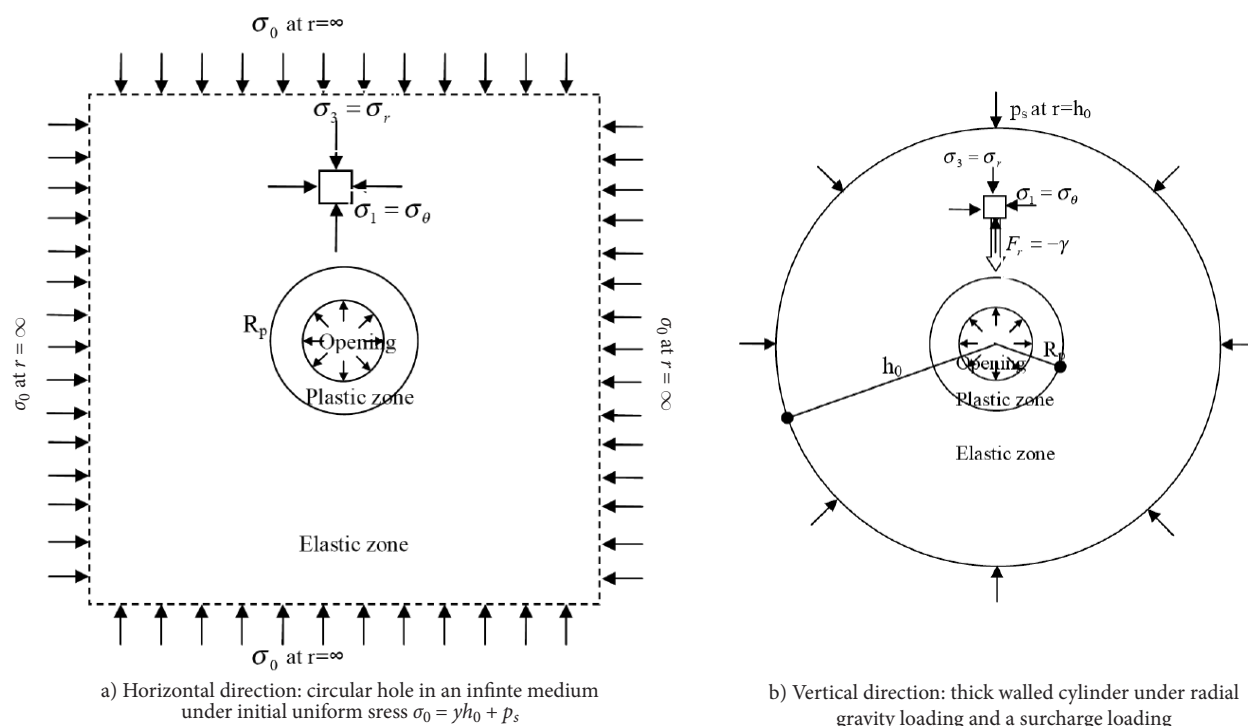


Figure 5. Geometry, applied loads and boundary conditions for the horizontal and vertical directions.

where u_r is the radial component of the displacement and ε_θ and ε_r are the circumferential and radial strains, respectively.

Furthermore, the stress state at a distance r is defined by the radial stress σ_r and the circumferential stress σ_θ , which are the minor σ_3 and the major σ_1 principal stresses, respectively, as shown in Fig. 5.

3 BEHAVIOR MODEL

The rock mass is assumed to exhibit the strain-softening behavior, in this study, which can be reduced to the perfect elasto-plastic or elasto-brittle-plastic cases. Generally, this behavior is characterized by a transitional failure criterion and a plastic potential. A softening parameter controls the gradual transition from an initial failure criterion (or a potential one) to a residual one. In the present work, the deviatoric plastic strain $\gamma^p = \varepsilon_\theta^p - \varepsilon_r^p$ is employed as the softening parameter. Although there is no universal way of defining the strain-softening parameter, as pointed out by Alonso et al. [18], the above softening parameter is the most widely accepted.

The plastic strain increments can be obtained from the plastic potential function, $g(\sigma_r, \sigma_\theta, \gamma^p)$ according to:

$$\dot{\varepsilon}_r^p = \dot{\lambda} \frac{\partial g}{\partial \sigma_r} \quad (6)$$

and:

$$\dot{\varepsilon}_\theta^p = \dot{\lambda} \frac{\partial g}{\partial \sigma_\theta} \quad (7)$$

where $\dot{\lambda}$ is a plastic multiplier, $\dot{\varepsilon}_r^p = \frac{\partial \varepsilon_r^p}{\partial \tau}$ and $\dot{\varepsilon}_\theta^p = \frac{\partial \varepsilon_\theta^p}{\partial \tau}$ (τ is a fictitious 'time' variable). Equations (6) and (7) are the constitutive equations in the plastic regime, and are usually termed the flow rule. If the plastic potential coincides with the failure criterion, then it is called an associated flow rule; otherwise it is called a non-associated flow rule. In this regard the incremental plasticity involves a consideration of a fictitious 'time' variable, even if it does not have any physical meaning. This variable controls the evolution of the plasticity and the plastic strain rates. In the formulation presented in this research, the plastic radius, R_p , will be assumed to be the time variable. This choice allows the acquisition of a simple formulation for the problem, in order to obtain a certain kind of solution, as illustrated by Alonso et al. [18].

Here, the Mohr–Coulomb criterion is selected as a plastic potential function for a non-associated flow rule:

$$g = \sigma_\theta - K_\psi \sigma_r \quad (8)$$

where K_ψ is the dilation factor, and is given as:

$$K_\psi = \frac{1 + \sin \Psi_g}{1 - \sin \Psi_g} \quad (9)$$

Ψ_g , in Eq. (9), is termed the dilation angle and varies as a function of the softening parameter γ^p .

The rock mass is assumed to obey the Hoek–Brown failure criterion, given by [19]:

$$\sigma_\theta - \sigma_r = (m\sigma_c\sigma_r + s\sigma_c^2)^{\frac{1}{2}} \quad (10)$$

in which σ_θ is the circumferential stress, σ_r is the radial stress, σ_c is the uniaxial compressive strength of the intact rock material, and m and s are the Hoek–Brown constants that depend on the properties of the rock mass and the extent to which it was broken before being subjected to the failure stresses σ_θ and σ_r .

For the plastic zone, the above equation is given as:

$$\sigma_\theta - \sigma_r = (m_g\sigma_r\sigma_c + s_g\sigma_c^2)^{\frac{1}{2}} \quad (11)$$

where m_g and s_g are the Hoek–Brown constants for the plastic zone and vary as a function of the softening parameter γ^p .

In contrast to the solution presented by Brown et al. [1], the solution proposed in this work considers the elastic strains induced in the plastic zone. The relationships between the elastic strains ε_r^e , and ε_θ^e , and the stresses σ_r and σ_θ are given by Hooke's law [17]:

$$\varepsilon_r^e = \frac{1+\nu}{E_g} [(1-\nu)(\sigma_r - \sigma_0) + \nu(\sigma_\theta - \sigma_0)] \quad (12)$$

$$\varepsilon_\theta^e = \frac{1+\nu}{E_g} [(1-\nu)(\sigma_\theta - \sigma_0) + \nu(\sigma_r - \sigma_0)] \quad (13)$$

where σ_0 is the initial stress, and calculating from Eq. (4), E_g and ν are the elasticity modulus and the Poisson's ratio of the rock mass, respectively. However, for the plastic zone, the elasticity modulus E_g varies as a function of the softening parameter γ^p .

It should be noted that in the plastic zone, the failure and dilation parameters, appearing in Eqs. (9) and (11), and also the rock mass elastic modulus appearing in Eqs. (12) and (13), can be described by a bilinear function based on the deviatoric plastic strain γ^p :

$$\omega = \begin{cases} \omega_i - (\omega_i - \omega_r) \frac{\gamma^p}{\gamma^{p*}} & 0 < \gamma^p < \gamma^{p*} \\ \omega_r & \gamma^p \geq \gamma^{p*} \end{cases} \quad (14)$$

where ω represents one of the parameters m_g , s_g , Ψ_g and E_g , and γ^{p*} is the critical deviatoric plastic strain from

which the residual behavior starts, and should be identified by experiments. The subscripts 'i' and 'r' denote the initial and residual values, respectively.

4 ANALYSIS OF THE PLASTIC ZONE

For both cases (the horizontal and the vertical directions) a plastic zone of radius R_p will be formed around the tunnel. The governing equations on the plastic zone are similar, but not identical, for both cases.

It is important to highlight that the strains and stresses in the plastic zone depend on two factors: on a physical variable r , which is the distance to the centre of the excavation; and on a fictitious 'time' variable $\tau = R_p$, which is a measure of the plasticity evolution. In this regard, the dimensionless variable ρ is considered, that maps the physical plane (r, τ) into a plane of coordinate ρ according to the following transformation (see Fig. 6):

$$\rho = \frac{r}{\tau} \text{ or } \rho = \frac{r}{R_p} \quad (15)$$

Based on the above transformation, the solutions for the strain and stress fields do not depend on the plastic radius.

In this regard, the equilibrium Eq. (3) can be expressed with respect to the normalized radius $\rho = \frac{r}{R_p}$ as:

$$\frac{d\sigma_r}{d\rho} - \frac{\sigma_\theta - \sigma_r}{\rho} + F_r R_p = 0 \quad (16)$$

where F_r is the radial body force. F_r is equal to $-\gamma$ for the vertical direction, and it is equal to zero for the horizontal direction (see Fig. 5).

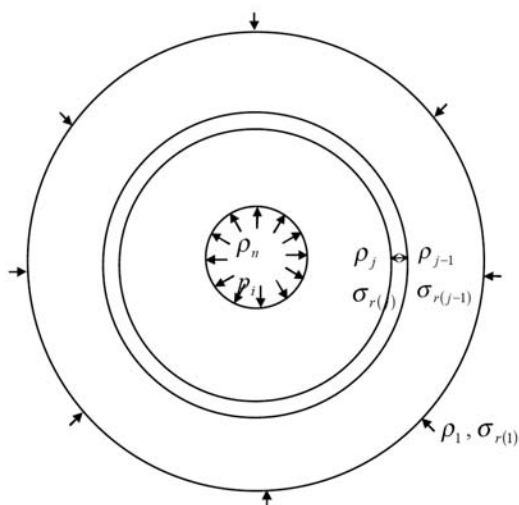


Figure 6. Normalized plastic zone with a finite number of annular elements.

A combination of the failure criterion, i.e., Eq. (11), and equilibrium equation, i.e., Eq. (16), gives:

$$\frac{d\sigma_r}{d\rho} + F_r R_p = \frac{(m_g \sigma_r \sigma_c + s_g \sigma_c^2)^{\frac{1}{2}}}{\rho} \quad (17)$$

It is assumed that in the plastic zone the total strains consist of the elastic and plastic parts:

$$\varepsilon_r = \varepsilon_r^e + \varepsilon_r^p, \quad \varepsilon_\theta = \varepsilon_\theta^e + \varepsilon_\theta^p \quad (18)$$

where ε_r and ε_θ are total radial and circumferential strains, respectively, and the superscripts e and p denote the elastic and plastic parts of the strains, respectively.

Thus, the total strain rates $\dot{\varepsilon}_\theta$ and $\dot{\varepsilon}_r$ can be written in terms of the elastic ($\dot{\varepsilon}_\theta^e, \dot{\varepsilon}_r^e$) and plastic ($\dot{\varepsilon}_\theta^p, \dot{\varepsilon}_r^p$) components as:

$$\dot{\varepsilon}_r = \dot{\varepsilon}_r^e + \dot{\varepsilon}_r^p, \quad \dot{\varepsilon}_\theta = \dot{\varepsilon}_\theta^e + \dot{\varepsilon}_\theta^p \quad (19)$$

where the dot denotes the derivative of strain with respect to the fictitious time variable $\tau = R_p$ ($\dot{\varepsilon} = \frac{\partial \varepsilon}{\partial \tau}$), and ε_r^e and ε_θ^e are obtained using Hooke's law, i.e., Eqs. (12) and (13).

For the Mohr-Coulomb type of plastic potential function (8), elimination of the plastic multiplier λ from the flow rule, i.e., equations (6) and (7), gives the relation between the plastic parts of the radial and circumferential strain rates as follows:

$$\dot{\varepsilon}_r^p + K_\psi \dot{\varepsilon}_\theta^p = 0 \quad (20)$$

where the coefficient of dilation K_ψ is obtained from Eq. (9).

Based on the given transformation (Eq. (15)), the partial derivatives of the field functions with respect to the variables r and $\tau = R_p$ are evaluated with the operators:

$$\frac{\partial(\cdot)}{\partial r} = \frac{1}{R_p} \frac{\partial(\cdot)}{\partial \rho} \quad (21)$$

$$\frac{\partial(\cdot)}{\partial \tau} = -\frac{\rho}{R_p} \frac{\partial(\cdot)}{\partial \rho} \quad (22)$$

Eliminating u_r from Eqs. (5) by applying Eqs. (15) and (21) develops the simple compatibility equation:

$$\varepsilon_r = \rho \varepsilon_\theta' + \varepsilon_\theta \quad (23)$$

where ε' is defined as:

$$\varepsilon' = \frac{d\varepsilon}{d\rho} \quad (24)$$

Since a multi-linear behavior model and the incremental theory of plasticity have been used, the governing equa-

tions on the stresses and strains in the plastic zone have no analytical solutions, and must be solved numerically, as presented in Appendix A.

Defining the stresses and strains on the outer boundary of the plastic zone, where $\rho = \rho_1 = 1$, successive values of the stresses and strains are calculated from the formulations presented in Appendix A by successive increments of ρ_j (see Fig. 6) until the value of the radial stress for a specific ρ_n (i.e. $\sigma_{r(n)}$) reaches p_i .

Thus, for an analysis of the plastic zone it is necessary to calculate the boundary stresses at the external radius of the plastic zone (plastic radius) by considering the interactions between the elastic and plastic zones.

5 ANALYSIS OF THE ELASTIC ZONE

It should be noted that the tunnel excavation induces additional stresses on the rock mass initially subjected to equal field stresses; thus, the final stresses in the rock mass will be equal to the sum of the initial stresses and the induced stresses.

As the excavation is taking place, the stresses $\delta\sigma_\theta$ and $\delta\sigma_r$ are induced in the rock mass. By reducing the initial portion of the stresses from equilibrium Eq. (3), the governing equilibrium equation in terms of the induced stresses $\delta\sigma_r$ and $\delta\sigma_\theta$ is given by:

$$\frac{d\delta\sigma_r}{dr} - \frac{(\delta\sigma_\theta - \delta\sigma_r)}{r} = 0 \quad (25)$$

In the elastic zone, Hooke's law for plane-strain conditions can be used between the induced stresses and strains [17]:

$$\delta\sigma_r = \frac{E_0}{(1+\nu)(1-2\nu)} [(1-\nu)\varepsilon_r + \nu\varepsilon_\theta] \quad (26)$$

$$\delta\sigma_\theta = \frac{E_0}{(1+\nu)(1-2\nu)} [(1-\nu)\varepsilon_\theta + \nu\varepsilon_r] \quad (27)$$

A combination of the equilibrium equation (25) with the above equations (Eqs. (26) and (27)); and then applying the strain-displacement Eqs. (5), gives the following equation for the unknown radial displacement u_r :

$$-\frac{u_r}{r^2} + \frac{1}{r} \frac{du_r}{dr} + \frac{d^2u_r}{dr^2} = 0 \quad (27)$$

This differential equation has an analytical solution for the elastic zone by applying the boundary conditions at the internal and external radii. The boundary conditions are different for both cases (the horizontal and vertical

directions) (see Fig 5), and thus the corresponding analytical formulations will be different.

For the case of the horizontal direction:

$$\delta\varepsilon_{r(r)} = -\delta\varepsilon_{\theta(r)} = \frac{1+\nu}{E_0} \delta\sigma_{r(R_p)} \frac{R_p^2}{r^2} \quad (28)$$

$$\delta\sigma_{r(r)} = -\delta\sigma_{\theta(r)} = \delta\sigma_{r(R_p)} \frac{R_p^2}{r^2} \quad (29)$$

For the case of vertical direction:

$$\delta\sigma_{r(r)} = -\delta\sigma_{r(R_p)} \frac{R_p^2}{h_0^2 - R_p^2} \left(1 - \frac{h_0^2}{r^2}\right) \quad (30)$$

$$\delta\sigma_{\theta(r)} = -\delta\sigma_{r(R_p)} \frac{R_p^2}{h_0^2 - R_p^2} \left(1 + \frac{h_0^2}{r^2}\right) \quad (31)$$

$$\delta\varepsilon_{\theta(r)} = -\frac{1+\nu}{E_0} \delta\sigma_{r(R_p)} \frac{R_p^2}{h_0^2 - R_p^2} \left(1 - 2\nu + \frac{h_0^2}{r^2}\right) \quad (32)$$

$$\delta\varepsilon_{r(r)} = -\frac{1+\nu}{E_0} \delta\sigma_{r(R_p)} \frac{R_p^2}{h_0^2 - R_p^2} \left(1 - 2\nu - \frac{h_0^2}{r^2}\right) \quad (33)$$

Based on the above equations, the same expressions for the induced stresses and strains are obtained, for both cases (the horizontal and the vertical directions), for a deep tunnel, namely where $h_0 \gg R_p$. On the other hand, it is observed that the gravitational loads will not affect the displacements in the elastic zone directly.

In the above equations, $\delta\sigma_{r(R_p)}$ is the induced radial stress at the plastic radius, and is obtained from:

$$\delta\sigma_{r(R_p)} = \sigma_{r(R_p)} - \sigma_{r0(R_p)} \quad (34)$$

The final stresses ($\sigma_{r(r)}$, $\sigma_{\theta(r)}$), at any radius in the elastic zone, are obtained from the sum of the initial portions ($\sigma_{r0(r)}$, $\sigma_{\theta0(r)}$) and the induced portions ($\delta\sigma_{r(r)}$, $\delta\sigma_{\theta(r)}$).

$$\sigma_{r(r)} = \sigma_{r0(r)} + \delta\sigma_{r(r)} \quad (35)$$

$$\sigma_{\theta(r)} = \sigma_{\theta0(r)} + \delta\sigma_{\theta(r)} \quad (36)$$

The final radial and circumferential stresses at the plastic radius ($\sigma_{\theta(R_p)}$ and $\sigma_{r(R_p)}$) must satisfy the strength criterion; therefore, substituting these stresses into the Hoek-Brown strength criterion (i.e., Eq. (10)), and solving the equation obtained, gives the final boundary radial stress at the plastic radius $\sigma_{r(R_p)}$.

For the vertical direction:

$$\sigma_{r(R_p)} = \frac{1}{2} (m_i \sigma_c + 2\beta(1+\alpha)) - \left[m_i^2 \sigma_c^2 + 4m_i \beta \sigma_c (1+\alpha) + 4\alpha s_i \sigma_c^2 \left(2 + \alpha + \frac{1}{\alpha} \right) \right]^{\frac{1}{2}} \quad (37)$$

$$\alpha = \frac{R_p^2}{h_0^2 - R_p^2} \left(1 + \frac{h_0^2}{R_p^2} \right) \quad (38)$$

$$\beta = (1 + \alpha) \sigma_{0(R_p, \theta=90^\circ)} \quad (39)$$

And for the horizontal direction:

$$\sigma_{r(R_p)} = \frac{1}{2} \left(\lambda - \sqrt{\lambda^2 + 4\lambda\sigma_{0(\theta=0^\circ)} + s_i\sigma_c^2} \right) + \sigma_{0(\theta=0^\circ)} \quad (40)$$

$$\lambda = \frac{(m_i\sigma_c)}{4} \quad (41)$$

Where m_i and s_i are the failure parameters for the original rock mass.

It should be noted that the plastic zone around the circular opening is only formed when the internal support pressure p_i is lower than a critical value of $\sigma_{r(R_p=r_i)}$ (where $R_p = r_i$).

As mentioned, for deep tunnels, $h_0 \gg r_0$, the governing equations in the elastic zone for both the horizontal and vertical directions are identical. However, in this case, the weight of the plastic zone may be significant; and thus the gravitational loads must be taken into account.

6 COMPUTATION PROCEDURE

As illustrated in Appendix A, in the plastic zone, the finite-difference calculations are carried out in terms of the normalized radius $\rho = \frac{r}{R_p}$. First, the boundary stresses and strains at the plastic radius ($\rho_1=1$ or $r_1=R_p$) are calculated from the equations presented in Section 5. Then, the successive values of the stresses and strains in the plastic zone are computed from the equations presented in Appendix A. The computations of the stresses $\sigma_{r(j)}$ and $\sigma_{\theta(j)}$ and the strains $\varepsilon_{r(j)}$ and $\varepsilon_{\theta(j)}$ are carried out until the equilibrium conditions at the tunnel radius are satisfied. Thus, when the value of radial stress, for a specific ρ_n , satisfies equation $\sigma_{r(j)}=p_i$, the computations will be stopped. The new value of the plastic radius will then be obtained, by dividing the tunnel radius r_i by this final value of ρ_n .

When the value of the plastic radius R_p is not initially determined, the computations must be performed iteratively. Thus, the value of plastic radius R_p , obtained in each step, is used for computations of the subsequent step.

7 ILLUSTRATIVE EXAMPLES

The solution described in this paper has been programmed in the FORTRAN language for use with a computer. This program was used to analyze several typical tunnels, and the results were then interpreted.

EXAMPLE 1

In this example the same tunnel as in Brown et al. [1] and Sharan [2] was analyzed, and the results were then compared. In Brown et al.'s, and Sharan's closed-form solutions, an elastic brittle rock mass behavior model has been used. Brown et al. neglected the elastic strain distribution in the plastic zone, while Sharan utilized an approximate formula for the elastic strains. In the proposed method, the analyses were performed for two values of γ^{p*} , i.e., $\gamma^{p*} = 0$ (corresponding to a brittle behavior) and $\gamma^{p*} = 0.01$ (corresponding to a strain-softening behavior).

A typical deep tunnel, $h_0 \gg r_0$, with the following typical properties is considered:

$$m_i = 1.7, m_r = 1, s_i = 0.0039, s_r = 0, \sigma_c = 30 \text{ MPa},$$

$$\nu = 0.25, E_0 = E_r = 5500 \text{ Mpa}, \gamma = 0.028 \text{ MN/m}^3,$$

$$\sigma_0 = 30 \text{ MPa}, r_i = 5 \text{ m}, p_i = 5 \text{ MPa}, \psi_i = 30^\circ, \psi_r = 20^\circ$$

where E_0 and E_r are the elastic modulus for the original and residual rock masses, respectively, and ψ_i and ψ_r are the dilation angles for the original and residual rock masses, respectively.

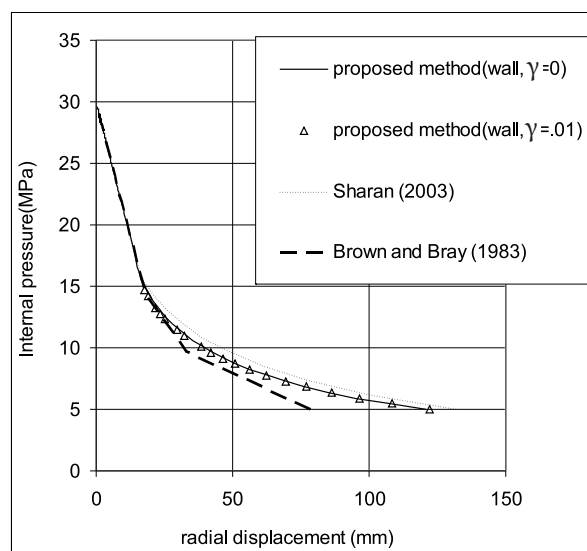


Figure 7. Ground-response curves for the tunnel of the example 1.

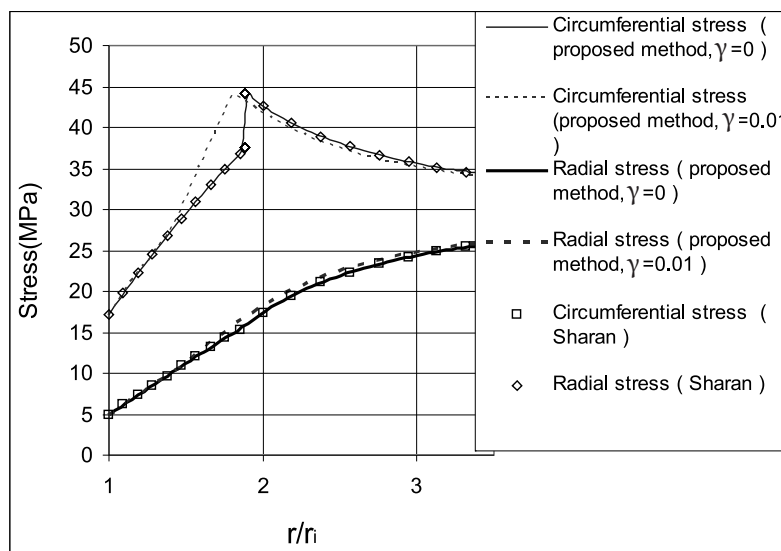


Figure 8. Distribution of stresses around the tunnel of example 1.

As this case is a deep tunnel, only the formulations for the horizontal direction are utilized.

Figs. 8 and 9 show the ground-response curves and the stress distributions obtained from the three theoretical methods. It is observed that Sharan's approximation overestimates the displacements, while Brown et al's approximation underestimates the displacements, as illustrated by Lee and Pietruszczak [6]. Furthermore, in the proposed method, the strain-softening behavior can

also be considered, and as shown in Figs. 8 and 9, for $\gamma^{p*} = 0.01$, the ground-response curves coincide, while the plastic radii are different.

EXAMPLE 2

In this example, the effect of gravitational loads being applied in the plastic zone is examined. In addition, the proposed method is compared with a numerical method.

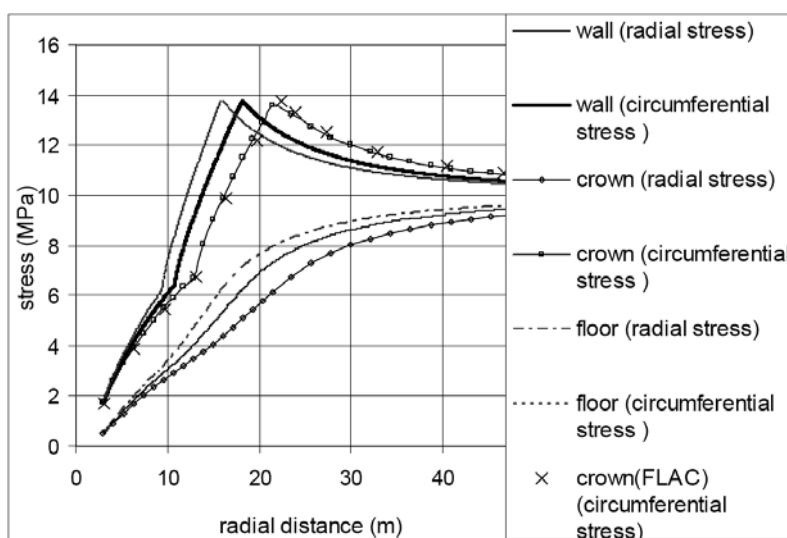


Figure 9. Distribution of stresses around the tunnel of example 2.

The following data set is used:

$$\begin{aligned} \gamma^{p*} &= 0.004, \quad m_i = 0.3, \quad m_r = 0.1, \quad s_i = 0.0001, \quad s_r = 0, \\ \sigma_c &= 30 \text{ MPa}, \quad \psi_i = \psi_r = 0, \quad \nu = 0.25, \quad E_0 = 10000 \text{ MPa}, \\ E_r &= 4000 \text{ MPa}, \quad \gamma = 0.028 \text{ MN/m}^3, \quad p_s = 0 \text{ MPa}, \\ \sigma_0 &= 10 \text{ MPa}, \quad r_i = 3 \text{ m}, \quad p_i = 0.5 \text{ MPa} \end{aligned}$$

This tunnel is also a deep tunnel; thus, for the analysis of the elastic zone the formulations proposed for the horizontal direction are utilized. However, because of the effect of gravitational loads in the plastic zone the results for the horizontal and vertical directions can be different.

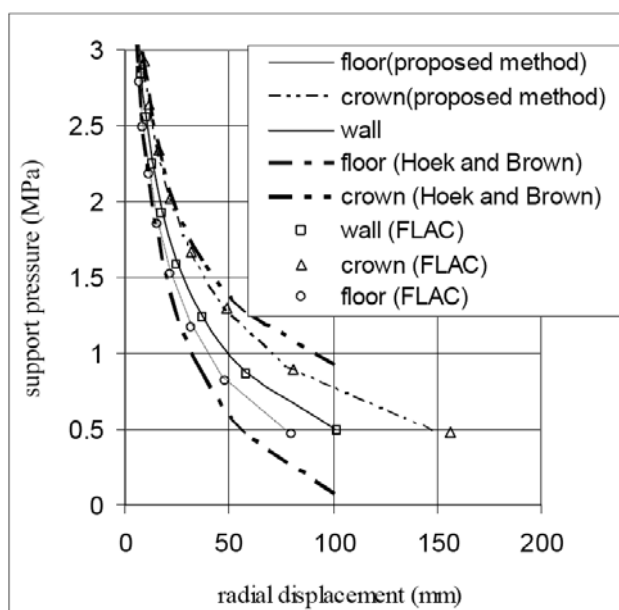


Figure 10. The ground-response curves for the tunnel of example 2.

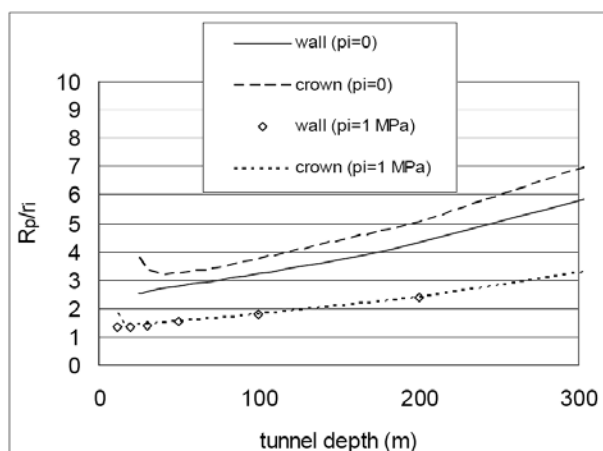


Figure 11. Variation of the plastic radius versus h_0 .

In Figs. 10 and 11 the ground-response curves and the stress distribution through the horizontal and vertical directions are depicted. In these figures, the results obtained from the FLAC 2D program [20] are also plotted, which show a very proper agreement with the proposed solution.

Fig. 9 shows that due to the weight of the plastic zone, the plastic radii are not the same for the different directions, and the plastic radius increases from the floor to the crown.

In Fig. 10, the ground-response curves obtained from Hoek and Brown's [19] simplified method are also plotted. As is clear from this figure, Hoek and Brown's method overestimates the tunnel convergence for the crown, and underestimates it for the floor.

EXAMPLE 3

In this example, the effect of tunnel depth and horizontal and vertical directions on the results are examined. For this purpose, the following data set is used:

$$\begin{aligned} \gamma^{p*} &= 0.0, \quad m_i = 0.7, \quad m_r = 0.3, \quad s_i = 0.001, \quad s_r = 0, \\ \sigma_c &= 30 \text{ MPa}, \quad \psi_i = \psi_r = 0, \quad \nu = 0.25, \quad E_0 = 1500 \text{ MPa}, \\ E_r &= 1500 \text{ MPa}, \quad \gamma = 0.028 \text{ MN/m}^3, \quad p_s = 5.0 \text{ MPa}, \\ r_i &= 5 \text{ m}, \quad p_i = 0.0 \text{ MPa and } 1.0 \text{ MPa} \end{aligned}$$

Fig. 11, shows the variations of the plastic radii for different values of the tunnel depth, for two cases of $p_i = 0.0 \text{ MPa}$ and 1.0 MPa . In the case of $p_i = 0.0 \text{ MPa}$, the plastic deformations in the plastic zone are large enough, and so the effect of gravitational loads is significant. Consequently, the plastic radii, through the horizontal and vertical directions, are not the same. On the other hand, in the case of $p_i = 1.0 \text{ MPa}$, the deformations in the plastic zone are small; thus, the plastic radii, through the horizontal and vertical directions, are approximately the same. It is concluded that the plastic radius for the tunnel crown is larger than the tunnel wall, and the difference increases with the increasing the depth of the tunnel.

The values of the radial displacements at the distance $r = h_0$ along the horizontal and vertical directions may be utilized as the lower-bound and the upper-bound values, respectively, for approximating the surface settlement. In Fig. 12 the radial displacements at the distance $r = h_0$ for different values of h_0 for two cases of $p_i = 0.0 \text{ MPa}$ and 1.0 MPa were plotted. It is clear that at small values of h_0 , because of the short distances between the ground surface and the plastic zone, excessive surface

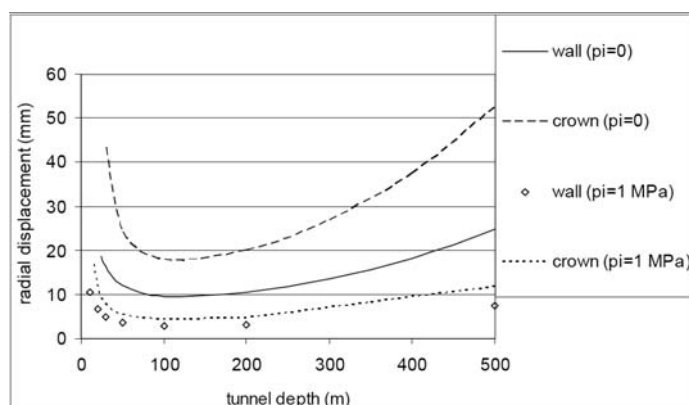


Figure 12. Variations of radial displacement at $r = h_0$ versus h_0 .

settlements occur. On the other hand, at large values of h_0 , the surface settlement may increase with depth due to an increase in magnitude of the in-situ stresses.

Furthermore, in Fig. 12, it is clear that the displacements through the tunnel crown are larger than the tunnel wall, and the difference becomes greater for the wider plastic zones.

8 CONCLUSIONS

In order to examine the C.-C. method, commonly used for the analysis of tunnels, and to demonstrate the effect of the classic assumptions on the characteristics of the ground-response curve, an analytical solution was proposed.

The solution is relatively simple, easy to use, and can readily indicate its sensitivity through a range of possible ground parameters, boundary conditions, and applied loads.

In this solution, the formulations were derived through horizontal and vertical directions, by taking the gravitational loads into account. It was shown that, for practical cases even for shallow tunnels, the convergence-confinement method is reasonably applicable. However, the effect of gravitational loads in the analyses can be noticeable, and ignoring the plastic load can lead to large errors in the calculations.

REFERENCES

- [1] Brown, E.T., Bray, J.W., Ladanyi, B., Hoek, E. (1983). Ground response curves for rock tunnels. *Journal of geotechnical Engineering*, Vol. 109, No. 1, pp. 15–39.
- [2] Sharan, S.K. (2003). Elastic–brittle–plastic analysis of circular openings in Hoek–Brown media. *Int. J. Rock Mech. Min. Sci.*, Vol. 40, No.6, pp. 817–824.
- [3] Carranza-Torres, C., Fairhurst, C. (1999). The elasto-plastic response of underground excavations in rock masses that satisfy the Hoek–Brown failure criterion. *Int. J. Rock Mech. Min. Sci.*, Vol. 36, No. 6, pp. 777–809.
- [4] Park, K.-H., Kim, Y.-J. (2006). Analytical solution for a circular opening in, an elasto-brittle-plastic rock. *Int. J. Rock Mech. Min. Sci.*, Vol. 43, pp. 616–622.
- [5] Guan, Z., Jiang, Y., Tanabasi, Y., (2007). Ground reaction analyses in conventional tunneling excavation. *Tunnelling and Underground Space Technology*, Vol. 22, No. 2, pp. 230–237.
- [6] Lee, Y.-K., Pietruszczak, S. (2008). A new numerical procedure for elasto-plastic analysis of a circular opening excavated in a strain-softening rock mass. *Tunnelling and Underground Space Technology*, Vol. 23, No. 5, pp. 588–599.
- [7] Fahimifar, A., Zareifard, M.R. (2009). A theoretical solution for analysis of tunnels below groundwater considering the hydraulic–mechanical coupling. *Tunnelling and Underground Space Technology*, Vol. 24, No. 6, pp. 634–646.
- [8] Carranza-Torres, C., Fairhurst, C. (2000). Application the convergence-confinement method of tunnel design to rock masses that satisfy the Hoek–Brown failure criterion. *Tunnelling and Underground Space Technology*, Vol. 16, No. 2, pp. 187–213.
- [9] González-Nicieza C., Álvarez-Vigil A.E., Menéndez-Díaz A., González-Palacio C. (2008). Influence of the depth and shape of a tunnel in the application the convergence-confinement method. *Tunnelling and Underground Space Technology*, Vol. 23, No. 1, pp. 25–37.

- [10] Lu A-Z., Xu G-s., Sun, F., Sun, W. (2010). Elastoplastic analysis of a circular tunnel including the effect of the axial in situ stress. *Int. J. Rock Mech. And Mining Sci.*, Vol. 47, No. 1, pp. 50–59.
- [11] Detournay, E. and Fairhurst, C. (1987). Two-dimensional elastoplastic analysis of along, cylindrical cavity under non-hydrostatic loading. *Int. J. Rock Mech. Min. Sci. & Geomech. Abstr.*, Vol. 24, No. 4, pp. 197–211.
- [12] Reed MB. (1988). The influence of out-of-plane stress on a plane strain problem in rock mechanics. *Int. J. Numer Anal Meth Geomech.*, Vol. 12, No., pp 173–81.
- [13] Hoek E., Brown E.T. (1980). Underground excavations in rock. The Institute of Mining and Metallurgy, London
- [14] Carranza-Torres, C. and Fairhurst, C. (1997). On the stability of tunnels under gravity loading, with post-peak softening of the ground. *Int. J. Rock Mech. Min. Sci.*, Vol. 34, No. 3-4, pp. 75.e1–75.e18.
- [15] Fahimifar, A., Zareifard, M.R., (2010). The elastoplastic response of circular tunnel considering gravity loads for two cases of plane strain and plane stress conditions. *Geotechnical Challenges in Megacities, Moscow*. V. 2.
- [16] Kolybas D. (2005). *Tunnelling and Tunnel Mechanics*. Springer-Verlag, Berlin Heidelberg (2)
- [17] Timoshenko S.P., and Goodier J.N. (1982). *Theory of Elasticity*. McGraw-Hill, New York
- [18] Alonso, E., Alejano, L.R., Varas, F., Fdez-Manin, G., Carranza-Torres, C. (2003). Ground response curves for rock masses exhibiting strain-softening behaviour. *Int. J. Numer. Anal. Meth. Geomech.*, Vol. 27, No. 13, pp. 1153– 1185.
- [19] Hoek E., Brown E.T. (1980). *Underground excavations in rock*. The Institute of Mining and Metallurgy, London
- [20] Itasca. (2000). *User manual for FLAC, Version 4.0*. Itasca Consulting Group Inc.: Minnesota

APPENDIX A. STRESS AND STRAIN ANALYSES FOR THE PLASTIC ZONE

stress analysis

The finite-difference method (FDM) is used to solve Eq. (17) for $\sigma_{r(j)}$ and $\sigma_{\theta(j)}$ by selecting an annular element of the outer radius ρ_{j-1} and the inner radius ρ_j shown in Fig. 6:

$$\sigma_{r(j)} = \sigma_{r(j-1)} + \lambda_1 - \left\{ \lambda_2 + \lambda_3 \sigma_{r(j-1)} \right\}^{\frac{1}{2}} \quad (\text{A1})$$

where:

$$\bar{m}_g = \frac{m_{g(j)} + m_{g(j)}}{2} \quad (\text{A2})$$

$$\bar{s}_g = \frac{s_{g(j)} + s_{g(j)}}{2} \quad (\text{A3})$$

$$\lambda_1 = F_r R_p (\rho_j - \rho_{j-1}) + 2\bar{m}_g \sigma_c \left(\frac{\rho_j - \rho_{j-1}}{\rho_j + \rho_{j-1}} \right)^2 \quad (\text{A4})$$

$$\lambda_2 = \left(\frac{\rho_j - \rho_{j-1}}{\rho_j + \rho_{j-1}} \right)^2 \left[\bar{m}_g^2 \sigma_c^2 \left(\frac{\rho_j - \rho_{j-1}}{\rho_j + \rho_{j-1}} \right)^2 + 2\bar{m}_g \sigma_c F_r R_p (\rho_j - \rho_{j-1}) + 4\bar{s}_g \sigma_c^2 \right] \quad (\text{A5})$$

$$\lambda_3 = 4\bar{m}_g \sigma_c \left(\frac{\rho_j - \rho_{j-1}}{\rho_j + \rho_{j-1}} \right)^2 \quad (\text{A6})$$

The failure criterion, i.e., Eq. (11), can then be used to calculate the corresponding values of $\sigma_{r(j)}$ as follows:

$$\sigma_{\theta(j)} = \sigma_{r(j)} + \left(m_{g(j)} \sigma_c \sigma_{r(j)} + s_{g(j)} \sigma_c^2 \right)^{\frac{1}{2}} \quad (\text{A7})$$

$\sigma_{r(j)}$ is a function of the plastic radius R_p for vertical direction, as observed in Eq. (A1); thus, the analyses are carried out alternately in a sequence of successive approximations, to achieve the appropriate convergence of the plastic radius R_p .

strain analysis

The total strain rates ε'_θ and ε'_r can be written in terms of the elastic ($\varepsilon'^e_\theta, \varepsilon'^e_r$) and plastic ($\varepsilon'^p_\theta, \varepsilon'^p_r$) components as:

$$\varepsilon'_r = \varepsilon'^e_r + \varepsilon'^p_r, \quad \varepsilon'_\theta = \varepsilon'^e_\theta + \varepsilon'^p_\theta \quad (\text{A8})$$

Considering the Mohr–Coulomb type of plastic potential function, i.e., Eq. (8), the elimination of the plastic multiplier $\dot{\lambda}$ from the flow rule, i.e., Eqs. (6) and (7), and using Eq. (15) gives the relation between the plastic parts of radial and circumferential strain rates:

$$\varepsilon'^p_r + K_\Psi \varepsilon'^p_\theta = 0 \quad (\text{A9})$$

The finite-difference method (FDM) is used to solve the governing differential equation obtained from Eqs (23) and (A9) for $\varepsilon'_{\theta(\rho_i)}$ and $\varepsilon'_{r(\rho_i)}$ by using the annular elements shown in Fig. 6 as:

$$\varepsilon'_{\theta(\rho_i)} = \frac{\left(2\bar{\Omega}_{(j)} - \varepsilon'_{\theta(j-1)}\left(3 + \bar{K}_{\Psi(j)}\right)\right)\rho_{(j-1)} + \varepsilon'_{\theta(j-1)}\rho_j\left(1 + \bar{K}_{\Psi(j)}\right) - 2\bar{\Omega}_{(j)}\rho_{(j)}}{\left(1 + \bar{K}_{\Psi(j)}\right)\rho_{(j-1)} - \left(3 + \bar{K}_{\Psi(j)}\right)\rho_{(j)}} \quad (\text{A10})$$

where:

$$\varepsilon_{r(j)}^e = \frac{\varepsilon_{r(j)}^e - \varepsilon_{r(j-1)}^e}{\rho_{(j)} - \rho_{(j-1)}} \quad (\text{A11})$$

$$\varepsilon_{\theta(\rho_i)}^e = \frac{\varepsilon_{\theta(j)}^e - \varepsilon_{\theta(j-1)}^e}{\rho_{(j)} - \rho_{(j-1)}} \quad (\text{A12})$$

$$\bar{K}_{\Psi(j)} = \frac{K_{\Psi(j)} + K_{\Psi(j-1)}}{2} \quad (\text{A13})$$

$$\Omega_{(j)} = \varepsilon_{r(j)}^e + K_{\Psi(j)}\varepsilon_{\theta(j)}^e \quad (\text{A14})$$

$$\bar{\Omega}_{(j)} = \frac{\Omega_{(j)} + \Omega_{(j-1)}}{2} \quad (\text{A15})$$

thus:

$$\varepsilon_{\theta(j)} = \varepsilon'_{\theta(j)}\left(\rho_{(j)} - \rho_{(j-1)}\right) + \varepsilon_{\theta(j-1)} \quad (\text{A16})$$

In addition, the corresponding values of the strains $\varepsilon_{r(j)}^e$, $\varepsilon_{\theta(j)}^e$, $\varepsilon_{r(j)}^p$, $\varepsilon_{\theta(j)}^p$, $\varepsilon_{r(j)}$ and $\varepsilon_{\theta(j)}$ are obtained using Eqs. (12), (13), (18), (A8), and (A9).

Using Eqs. (18) and (23), the following boundary conditions are obtained for the plastic radius, where, $\rho = \rho = 1$:

$$\varepsilon_{r(j=1)} = \varepsilon_{r(j=1)}^e \quad \text{and} \quad \varepsilon_{r(j=1)}^p = 0 \quad (\text{A17})$$

$$\varepsilon_{\theta(j=1)} = \varepsilon_{\theta(j=1)}^e \quad \text{and} \quad \varepsilon_{\theta(j=1)}^p = 0 \quad (\text{A18})$$

$$\varepsilon'_{\theta(j=1)} = \varepsilon_{r(j=1)} - \varepsilon_{\theta(j=1)} \quad (\text{A19})$$

NOMENCLATURE :

E_0 : Deformability modulus of elastic rock mass
 E_g : Deformability modulus of plastic rock mass
 h_0 : Depth of the tunnel
 F_r : Radial body force
 F_{θ} : Circumferential body force
 K : Lateral stress coefficient
 K_{Ψ} : Dilation factor
 $m_{i,s}$: Material constants for original rock mass.
 $m_{r,s}$: Material constants for residual rock mass
 $m_{g,s}$: Material constants for broken rock mass
 p_s : Surcharge load

r : Radial distance from the center of the tunnel
 r_i : Tunnel radius
 R_p : Radius of plastic zone
 u_r : Radial displacement
 (x,y,z) : Cartesian coordinates
 $\delta\sigma_{\theta}$: induced circumferential stress
 $\delta\sigma_r$: induced radial stress
 ε_1 : Major Principal strain of rock mass
 ε_3 : Minor principal strain of rock mass
 ε_{θ} : Circumferential strain
 ε_r : Radial strain
 ε_{θ}^e : Elastic circumferential strain
 ε_r^e : Elastic radial strain
 ε_{θ}^p : Plastic circumferential strain
 ε_r^p : Plastic radial strain
 $\dot{\varepsilon}$: Derivative of strain ε with respect to τ
 ε' : Derivative of strain ε with respect to ρ
 γ : Unit weight of rock mass
 γ^p : Deviatoric plastic strain
 γ^{p*} : Critical deviatoric plastic strain
 η : Softening parameter.
 $\dot{\lambda}$: Plastic multiplier
 ν_r : Poisson's ratio of rock mass
 θ : Angle measured clockwise from the horizontal direction
 ρ : Normalized radius
 σ_1 : Major principal stress
 σ_3 : Minor principal stress
 σ_c : Uniaxial compressive strength of intact rock
 σ_{θ} : Circumferential stress
 σ_r : Radial stress
 $\sigma_{\theta 0}$: Initial circumferential stress
 $\sigma_{r 0}$: Initial radial stress
 σ_0 : Initial stress
 τ : Fictitious time variable
 ψ_i : Dilation angle for original rock mass
 ψ_r : Dilation angle for residual rock mass
 ψ_g : Dilation angle for plastic rock mass
 Subscript e : Refers to elastic part
 Subscript p : Refers to plastic part

VERJETNOSTNA ŠTUDIJA POJAVA DROBLJENJA ZRN PO METODI WEIBULL

KHEFFACHE TOUFIK IN MELBOUCI BACHIR

o avtorjih

Kheffache Toufik
Université Abderahmane Mira de Bejaïa,
Route de Targua Ouzemour, 6000 Bejaïa, Alžirija

vodilni avtor

Melbouci Bachir
Université Mouloud Mammeri de Tizi Ouzou,
Environnement et Aménagement,
Laboratoire de Géomatériaux
BP N° 17 R.P., 15000 Tizi-Ouzou, Alžirija
e-pošta: bmelbouci@yahoo.fr

izvleček

Drobljenje zrn v pesek je pomemben postopek, ker povzroča fizikalne in mehanske spremembe materialov. Za določitev mehanskih sprememb je za porazdelitev zrn uporabljena statistična metoda, za določitev razvoja porazdelitve zrn (lomljenih in celih) v vzorcih pa mehanika loma.

Delo je rezultat eksperimentalne študije drobljenja posameznih zrn apnenca ter večzrnatih vzorcev, ki so bili podvrženi eno-osni obremenitvi, s čimer se je ugotovilo vpliv obremenitve in velikosti zrn na odnos lomljenja. S statistično metodo Weibull je problem modeliran in določen je odnos lomljenja za oba primera.

Izsledki študije so pokazali, da je ocena odklona odvisna od velikosti zrn in jakosti obremenitve. Statistično modeliranje po metodi Weibull pa je v obeh primerih dalo zadovoljive rezultate.

ključne besede

zrno, vzorec, drobljenje, statistična študija

PROBABILISTIC STUDY OF THE PHENOMENON OF CRUSHED GRAINS USING THE MODEL OF WEIBULL

KHEFFACHE TOUFIK and MELBOUCI BACHIR

about the authors

Kheffache Toufik
Université Abderahmane Mira de Bejaïa,
Route de Targua Ouzemour, 6000 Bejaïa, Algeria

corresponding author

Melbouci Bachir
Université Mouloud Mammeri de Tizi Ouzou,
Environnement et Aménagement,
Laboratoire de Géomatériaux
BP N° 17 R.P., 15000 Tizi-Ouzou, Algeria
E-mail: bmelbouci@yahoo.fr

abstract

The crushing of grains in a granular medium is a very important phenomenon; it is a source of both physical and mechanical changes to these materials. A statistical study of the mechanical properties of a material was used to characterize the distribution and fracture mechanics in order to quantify the evolution of these distributions with sample sizes (grains and whole grains).

This work presents the results of an experimental study made on the crushing of individual grains of limestone and samples consisting of multiple grains subjected to a uniaxial loading in order to highlight the influence of the loading and the grain size on the rate of crushing. A statistical study using the Weibull method allowed us to model the problem and quantify the rate of breakage for the two cases.

The results obtained show that the rate of deflection depends on the grain size and the intensity of the applied load. Statistical modelling using the Weibull method gave us acceptable results in both cases.

keywords

grain, sample, crushing, statistical study

INTRODUCTION

The effect of grain crushing is a specific problem for the behaviour of granular materials subjected to high stresses. The breaking or crushing of a grain is of great importance in understanding the deformation properties of soils or rocks. It has been observed that the effect of the crushing of particles is advanced as a major cause of the compressibility and the deterioration of the mechanical properties of granular materials subjected to high stresses [1].

Studies, usually based on comparisons of grain size distribution curves before and after loading, performed on grain samples showed that the phenomenon of crushing the grains depends on the physical and mechanical characteristics of the grains. The authors of [2,3,4] studied the influence of grain size, shape and size distribution. Their findings, in agreement with all the results available on the mechanical behaviour of granular media under high stresses, suggest that the effect of grain crushing and the compressibility of the medium increases with increasing grain size, the uniformity of the sample, the angularity of the particles, the pressure containment, and the deviator stress for a given confining pressure.

Based on these experiments, parameters such as the total deal-breaker factor [5], the granular stability (aggregate stability) [6], the probability of a crash and the breaker particle factor [7] were identified. These parameters were found to be of great importance for an understanding of the behaviour of granular materials crushing. It has been shown that the stresses of the resistance to the crushing of particles follow the Weibull distribution [8,9]. For soil particles of size " d ", loaded diametrically between two flat plates, McDowell and Amon [8] showed that the survival probability $P_s(d)$ is given according to the reference diameter d_0 , the stress σ_0 that gives a probability of survival of 37% for the particle diameter d_0 tested, and " m ", which is the Weibull modulus.

This work focuses on determining the probability of the survival of grains made of limestone subjected to unidirectional loading using the Weibull statistical method. It

consists of submitting a singular grain to a unidirectional loading and then samples of multiple grains until break up. Laboratory tests provide the pairs $(\sigma; P_s(d))$ that allow us to determine the Weibull modulus for each case separately. The results obtained show that the probability of survival, either of the crash of a singular grain or in the case of samples formed by multiple grains, can be represented by the Weibull statistical distribution.

1 IDENTIFICATION AND CHARACTERIZATION OF MATERIALS

The materials used are aggregates obtained from crushing rock coming from Adrar Oufarnou career. The deposit of rock in question is located at a distance of 8 km north of the city of Bejaia in Algeria. The deposit is formed by lands of lower leas, which are represented by grey limestone, a light-grey, pinkish compact and massive to small and fat crystals dolomitized by locals for the production of aggregates and stones used in construction. All the seated limestone is traversed by folions. The massif is formed at its base by marls, marly limestone and the dogger by massive limestone and dolomite from the lower leas to the top.

The analysis performed by the specialized laboratory of the National Office of Geological and Mining Research (ORGM) on rock samples in order to identify the mineralogical and chemical characteristics of the deposit produced the results in Table 1.

Table 1. Chemical constituents of the material.

Component	Chemical symbols	Percentage
silicon oxide	SiO ₂	~1.75%
iron oxide	FeO ₃	~0.2%
titanium oxide	TiO ₂	<0.5%
Aluminum oxide	Al ₂ O ₂	~0.05%
manganese oxide	MnO	~0.05%
magnesium oxide	MgO	0.62%
sodium oxide	Na ₂ O	<0.5%
potassium oxide	K ₂ O	<0.5%
Sulfuric oxide	SO ₃	<0.5%
lime	(CaO)	54%
fire losses PAF (organic materials and other)	-	43%

The tests results carried out with the Los Angeles (LA) and Micro-Deval (MDE) on the material gave mean values of LA (%) = 31 and of MDE (%) = 19. Tests of the fragmentability according to the EN standard (NF P94-066) and the degradability DG (NF P94-067) made into a 10/20mm fraction of this material were Fr = 3 and DG = 1. The average absolute density is approximately 2.7g/cm³.

2 DESCRIPTION OF THE EXPERIMENTAL DEVICE

The experimental device shown in Figure (1) is designed specifically for a study of the characteristics of the crushing of granular materials that come from crushing limestone.



Figure 1. Presentation of the samples used.

Actually, this material is used to adapt a brain hydraulics used to apply loads on the device, which is used in turn to hold the samples. Overall, we used three types of fixtures for the various tests.

The first assembly consists of two hard steel plates. The thickness of each is 6 mm; they are used to apply stress to the grains. These will be placed between two plates and subjected to a normal load for the crushing grain by grain. And for the second installation it is a hard steel cylinder of 5.5 mm in diameter, with a height that respects the ratio H/d between 3 and 5, and steel piston lasts of 5.3 mm in diameter, used to transmit loads to the sample. This arrangement is used for crushing tests of the samples of grain classes 3.5mm, 5mm and 6.3-8mm. The third device is a second identical assembly with different dimensions used to crush grain samples of classes 8-10 mm and 14mm. The diameter of the cylinder is 10.5mm and the piston is 10.3 mm, able to maintain the ratio H/d at between 3 and 5.

The grains used in the tests will be coated with a colour pigment on the surface for the easy identification of possible breaks after the application of a load on different samples. This coloration is such that it has no effect on the surface of the grains.

The load is applied with hydraulic system equipment that allows automatic control of the load applied to the sample of the material in question and facilitates the reading values of the applied force.

3 CRUSH BY GRAIN

In this case grains of limestone were used more or less rounded to the different size classes after they were coated with a colour pigment on the surface. Note that the choice of a standard sample to be tested in the laboratory is necessary if the size effects are considered solely responsible for the variations in the mechanical properties in order to avoid effects related to the shape.

The tensile strength of the soil particles and the rock is usually measured by the diametral compression between plates until fracture [10].

The crushing test consists of subjecting the individual grains to a normal force. The grain is placed between two steel plates and using the hydraulic cylinder a load is exerted. For a particle of diameter d , diametrically compressed by a force F , a tensile strength σ feature is induced that can be defined as follows:

$$\sigma = \frac{F}{d^2} \quad (1)$$

The dimension d is usually the distance between two plates, but for particles that are roughly spherical the nominal size can be taken as the average of three measurements along the orthogonal directions [9].

The tensile strength corresponds to the maximum value of σ at which the particle undergoes catastrophic failure [9].

For each size class we conducted 40 tests, such that each test effort is exerted on the grain in question until rupture. The tensile strength is taken as the point at which the grain undergoes a catastrophic failure. The results for the five classes tested are represented in Figure (3).



Figure 2. Tests crushing grain by grain.

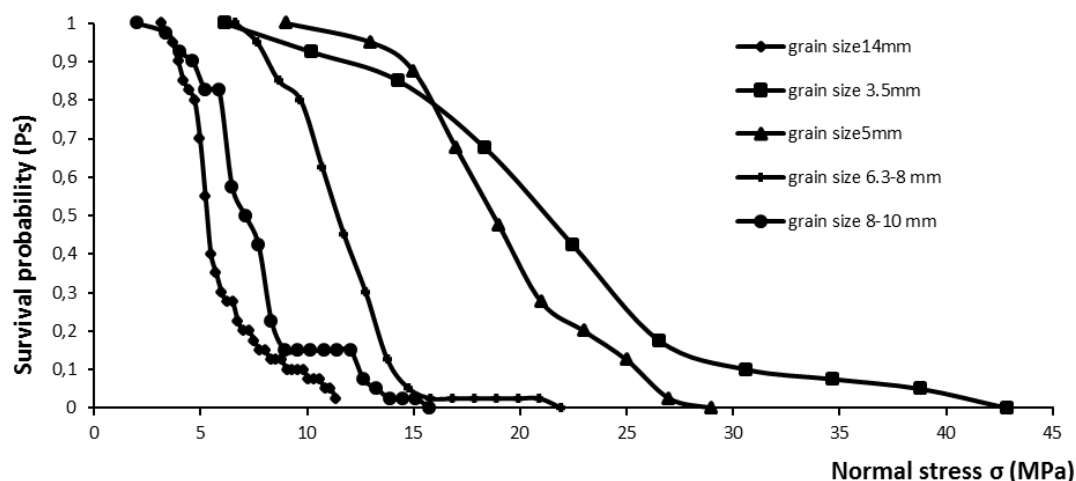


Figure 3. Representation of the percentage survival of grains of limestone according to the load exerted on the crushed limestone grains (singular grain).

4 RESULTS AND DISCUSSION

After submitting a grain to a normal force, it was noted that for all grains, the first cracks appear on the angularities in contact with the steel plates. The fracture occurs in the form of a shell for some grains and finally the total failure and catastrophic fracture occurs.

Figure (3) shows the representation of the percentage survival of particles as a function of the applied stress. The relative frequency is calculated using the median value. The results obtained show a dispersion of the values of the compressive strength for the same size class and that for different classes studied. These results are similar to those obtained for cereal grains and sand silica gel reported by [10], and the ballast carried out by [11]. The variation of the resistance to the crushing of the grains can be explained by the fact that the state of the grains (shape) is not the same before their submission to the loading, so that the state of the cracking varies from one grain to another, which is reflected by the change in the resistance, and thus spreading curves $P_s = f(\sigma)$. These generally have the same form for different classes.

The calculation of the probability of survival for the grains was carried out using the following formula:

$$P_s = 1 - P_c \quad (2)$$

- P_c : cumulative percentage of broken grains;
- P_s : percentage of grains that survive;

The minimum resistance of the crash or of the appearance of the first break differs from one class to the other; its value increases with the decrease in the grain diameters, d , such that the minimum resistances obtained are shown in Table 2:

Table 2. Minimum stress of rupture by size range.

Diameter of particle size d (mm)	3.5	5	6.3-8	8-10	14
minimum stress (MPa)	6.12	9	5.6	3.4	1.4

The compressive strength presents a scale effect: the larger the sample size, the lower is the resistance [10]. Granular materials from original rocks are generally porous with a low tenacity (full of cracks and pores). When two geometrically identical blocks are cut from a single block of fragile rock, they have a dispersion of strength due to the dispersion of the size of the existing defects. When the grains of soil are healthy, small and very rounded, they can withstand very high stresses [12]. This has been explained by several authors with the fact that the probability of the existence of defects in a big grain is more than for a small one. When the soil grains are hard, strong and very rounded, they can withstand high stresses without being crushed. The angular particles of freshly extracted materials undergo fragmentation under the normal pressures due to the rupture of sharp angularities.

5 STATISTICAL MODELLING

In order to understand the physical behaviour of soils, it is important to define the degree of crushing of the grains of a soil element and then to quantify it, because the crushing of grain soils during loading is a source of modification of the physical and mechanical characteristics [1]. In order to quantify the grain-crushing phenomenon we made a representation of the results of crash tests for singular grains with the graphs $P_s = f(\sigma)$ is shown.

To achieve a model that supports the quantization rate of crushing grains, we used the Weibull statistical method. This method takes into account the dispersion of the responses measured during the tests. The perspective used in the model is that the rupture is initiated at a defect of the material that spreads instantaneously to produce the break. This is taken as being fragile. The heterogeneity of the material is modelled by defects that are characterized by their sensitivity to rupture under a mechanical stress.

In the spirit of the Weibull statistical method for any constraint σ of the pair $(\sigma; P_s(d))$ we calculate $x_i = \ln(\sigma_i)$ and $P_s = 1 - P_c$ and $y_i = \ln(-\ln(P_s(\sigma_i)))$. The graphical representation of the cloud point Fig (3) shows linearity, so that the points obtained are sufficiently aligned and can be presented by the regression lines of y in x .

The regression equation obtained was:

$$Y = m \cdot x - m \cdot \ln(\sigma_0) \quad (3)$$

The regression lines obtained give us the values of the Weibull parameters m for each class studied, such that the latter is the slope of the line and $(-m \cdot \ln(\sigma_0))$ is the intercept. The Weibull modulus m is a measure of the dispersion; the lower the modulus, the higher is the dispersion.

Weibull proposed a simplified form for calculating the probability of failure:

$$P_C(\sigma, V) = 1 - e^{-\left(\frac{V}{V_0}\right)^m f(\sigma)} \quad (4)$$

where V is the sample volume, V_0 is the reference volume and σ is the tensile strength. McDowell and Humphreys [10] studied the crushing of singular-grain serials (corn flask, corn Cripps and sand silica gel) and concluded that the failure of the latter can be quantified using the Weibull statistical method. They proposed the following formula:

$$P_s(d) = e^{-\left(\frac{d}{d_0}\right)^3 \left(\frac{\sigma}{\sigma_0}\right)^m} \quad (5)$$

where σ_0 corresponds to the stress for a survival of 37% for a particle diameter d_0 of the reference. The value thereof is approximately equal to the average stress, and m is the Weibull modulus, which decreases with the growth of the variability stresses.

McDowell and Bolton [13] have suggested that the tensile strength should be proportional to the average stress of crushing the grain. McDowell and Humphrys [10] showed that the value of the crush strength is measured according to the size, so that the average resistance is given by:

$$\sigma_{av} = d^{-b} \quad (6)$$

where b is a parameter determined experimentally to be equal to $3/m$.

McDowell and Humphrys [10] proposed that for the singular grain crash for a number of materials equation (5) can be written as follows:

$$P_s(d) = e^{-\left[\left(\frac{\sigma}{\sigma_0}\right)^m\right]} \quad (7)$$

Wee Lim et al. [11] showed that σ_0 is proportional to the grain diameter and approximately equal to the average resistance with $\sigma_{av} = d^{-3/m}$

In the case of identical grains of limestone, it was considered that $d/d_0 = 1$, and then equation (5) can be reduced to the following formula:

$$P_s(d) = e^{-\left[\left(\frac{\sigma}{\sigma_{50}}\right)^m\right]} \quad (8)$$

The results for all the cases studied show that we can take $\sigma_0 \approx \sigma_{50}$.

So in this case, the survival rate of the grain can be approximated by the empirical formula shown in (8).

The linearization curves $P_s = f(\sigma)$ using the Weibull method Fig. (4) for the limestone grains show a linear tendency, and the Weibull modulus that corresponds to the slope of the regression line varies according to the sample size, such that the values obtained for each class are represented in Table 3:

Table 3. Weibull modulus obtained for each size class studied.

Diameter of particle size d (mm)	3.5	5	6.3-8	8-10	14
Weibull modulus obtained " m "	2.969	5.66	4.28	3.17	2.37

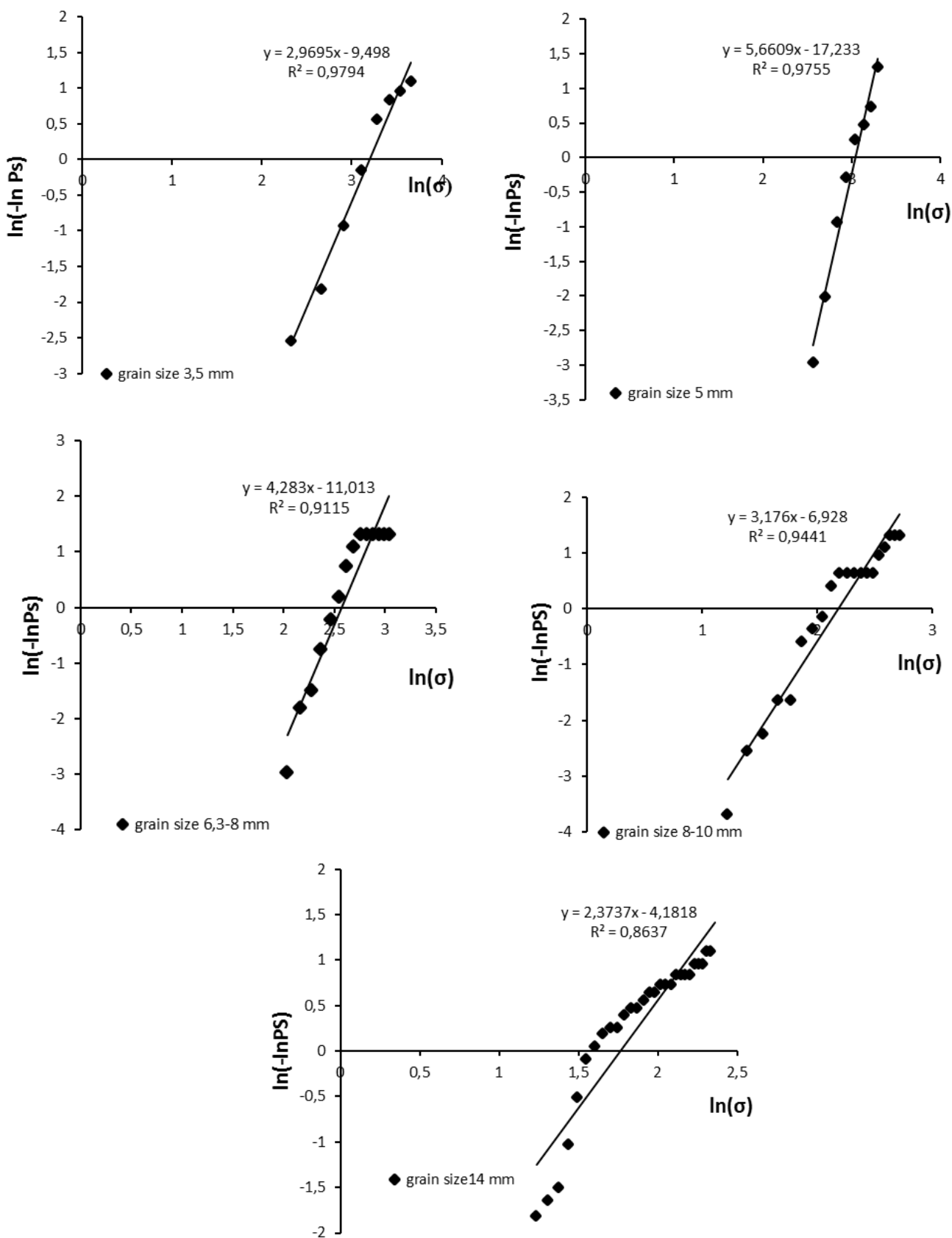


Figure 4. Graphical representation of the survival Weibull probability (crushing grain by grain).

Note that the Weibull modulus increases with a reduction of the grain size for the four classes studied. This means that higher when the grain size is important, the greater dispersion of values of resistance is important. In fact the Weibull modulus decreases with an increasing of the distribution of the values of the stress σ [8, 11]. The results confirm that the Weibull modulus cannot be a parameter belonging to the materials, but depends on the grain size and the initial state of the material. It is possible that the shape parameter is overestimated because it is biased, but in this study it is not taken in consideration that this parameter is overestimated and should be corrected.

5.1 CRUSHING OF A SAMPLE CONSISTING OF SEVERAL GRAINS

In this case we pass from a study of a singular grain to a study of one of medium to several grains in order to calculate the probability of the rupture of the grains in a granular medium and their quantification.

Several studies have been conducted in the direction of quantifying the rate of crushing of the grains. Usually, these studies are based on a comparison of the grain size distribution curves of samples of materials before and after their submission to the load. Several authors have defined the rate of deflection from developing or spreading the grading curve [14, 15, 16]. Then, all the parameters are determined from the percentage corresponding to a given selected grain size. We distinguish the methods of a single factor, on the one hand [2, 17], and on the other hand the methods with several other factors, for example, the Marsal method that allows determining the percentage of grains weight affected during the test. In our case we conducted another way, as we took for each

size class a known number of grains, according to the diameters, the number of grains taken for each sample is as follows: (25 grains of the class for 14mm, 30 grains for class 8-10, and 6.3-8, 100 for class 5 mm and 200 grains for Class 3.5mm). The number of grains was chosen to meet the ratio H/d between 3 and 5. And then we calculate the number of grain that has apparent breaks.

Granular systems are disordered and heterogeneous systems formed by many interacting elements; they have two complementary phases, a poly-disperse distribution of sizes, varied forms of particles, interactions that are highly nonlinear and an intrinsically disordered geometry [18]. For these reasons, we must use a standard sample in the laboratory for the effects of size to be considered solely responsible for the variations in the mechanical properties.

5.2 OBSERVATIONS ON SAMPLES

The observations made on all samples submitted to unidirectional loading showed that the contacts between the grains are the cause of most breaks noticed in most grains. When two bodies in contact are pressed against each other, they deform locally to create a contact area of a characteristic dimension smaller than the small radius of curvature of two bodies at the contact point, the area on which the contact force acts. The induced stresses are thus concentrated in a small region around the contact point that leads to breakage, in most cases it is the sharp points that break, and their intensity decreases rapidly when it is removed (after the break). In the aggregate, there are two types of changes possible under mechanical stress: they break giving elements of any size or they wear by friction giving essentially fine elements [12].



Figure 5. Crushing tests of samples composed of multiple grains.

The phenomenon of grain crushing occurs at much higher values in the case of crushing grain by grain. This can be explained in terms of the rearrangement of the grains of the samples. This leads us to say that the grains begin to crash when they have a tight configuration and activation of the contact forces between the grains. So in this case, the force applied on the set (sample) has not yet reached the inherent resistance of the grains. The crushing of the grains appears when the constraint imposed on the grains is beyond their own strength [12]. We can also add that when a grain in a granular medium is surrounded by other grains and can generate forces of containment on the latter, it will prevent or at least delay the break.

6 EXPERIMENTAL RESULTS

The test results of unidirectional loading on the samples consisting of several grains of the material Fig. (6) show a distribution similar to the grain-by-grain crushing (grain singular), but with much higher stress values. During the loading tests we can distinguish three phases, the first one happens without apparent breaks, this is the phase of the rearrangement of the grain. In this case the load applied is dissipated to create closer contacts of the grains against each other, and this is reflected in most cases by a slight change in volume. Above a certain load we obtain a significant rate of grain crushing. This is the second phase. The last one is the phase or structure in

which the sample has a new configuration (new size). New contacts and a new charge distribution reduce the rate of deflection. Hagerty et al [19] observed the same phases.

The choice of grains of the same shape (rounded) and the same size constitutes samples that are more or less of uniform size for different classes of limestone aggregates used in the tests. It was found that the crushing of the grains does not change after obtaining a certain rate. This is probably due to the new configuration size of the samples, so that smaller particles generated by the crushing of the larger ones will rearrange to fill the inter-granular voids. This will lead to the creation of other points of contact, and a new redistribution of stresses within the sample. A particle of a given size suffers less in the case of breakage, because it will fragment into smaller particles that will create a new scale of the sample and therefore new contacts. In the case of graduated soil there are many particles so many contacts and inter-particle charge in the contact is less than in a soil with uniform graduation [14, 20].

The observation of the samples after their submission to the various loads has shown that most cracks are located at the angularities. This can be explained by the fact that particles with angularities break more easily, as long as the loads are concentrated along the latter, causing fracturing of the particles. The stress can also focus on the corner points of contact, causing breakage points [17].

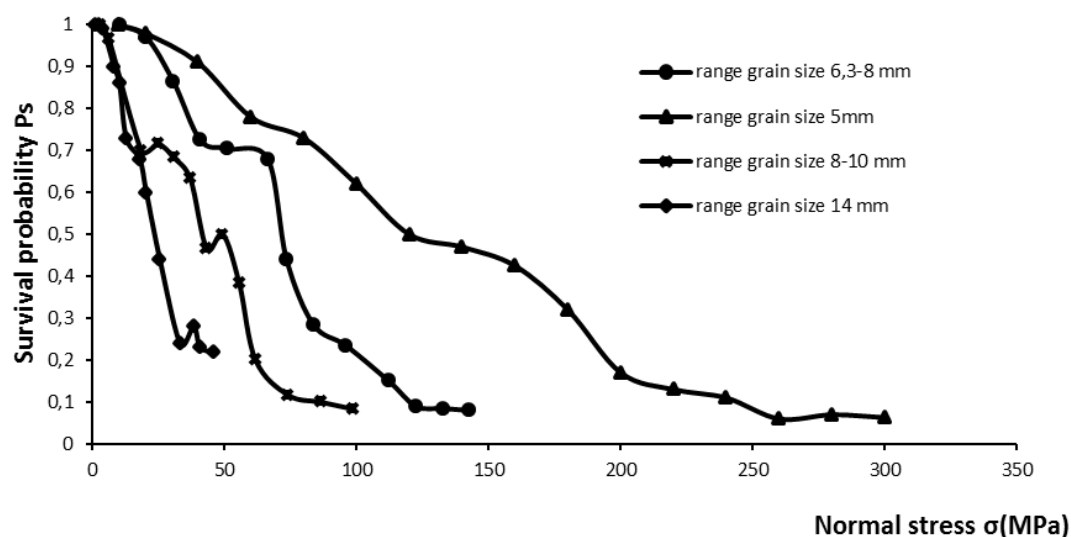


Figure 6. Representation of the survival percentage of limestone grains according to the load exerted on the crushed grains (samples consisting of several grains).

7 STATISTICAL MODELLING

Statistical modelling aims to quantify the rate of crushing of grains in samples subjected to a load. For this we plotted the curves $P_s = f(\sigma)$ corresponding to each size class. The results of the statistical study gave the values σ and P_s from Eq. (2).

In the same way, for any constraint σ we calculate $x_i = \ln(\sigma_i)$ and $P_s = 1 - P_c$ and $y_i = \ln(-\ln(P_s(\sigma_i)))$ in the spirit of the Weibull statistical method. The graphical representation of the cloud point Fig (7) shows linearity, so that the points obtained are sufficiently aligned and can be represented by the regression lines of $y=f(x)$.

Fig. 7 shows the linearization of the curves in Fig. 6 using the Weibull method, obtained for samples composed of multiple grains. This linearization is obtained by calculating $\ln(\sigma)$ and $\ln(-\ln(P_s))$, respectively, which correspond to the natural logarithm of the stress and the survival probability of the particles to obtain the Weibull modulus m .

The results obtained confirm that the Weibull method are applicable for modelling the phenomenon of crushing the grains in a granular medium.

Because of the uniformity of the samples used for various tests, we can consider reports $V/V_0 = 1$, where V

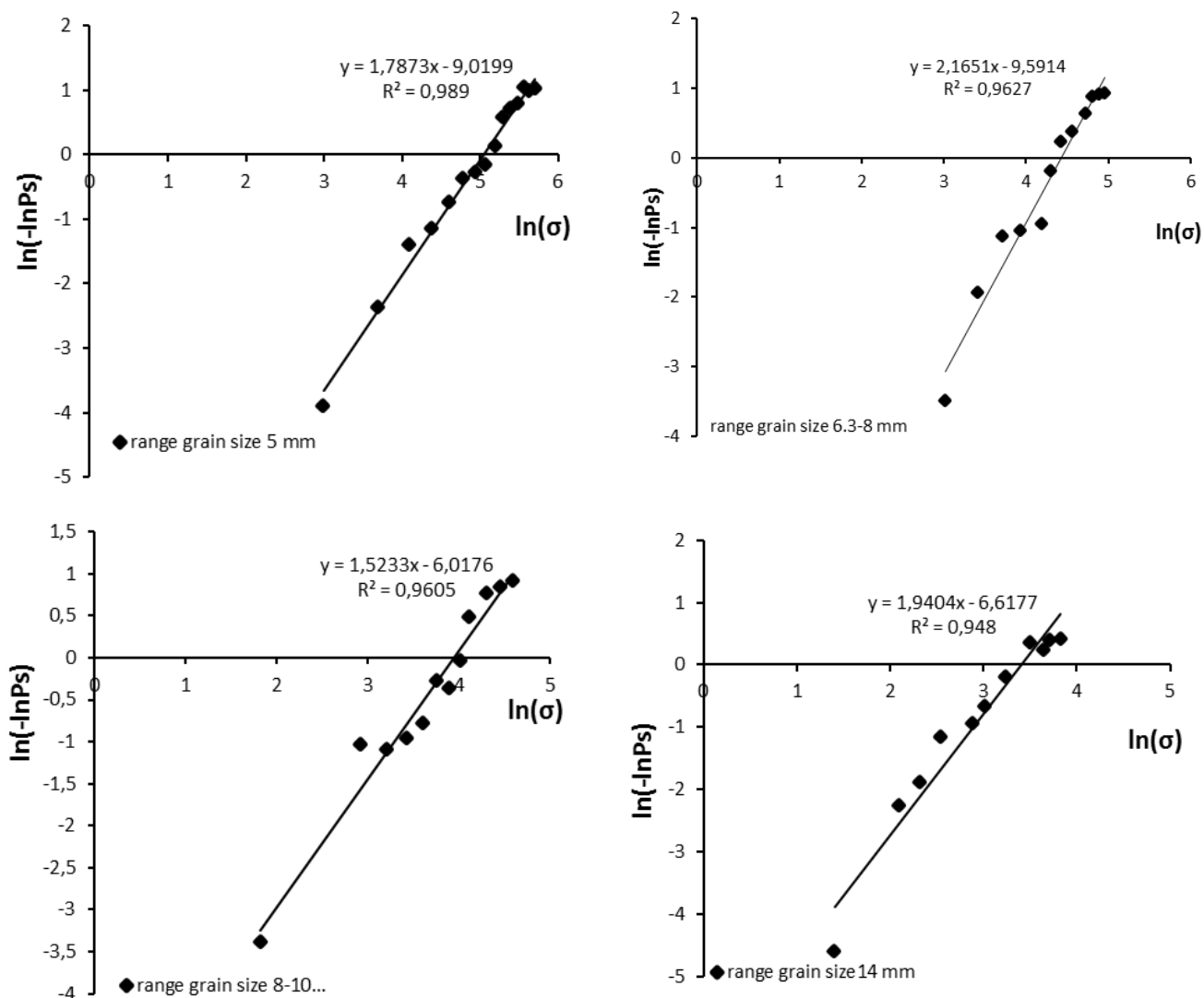


Figure 7. Representation of the survival Weibull probability (sample consisting of several grains).

and V_0 are respectively the volumes of the sample tested and the volume of the reference sample. The Weibull modulus for each class is obtained from the slopes of the regression lines, and σ_0 in our case is taken as the stress at which about 50% of the particles survive. In this case the probability of the survival of the grains can be calculated using equation (7).

To verify the validity of the model we can perform the Kolmogorov-Smirnov test on all the classes studied. In this test, the calculations about the laws of probability are on distribution functions: measuring the difference between the theoretical distribution function and the distribution function observed. In this study, instead of conduct tests, it was limited to the presentation of the comparison of the experimental values with those obtained by the theoretical formula. The results showed that the differences are not significant.

The comparison of results obtained in the laboratory with those calculated by the formula (7) for each class (fig. 8) shows that they have the same appearance as those obtained from the experiment with a slight lag. This means that the formula obtained with the following reasoning may represent the quantity of grain crushed under a known load. We can therefore say that the Weibull method can be generalized to estimate the probability of crushing the grains in a medium composed of multiple grains.

CONCLUSION

The diametral compression tests conducted on five classes of different size, d , of limestone grain for the crash of singular grains showed the sensitivity of grain crushing. It was noted that the rate of deflection

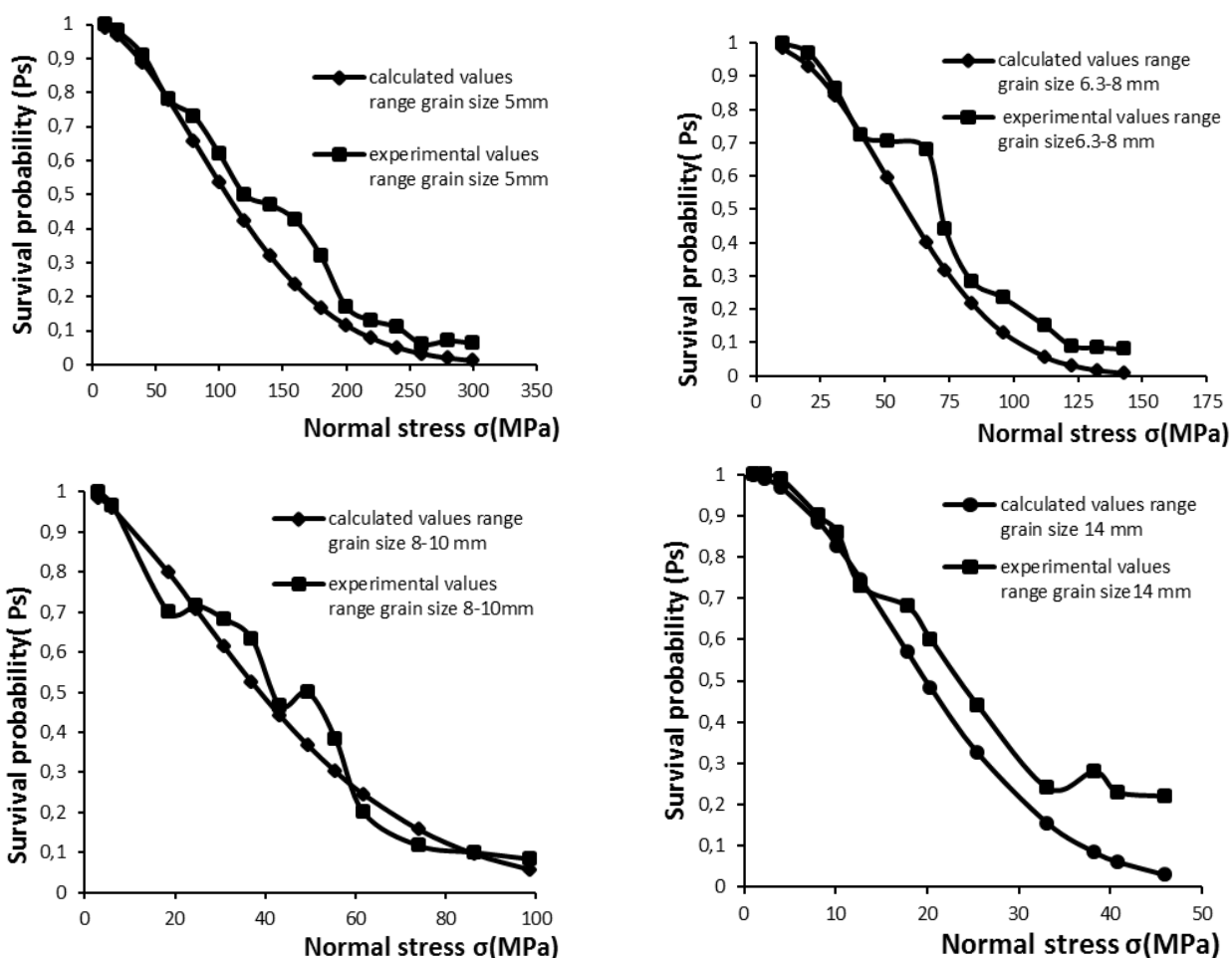


Figure 8. Comparison of experimental results with those calculated for the crash of samples consisting of several grains of limestone.

increases with the increase in the grain size and the applied load. In general, the first grain crash took place at the angularities. These superficial cracks are caused by contacts between the grains and the press platens for the crash grain by grain. After a certain threshold load, brutal destruction of the grain may occur. The representation of the percentage survival of particles as a function of applied stress showed dispersion values of the compressive strength for the same class size for different classes studied. The minimum resistance of the crash or of the appearance of the first fracture differs from one class to another increase with an decreasing diameter, d , of the grain. For each class under test, the stress distribution of the crash follows the Weibull distribution.

The uniaxial loading tests performed on samples consisting of several grains of the same limestone have shown that the rate of deflection also depends in this case on the diameter of the grain and the applied load, in the same way as in the case of crushing of singular grains. The stresses of the first breaks are higher compared to the minimum stress fracture of one element of the same diameter. This can be explained by the grain rearrangement of the samples. This leads us to say that the grains begin to crash when they have a tight configuration and by the activation of contact forces between the grains. The representation of the probability of survival according to the applied stress on the sample also shows a dispersion of resistance values for samples of the same class. The Weibull statistical method gave satisfactory results on the statistical modelling of the crushing phenomenon. So we conclude that the probability of survival of the grains in a granular medium follows the Weibull distribution.

REFERENCES

- [1] Colliat-Dangus, J.L. (1986). Comportement des matériaux granulaires sous fortes contraintes influence de la nature minéralogique du matériau étudié. *Thèse de l'Université Scientifique et Médicale de l'Institut Polytechnique de Grenoble*, France.
- [2] Lee, K.L. and Farhoomand, J. (1967). Compressibility and crushing of granular soils in anisotropic triaxial compression. *Canadian Geotechnical J.*, Vol. 4, No. 1, pp. 68-86.
- [3] Guyon, E. et Troadec, J. P. (1994). Du sac de billes au tas de sable, *Editions. Odile Jacob*, Paris.
- [4] Ramamurthy, T. (1969). Crushing phenomena in granular soils. *J Ind Natl Soc Soil Mech Found Eng* 8:67-86.
- [5] Hardin, B. O. (1985). Crushing of soil particles. *J Geotech Eng. Proc. ASCE* 111, N°10, 1177-1192.
- [6] Prasad, P. Bartake. Devendra, N. Singh. (2007). A generalized methodology for determination of crushing strength of granular materials. *Geotech Geol Eng* 25: 203-213
- [7] Nakata, Y. Hyde, AFL. Hyodo, M. Murata, H. (1999). A probabilistic approach to sand particle crushing in the triaxial test. *Geotechnique* 49(5): 567-583.
- [8] McDowell, G. R. and Amon, A. (2000). The Application of Weibull Statistics to the Fracture of Soil Particles. *Soils and foundations*. Tokyo, 40(5), 133-142.
- [9] McDowell, G. R., (2002). On the Yielding and Plastic Compression of Sand. *Soils and foundations -TOKYO-*, 42(1), 139-146.
- [10] McDowell, G.R. and Humphreys, A. (2002). Yielding of granular materials. *Granular Matter* 4, No.1, 1-8. 26.
- [11] Wee, L. Lim, McDowell, Glenn R., Andrew C. Collop (2004). The application of Weibull statistics to the strength of railway ballast. *Granular Matter* 6, 229-237 Springer-Verlag. DOI 10.1007/s10035-004-0180-z.
- [12] Melbouci, B. Bahar, R. Cambou, B (2008), Study of the behaviour of schist grains under crushing. *Bull Eng Geol Environ* 67:209-218.
- [13] McDowell, G.R., Bolton, M.D. (1998), On the micromechanics of crushable aggregates. *Geotechnique* 48(5):667-6790.
- [14] Erzin, Y., Yilmaz, I. (2008). A case study of crushing resistance of Anatolian sands at lower and higher density. *Bull Eng Geol Environ* 67:71-77.
- [15] Akers, S. A. (2001). Two-Dimensional Finite Element Analysis of Porous Geomaterials at Multikilobar Stress Levels. *Faculty of the Virginia Polytechnic Institute and State University*. USA.
- [16] Al Dwairi, R, Al-Hattamleh, O., Al-Shalabi, F., and Al-Rousan, T. (2009). Effect of Grain Crushing and Bedding Plane Inclination on Ras en-Naqab Natural Sand Behavior. *EJGE*, Vol. 14, Pp 1-22, Bund. L.
- [17] Lade, P.V, Yamamuro, J.A, Bopp PA (1996). Significance of particle crushing in granular materials. *J Geotech Eng* 122(4):309-316.
- [18] Azema, É. (2007). Étude numérique des matériaux granulaires à grains polyédriques: rhéologie quasi-statique, dynamique vibratoire, application au procédé de bourrage du ballast. *Thèse de Doctorat*, Université Montpellier, France.
- [19] Hagerty, M., M.; Hite, D.R.; Ullrich, C.R. et Hagerty D.J. (1993). One dimensional high pressure compression of granular media. *Journal of Geotechnical Engineering*, 119, (1): 1-17.
- [20] Chavez, C. and Alonso, E.E (2003). A constitutive model for crushed granular aggregates which includes section effect. *Soils and foundation*, Vol.43, N°4, 215-227. Japznes Geotechnical Society.

ZEOLITIZACIJA ELEKTROFILTRskega PEPELA PRI ODSTRANJEVANJU PO MOKREM IN SUHEM POSTOPKU

BHAGWANJEE JHA IN D. N. SINGH

o avtorjih

Bhagwanjee Jha
Indian Institute of Technology Bombay,
Department of Civil Engineering
Powai, Mumbai-400076, Indija
e-pošta: jha66b@iitb.ac.in

vodilni avtor

D. N. Singh
Indian Institute of Technology Bombay,
Department of Civil Engineering
Powai, Mumbai-400076, Indija
e-pošta: dns@civil.iitb.ac.in

izvleček

Elektrofiltrski pepel v termoelektrarnah se odstranjuje po mokrem ali suhem postopku. Pri obeh postopkih se lastnosti elektrofiltrskega pepela spremenijo, kar povzroči različno reakcijo z alkalijami, torej sposobnost zeolitizacije. V raziskavi se je preučevalo fizikalne, kemične, mineraloške in morfološke lastnosti usedlin elektrofiltrskega pepela, zbrane v usedalnih bazenih in silosih termoelektrarne po hidrotermalni obdelavi. Preiskava z okoljskim vrstičnim elektronskim mikroskopom in rentgenska difrakcijska analiza usedlin sta pokazali, da ima pepel v silosu izredno dobro kationsko izmenjavo in visoko razmerje $\text{SiO}_2/\text{Al}_2\text{O}_3$ (SAR), kar ustreza tvorjenju večjih zeolitov elektrofiltrskega pepela v primerjavi z mokrim postopkom. Študija je pokazala, da se pepel v silosih boljše sintetizira v zeolite kot pepel v bazenih, da ga je količinsko več in da je boljše kakovosti.

ključne besede

reakcija z alkalijami, bazenski pepel, pepel v silosih, zeoliti elektrofiltrskega pepela

ZEOLITIZATION CHARACTERISTICS OF FLY ASHES FROM WET- AND DRY- DISPOSAL SYSTEMS

BHAGWANJEE JHA and D. N. SINGH

about the authors

Bhagwanjee Jha
Indian Institute of Technology Bombay,
Department of Civil Engineering
Powai, Mumbai-400076, India
E-mail: jha66b@iitb.ac.in

corresponding author

D. N. Singh
Indian Institute of Technology Bombay,
Department of Civil Engineering
Powai, Mumbai-400076, India
E-mail: dns@civil.iitb.ac.in

Abstract

The fly ash disposal at thermal power plants is either through wet- or dry-disposal systems. As these disposal practices result in different characteristics for the fly ashes, their interaction with alkalis, and hence the zeolitization potential, will be different. In order to demonstrate this, investigations were conducted to study the physical, chemical, mineralogical and morphological characteristics of the residues of the fly ashes collected from the lagoons and hoppers of the same thermal power plant, after their hydrothermal treatment. Field-emission-gun scanning electron microscopy and X-ray diffraction analysis of these residues demonstrated that the hopper ash attains an exceptionally high cation-exchange capacity and $\text{SiO}_2/\text{Al}_2\text{O}_3$ ratios (SAR), which correspond to the formation of major fly ash zeolites as compared to its counterpart. In other words, the study presented here helps to establish the superiority of hopper ash over lagoon ash for synthesizing fly ash zeolites and their enhanced quantity and quality.

keywords

alkali activation, lagoon ash, hopper ash, fly ash zeolites

1 INTRODUCTION

Several researchers have established the utility of fly ash as a raw material for the synthesis of zeolites, known

as fly ash zeolites (FAZs) [1-18]. However, the overall quality of the fly ash has been shown to be dependent on the type of disposal system (either wet- or dry- disposal) adopted by the power plants [6,7]. The hopper units of the electrostatic precipitators (i.e., the dry-disposal system of the fly ash) do not involve ash-water interaction, while, when fly ash is converted into a slurry for its storage in the ash ponds (or lagoons), the practice known as wet-disposal, such an interaction occurs over a prolonged period [19-21]. Though this ash-water interaction, known as zeolitization, has been studied by several researchers [6,7,19-21] in the past, not many efforts have been made to explore the influence of the disposal practices adopted at the same thermal power plant (TPP) on the zeolitization characteristics of the fly ash and the types of zeolites formed.

It has been shown by researchers that ash-water interaction results in an alteration of the physical, chemical, mineralogical and morphological characteristics of the fly ash [6,7]. Furthermore, these studies have highlighted the fact that the type of zeolites produced at the end of this interaction, their specific gravity, specific surface area, cation-exchange capacity, mineralogical and morphological phase transitions, depend upon the fly ash's composition and the ash-water interaction conditions [6,7]. Though these factors (uncertainties) are mainly responsible for generating the debate about the quality (grade) of the fly ash zeolites being produced at the end of the hydrothermal treatment, the influence of the source of fly ash (from wet- or dry-disposal systems) on the grade of fly ash zeolites cannot be ignored.

In such a scenario, it becomes prudent to establish the superiority of the fly ash collected from the two disposal systems, at the same thermal power plant (TPP) from which a better quality and quantity of the fly ash zeolites could be produced. With this in view, extensive investigations were conducted to characterize the physical, chemical, mineralogical and morphological characteristics of the fly ashes, and their residues after hydrothermal treatment, collected from a thermal power plant in India. Details of this study are presented here and it has

been demonstrated that the hydrothermal treatment of the fly ash collected from the hopper yields much better zeolites than its counterpart from the lagoon.

2 EXPERIMENTAL INVESTIGATIONS

Fly ash samples from the hoppers and lagoons of a thermal power plant in western Maharashtra, India, were collected over a period of several months. These samples have been designated as original hopper ash (OHA) and original lagoon ash (OLA). NaOH pellets supplied by Thomas Baker Ltd., Mumbai, India, were dissolved in the deionized water for the preparation of stock solutions of different molarity (0.5, 1.0, 2.0 and 3.5M). To ensure the alkali-ash interaction, the slurry of fly ash and the stock solutions were maintained at a liquid-to-solid ratio, L/S, of 10 ml/g [6]. This slurry was heated at 100°C in an open reflux system for different times, T , (= 12 to 48 hours, with an increment of 12 hours). The residues from this hydrothermal treatment designated as ALA and AHA (i.e., alkali activated lagoon ash and alkali activated hopper ash, respectively) were characterized for their specific gravity, chemical composition, cation-exchange capacity, mineralogy and morphology. Details of the methodology adopted for this purpose are described in the following sections. For the sake of clarity, the ALA and AHA samples are designated as described in Table 1.

2.1 DETERMINATION OF THE SPECIFIC GRAVITY

The specific gravity, G , of the samples was determined with the help of a Helium gas Ultra Pycnometer setup (Quantachrome, USA), as per the guidelines proposed by ASTM D 5550 [22]. This instrument helps in measuring the volume of helium gas displaced from the sample chamber for a known weight of the samples. Using this volume (which is equal to the volume of the sample) the specific gravity (the density with respect to water) of the

sample was computed and the results are shown in Fig. 1 for different ALA and AHA samples.

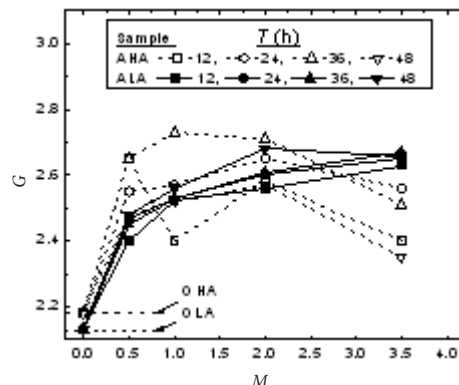


Figure 1. Variation in the specific gravity (G) and molarity (M) of the AHA and ALA samples.

2.2 DETERMINATION OF THE CHEMICAL COMPOSITION

An X-ray fluorescence (XRF) spectrometer was employed for the quantitative chemical analysis of the sample, in order to reveal the elements (as oxides by weight %) present in it. In accordance with ASTM C 618-03 [23], the XRF setup (Phillips 1410, Holland), a homogeneous mixture of 4 g of sample and 1 g of microcrystalline cellulose, dried by infrared radiations, was transferred to a standard sample holder made of aluminium (internal diameter 33 mm and height 12 mm). Thereafter, the filled sample holder was compressed by applying 15 tons of load through a hydraulic jack to the pellet, which is mounted on the spectrometer. Reference materials (i.e., Fly ash 2689, 2690, 2691, NIST, USA) were employed for the calibration of the spectrometer. The percentages of oxides present in the hopper and lagoon ashes (designated as OHA and OLA, respectively) are presented in Table 2. Also, the percentages of SiO_2 and Al_2O_3 and

Table 1. Sample designation for the treated ash samples (i.e., the residues).

M molarity	T hours							
	12	24	36	48	12	24	36	48
0.5	ALA1	ALA2	ALA3	ALA4	AHA1	AHA2	AHA3	AHA4
1.0	ALA5	ALA6	ALA7	ALA8	AHA5	AHA6	AHA7	AHA8
2.0	ALA9	ALA10	ALA11	ALA12	AHA9	AHA10	AHA11	AHA12
3.5	ALA13	ALA14	ALA15	ALA16	AHA13	AHA14	AHA15	AHA16

their ratio, designated as SAR, are presented in Table 3. It should be noted that SAR indicates the zeolitization potential of the ash and the cation-exchange capacity (CEC) of the residues [24], as discussed in the following.

Table 2. Chemical composition of the original fly ash samples.

Oxide	% by weight	
	OHA	OLA
SiO ₂	63.85	58.33
Al ₂ O ₃	26.05	27.10
Fe ₂ O ₃	5.14	5.02
SiO ₂ +Al ₂ O ₃ +Fe ₂ O ₃	95.04	90.45
Na ₂ O	0.06	0.22
K ₂ O	0.66	0.89
CaO	1.88	1.12
MgO	0.39	0.53
TiO ₂	1.52	1.63
P ₂ O ₅	0.16	0.24

2.3 DETERMINATION OF THE CEC

The cation-exchange capacity, CEC, of the ash sample was determined by adopting the following methodology [25]. A 3.2 g sample and 27 ml of 1N CH₃COONa solution were transferred to a polyvinyl bottle and this mixture was thoroughly shaken on a mechanical shaker for 5 min. This mixture was centrifuged until a clear solution was obtained and later decanted. This process was repeated twice to facilitate the saturation of the sample with Na⁺. Thereafter, the sample was mixed with 27 ml of 99% isopropyl alcohol and shaken for 5 min. This process ensures washing of the sample and the removal of all the organic matter from it. Centrifugation of this mixture yields a residue, which was rewashed twice. This process was followed by mixing the residue with 27 ml of 1N CH₃COONH₄ solution followed by shaking and centrifugation. To ensure the exchange of Na⁺ from the residue, its washing with ammonium acetate solution was repeated twice. Furthermore, the Na⁺ concentration in the solution was detected with the help of an Inductively Coupled Plasma-Atomic Emission Spectrometer (ICP-AES) and the CEC (in meq/100g) was calculated by employing Eq. (1). The results are shown in Fig. 2.

$$CEC = C \times (V / m) \times (100 / 1000) \quad (1)$$

where C is the concentration of Na⁺ (meq/l) in the solution obtained after the last three washings, V is the total volume of these solutions (in ml) and m is the mass of the dried sample (in g).

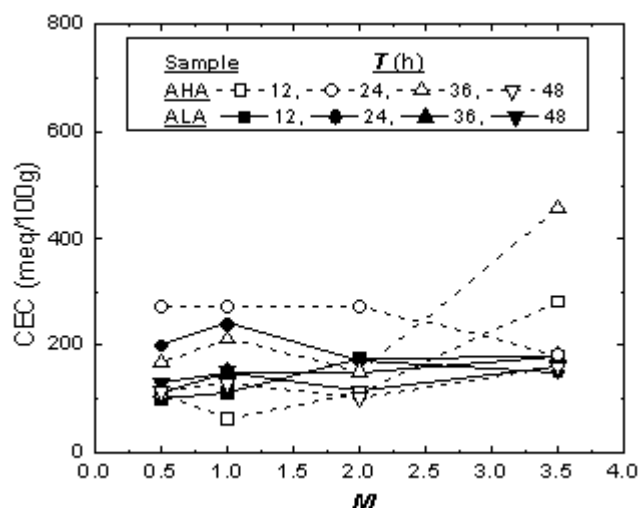


Figure 2. Variation in the CEC of the AHA and the ALA samples.

2.4 MINERALOGICAL STUDY

The XRD patterns of the OHA and AHA samples were determined with the help of a XRD set up (Phillips, Eindhoven, Netherlands), which is fitted with a graphite monochromator and employs Cu-K α radiation as the source. These samples were scanned for a diffraction angle ($2\theta^\circ$) ranging between 0 to 50° . The obtained XRD pattern (refer Fig. 3) was analysed and the minerals corresponding to each major peak were identified with the help of the search files presented by the Joint Committee on Powder Diffraction Standards (JCPDS, 1994) [26]. Accordingly, the mineralogical composition of the OLA [21] & OHA and superior ALA [21] & AHA samples were explored and the results are presented in Table 4.

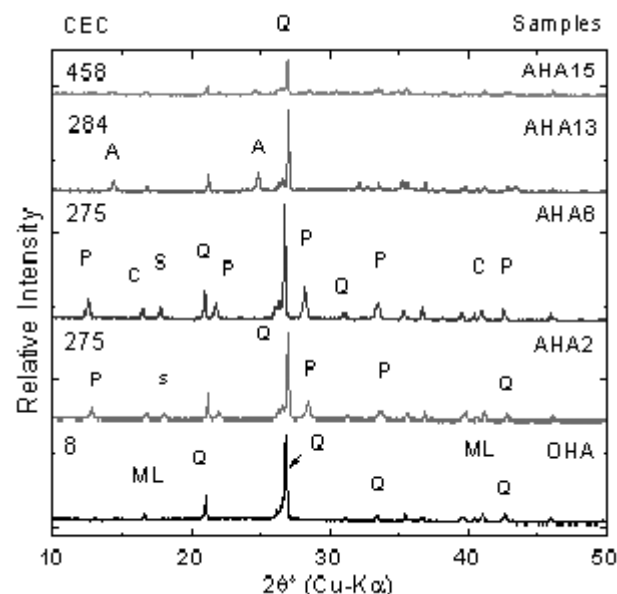


Figure 3. XRD patterns of the OHA and the superior AHA samples (where Q, ML, P, C, S and A represent quartz, mullite, zeolite Na-P1, cancrinite, hydroxysodalite and analcime, respectively).

Table 3. Silica and alumina oxides and their ratio in the fly ash samples.

Fly ash	Designation of the residue	SiO ₂	Al ₂ O ₃	SAR
		% by weight		
OHA	-	63.85	26.05	2.45
	AHA1	57.73	27.90	2.06
	AHA2	48.74	21.70	2.24
	AHA3	52.05	24.00	2.16
	AHA4	48.74	18.40	2.64
	AHA5	52.56	20.88	2.51
	AHA6	55.15	24.64	2.23
	AHA7	36.96	18.76	1.97
	AHA8	51.41	23.56	2.18
	AHA9	36.77	19.10	1.92
	AHA10	38.67	26.00	1.48
	AHA11	36.77	19.10	1.92
	AHA12	41.7	17.66	2.36
	AHA13	37.93	23.65	1.60
	AHA14	35.48	19.76	1.79
	AHA15	43.83	17.74	2.47
AHA16	28.12	14.30	1.96	
OLA	-	58.33	27.10	2.15
	ALA1	64.2	26.77	2.39
	ALA2	62.29	29.27	2.12
	ALA3	59.78	30.87	1.93
	ALA4	58.55	30.04	1.94
	ALA5	61.53	30.84	1.99
	ALA6	58.94	31.12	1.89
	ALA7	54.89	30.47	1.80
	ALA8	57.03	32.76	1.74
	ALA9	58.01	30.90	1.87
	ALA10	56.98	32.16	1.77
	ALA11	56.06	32.53	1.72
	ALA12	53.94	34.14	1.57
	ALA13	48.76	30.99	1.57
	ALA14	43.27	32.29	1.34
	ALA15	42.12	32.48	1.29
ALA16	40.59	32.20	1.26	

2.5 MORPHOLOGICAL STUDY

The morphological characteristics of these samples were studied by conducting an analysis with the help of a field-emission-gun scanning electron microscope (FEG-SEM) setup (JSM-7600F, Japan), which has a magnification ranging from 25 to 1,000,000. The micrographs of

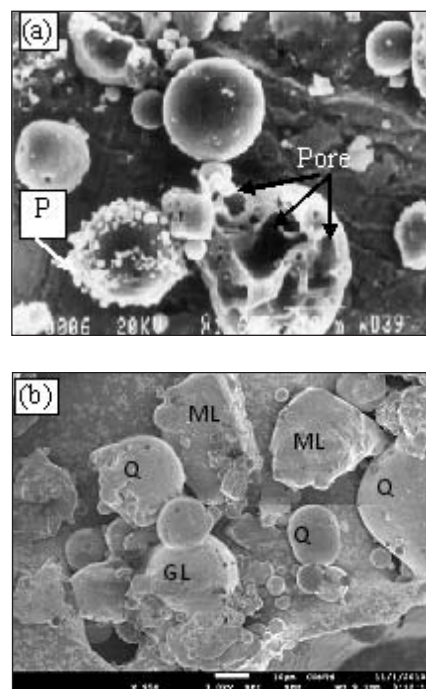


Figure 4. Micrographs of the samples (a) OLA and (b) OHA, where Q, ML, GL and P designate quartz, mullite, glass and zeolite Na-P1, respectively.

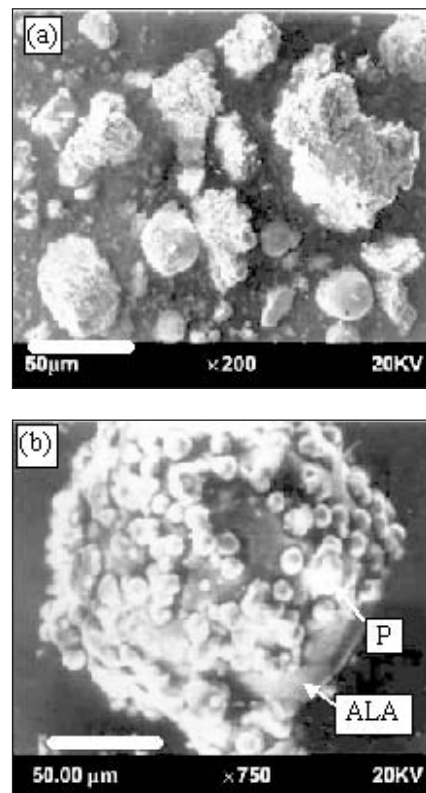


Figure 5. Micrographs of the superior residue, ALA6, at different magnifications (a) $\times 200$ and (b) $\times 750$.

the OLA and OHA are presented in Fig. 4. Likewise, the micrographs of a group of superior ALA and AHA samples (as per the high CEC values) were also obtained and the results are presented in Figs. 5 and 6 (a to f).

3 RESULTS AND DISCUSSION

3.1 VARIATION IN G

From Fig. 1 it is clear that the specific gravity, G , of the original hopper ash, OHA, ($=2.18$) is almost same as that of the original lagoon ash, OLA, ($=2.13$). Though, in general, G values for the ALA and AHA samples are seen

to increase with an increase in the molarity of the NaOH ($M \leq 2.0$), randomness in the value of G for the AHA with T is noticeable. Incidentally, the residues AHA7 (i.e., the hopper ash treated with 1 M NaOH solution for 36 hours) and ALA6 (i.e., the lagoon ash treated with 1 M NaOH solution for 24 hours), exhibit very high G values (2.73 and 2.53, respectively). The increase in G value can be attributed to the etching of the ash particles, which helps in the escape of entrapped air and gases from the inner regions of the fly ash particle, due to an alkali treatment [6,7]. On the other hand, treatment of the fly ash with high molar solutions (i.e., $M \geq 2.0$), results in a significant increment (up to 2.67) and reduction (up to 2.35) in the G values of the ALA and AHA samples,

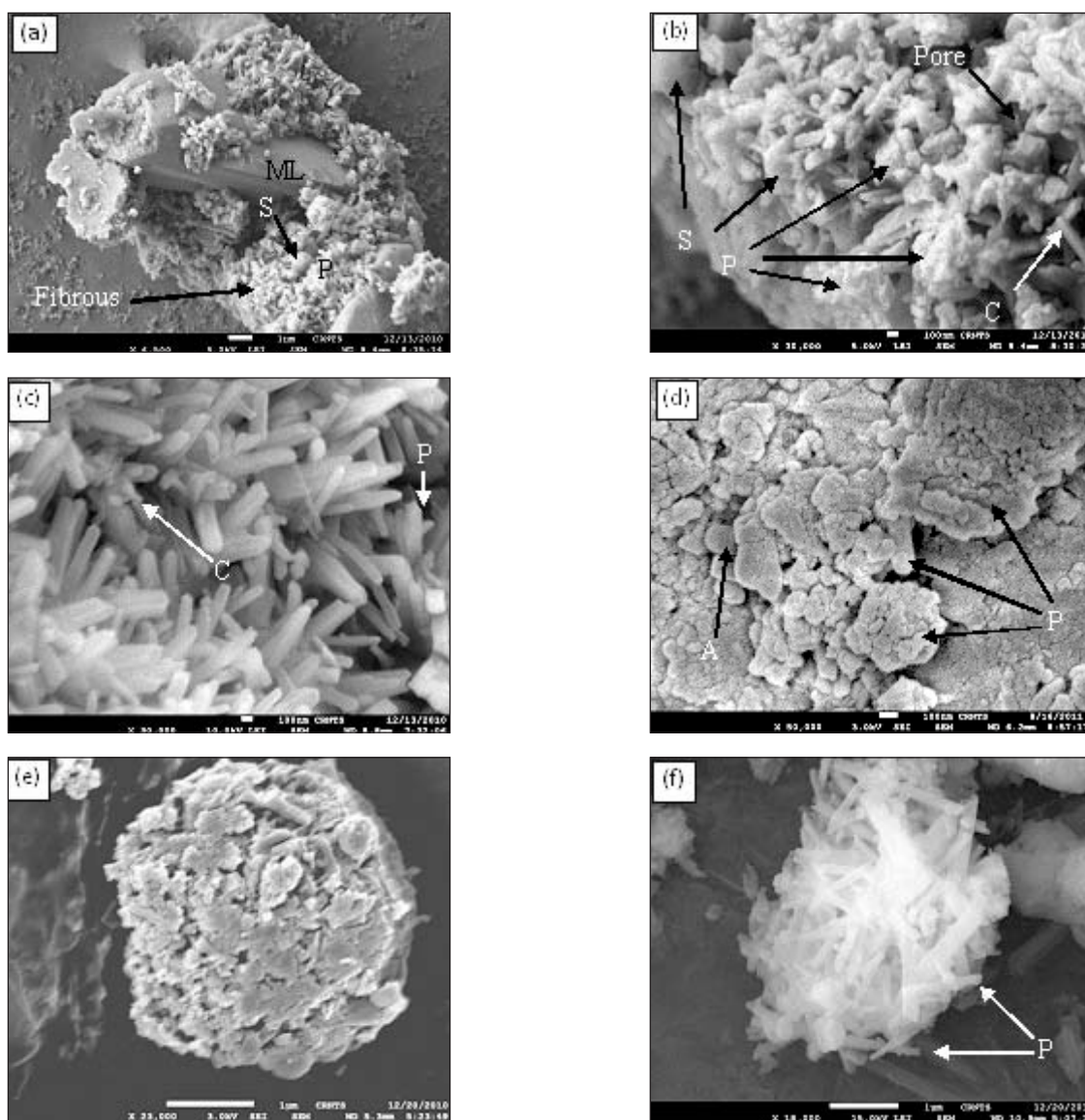


Figure 6. Micrographs of the residues (a) AHA6, $\times 6500$, (b) AHA6, $\times 30000$, (c) AHA2, $\times 30000$, (d) AHA15, $\times 50000$, (e) AHA13, $\times 23000$ and (f) AHA13, $\times 18000$, where P, C, S and A designate the zeolites Na-P1, cancrinite, hydroxysodalite and analcime, respectively.

respectively. This could be attributed to a gradual increase in the dissolution of the lighter ingredients (e.g., cenospheres) present in the lagoon ash, as compared to the hopper ash, for which the reaction is faster, even at lower molarities. Also, as depicted in Fig. 6, the AHA samples develop more internal pores, which justifies the increased zeolite formation and results in lower G values. The increased zeolite formation in AHA samples is also justified by the significant dissolution of SiO_2 (e.g., from 63.85%, for the OHA, to 36.96%, for AHA7, which is 27%) and Al_2O_3 (from 26.05%, to 18.76%, which is 7%). This dissolution of SiO_2 and Al_2O_3 also results in enhanced pores on the residue particles (see micrographs of the residues in Fig. 6).

3.2 VARIATION IN SAR

From Table 2 it can be observed that though both OHA and OLA belong to class F fly ash [23], as $\text{SiO}_2 + \text{Al}_2\text{O}_3 + \text{Fe}_2\text{O}_3$ is more than 70%, the percentage of SiO_2 in the OHA is higher by 5%, as compared to the OLA. This excess amount of SiO_2 in the OHA may be in the amorphous aluminosilicate glass phase, which is responsible for a higher silica dissolution, as shown in Table 3. From the data presented in the table, it is clear that the SAR of all the AHA samples is in the range 1.79–1.97, which matches well with the SAR value for the zeolites Na-P1 and analcime [27]. Such a reduced SAR (lower than 2.45 in the OHA) can be attributed to either a loss of SiO_2 or a gain of Al_2O_3 in these residues. This also indicates mineralogical and morphological transitions, which further enforces the probability of zeolitization of the OHA. In contrast, Table 3 also exhibits an increase in SiO_2 in some of the residues (i.e., ALA2 to ALA6) of the hopper ash, as compared to the lagoon ash. Also, Al_2O_3 has been noticed to be on the higher side, as compared to the OLA, in these samples except for the ALA1. However, such an increase in the oxides in the residues of OLA is unexpected and could not be substantiated, as neither SiO_2 nor Al_2O_3 were added externally. Hence, an extensive study is warranted to explore the chemistry involved in this entire process.

Furthermore, it can be inferred that the increase in Al_2O_3 in the ALA samples contributes to a significant lowering of their SAR up to 1.26 (refer Table 3). Also, a decrease in the SAR of the ALA samples with an increase in the M and T of the treatment may have some effects on their increasing G , as shown in Fig. 1. Thus, based on the SAR values, it can be concluded that the lagoon ash used in this study is a suitable material for the synthesis of a group of low-silica zeolites ($2 > \text{SAR} > 1.26$), such as Na-P1 and hydroxysodalite. Incidentally, these zeolites

have been identified from the XRD diffractograms of the samples, as presented in Table 3. This study also reveals the higher zeolitization potential of the OHA for synthesizing a class of zeolites with a slightly higher SAR value ($2.64 > \text{SAR} > 1.60$), which is responsible for the creation of the zeolites faujasite and analcime [27].

3.3 VARIATION IN THE CEC

The variation of the cation-exchange capacity (CEC) of the residues with respect to the molarity, M , is depicted in Fig. 2. It can be seen from this figure that the trends are not well defined, but the AHAs attain a higher CEC than the ALAs. This also confirms the higher zeolitization of the OHA, as compared to its counterpart. It should also be noted that some of the OHA residues (i.e., AHA3, AHA13 and AHA15) exhibit very high CEC values (275, 284 and 458 meq/100g, respectively).

3.4 CORRELATION BETWEEN CEC AND SAR

An attempt was made to develop a correlation between the CEC and SAR of the residues, as shown in Fig. 7. It is clear that, in general, the CEC decreases with an increase in SAR. However, the rate of this decrease (defined in terms of the slope of the relationship) is significantly rapid for the AHA, as compared to the ALA. This also demonstrates that the OHA is a much more active and suitable material to synthesize a higher grade of the cation exchanger (i.e., a zeolite) than the OLA. A combined trend for the ALA and AHA samples is also shown in the figure, which could be very useful for predicting the CEC of the activated flyashes if their SAR is known.

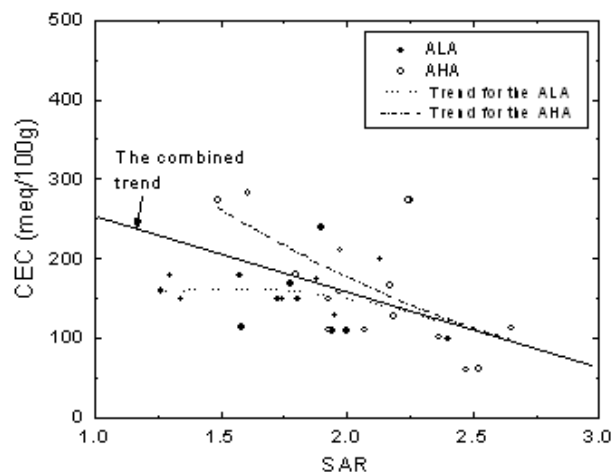


Figure 7. Correlations between CEC and SAR of the residues.

3.5 MINERALOGICAL ALTERATION

As listed in Table 4, the ALA samples contain zeolite Na-P1 and in addition the residue ALA6 exhibits the presence of the zeolite Na-P1 for $M \leq 1$ [21]. Incidentally, the zeolite hydroxysodalite appears in the residue for $M \geq 1$. These peaks match with the zeolites Na-P1 and hydroxysodalite in the residue AHA2. However, as listed in Table 4, the zeolites cancrinite and analcime were also found in the residue AHA6. This could be attributed to the disappearance of mullite and hence the enhanced zeolitization of the hopper ash. Also, newly formed peaks ($2\theta^\circ$ equal to 12.55° and 28.19°) exhibit an increase in the peak intensity with an increase in the molarity ($M \leq 1$) and for activation time ($T \leq 24$ hours). From the table it can be seen that the residue AHA13 exhibits two new and small peaks of zeolite analcime. Incidentally, these peaks and other peaks (present in the AHA15) disappear for a higher molarity and a longer activation time. As explained earlier, a high CEC (458 meq/100g) of the residue AHA15, indicates a highly fibrous, porous and soft grade (low intensity peaks, refer Fig. 3) of polycrystalline zeolites in the residue (refer Fig. 6). Furthermore, the presence of a little quartz and negligible mullite in the residue AHA15 reveals the suitability of the hopper ash for the synthesis of better fly ash zeolites.

3.6 MORPHOLOGICAL ALTERATIONS

From Fig. 4 (a,b) it can be seen that both OHA and OLA samples are enriched with spheroidal and oval particles, which may correspond to glass and quartz, respectively. However, Fig. 4(a) exhibits some whitish spherules (zeolite Na-P1 with large surface pores) deposited on the OLA samples, due to the ash-water interaction taking place in the lagoon [7,21,28]. In contrast, the micrograph of the OHA (as depicted in Fig. 4b), reveals many smooth and spherical (quartz, mullite) to irregular parti-

cles (carbon, hematite and/or magnetite) as reported by Adamczyk and Bialecka [1] and Nungteren et al. [5]. It can also be noted from Fig. 6(a) that a spherical particle, in AHA6, has been fully covered with zeolites. The majority of the fibrous and ball-shaped products (see Fig. 6a,b) are zeolite Na-P1 and hydroxysodalite, respectively [14,16]. Also, orthorhombic and cubic morphologies (see Fig. 6c,d) correspond to another grade of Na-P1 (with improved SAR and CEC, as shown in Table 3 and Fig. 6) and analcime. Also, some fine needle-shaped (cancrinite) morphology [24] can also be seen in Fig. 6(b,c). Above all, the cluster of whitish orthorhombic products formed in the AHA13 (see Fig. 6e,f) is exceptional and it confirms the significant zeolitization of the OHA samples. In addition, a large-scale development of the surface pores can be confirmed from Fig. 6(a to f), which in turn supports the high CEC of the AHA samples. In agreement with the XRD patterns (see Fig. 3), the formation of the zeolitic morphology corresponds to the appearance of new mineral peaks. Moreover, the micrographs of the AHA (corresponding to 3.5M NaOH and 36 hours of treatment as exhibited in Fig. 6d), reveal the synthesis of the majority of zeolite Na-P1 with large inter-particle pores and a high CEC up to 458 meq/100g (refer Figs. 2 and 6).

4 CONCLUSIONS

Based on the above observations and findings, the following can be concluded:

- The hopper ash, as compared to the lagoon ash, is rich in silica and hence a much more active material for dissolution by a hydrothermal treatment with NaOH.
- Hopper ash attains a higher cation-exchange capacity (270 to 458 meq/100g), silica alumina ratio and pores than the lagoon ash due to the treatment.

Table 4. Minerals identified in the fly ash and superior residues.

Mineral	OHA	OLA	AHA2	AHA6	ALA6	ALA9	ALA10	ALA11	AHA13	AHA15	ALA16
Quartz	✓✓✓				✓✓				✓	-	✓✓
Mullite	✓✓		✓	-		✓			-		✓
Na-P1 zeolite	-	✓		✓✓		✓		-	✓	✓✓	-
Hydroxysodalite			✓	-	✓				-		✓
Cancrinite		-		✓	-					-	
Analcime			-				-		✓		-

Note: predominant (✓✓✓), present (✓✓), traces (✓) and absent (-).

- The majority of the zeolite Na-P1 can be synthesized from hopper ash along with traces of zeolite hydroxysodalite, cancrinite and analcime by imparting the hydrothermal treatment of the ash using 1.0M to 3.5M NaOH and 24 to 36 hours of activation time).
- A combined trend derived between the cation-exchange capacity and the silica alumina ratio of an activated fly ash is found to be very useful for predicting its zeolitization potential.

ABBREVIATIONS

AHA	activated hopper ash
ALA	activated lagoon ash
CEC	cation-exchange capacity
FAZ	fly ash zeolites
FEG-SEM	field-emission-gun scanning electron microscopy
ICP-AES	inductively coupled plasma - atomic emission spectrometer
JCPDS	Joint Committee of Powder Diffraction Standards
NIST	National Institute of Standards and Technology
OHA	original hopper ash
OLA	original lagoon ash
SAR	silica alumina ratio
TPP	thermal power plant
XRD	X-ray diffraction spectrometer
XRF	X-ray fluorescence spectrometer

SYMBOLS

C	concentration (in mg/l)
G	specific gravity
L	liquid
S	solid
M	molarity of NaOH
m	mass (in g)
T	duration of treatment (in hours)
θ	diffraction angle
V	volume (in ml)

REFERENCES

- [1] Adamczyk, Z., Biaćka, B. (2005). Hydrothermal synthesis of zeolites from polish coal fly ash. *Polish J. of Environ. Stud.*, Vol. 14, No. 6, pp. 713-719.
- [2] Hollman, G.G., Steenbruggen, G., Janssen-Jurkovicov, M. (1999). A two-step process for the synthesis of zeolites from coal fly ash. *Fuel*, Vol. 78, No. 10, pp. 1225-1230.
- [3] Murayama, N., Yamamoto, H., Shibata, J. (2002). Mechanism of zeolite synthesis from coal fly ash by alkali hydrothermal reaction, *Int. J. Miner. Process*, Vol. 64, No. 1, pp. 1-17.
- [4] Inada, M., Eguchi, Y., Enomoto, N., Hojo, J. (2005). Synthesis of zeolite from coal fly ashes with different silica-alumina composition. *Fuel*, Vol. 84, No. 2-3, pp. 299-304.
- [5] Nungterren, H.W., Moreno, N., Sebastia E., Querol, X. (2001). Determination of the available Si and Al from coal fly ashes under alkaline conditions with the aim of synthesizing zeolite products. *International Ash Utilization Symposium, Centre for Applied Energy Research, University of Kentucky*, Paper No. 71.
- [6] Scott, J., Guang, D., Naeramitmansuk, K., Thabuot, M., Amal, R. (2001). Zeolite synthesis from coal fly ash for the removal of lead ions from aqueous solution. *J. Chem. Technol. Biotechnol.*, Vol. 77, pp. 63-69.
- [7] Kolay, P.K., Singh, D.N. (2002). Characterization of alkali activated lagoon ash and its application for heavy metal retention. *Fuel*, Vol. 81, No. 4, pp. 483-489.
- [8] Kolay, P.K., Singh, D.N. (2001a). Effect of zeolitization on physicochemico-mineralogical and geotechnical properties of the lagoon ash. *Can. Geotech. J.*, Vol. 38, No. 5, pp. 1105-1112.
- [9] Ma, W., Brown, P.W., Komarneni, S. (1998). Characterization and cation exchange properties of zeolites synthesized from flyashes. *J. Mater. Res.*, Vol. 13, No. 1, pp. 3-7.
- [10] Mimura, H., Yokota, K., Akiba, K., Onodera, Y. (2001). Alkali hydrothermal synthesis of zeolites from coal flyash and their uptake properties of Cesium ion. *J. of Nucl. Sci. and Technol.*, Vol. 38, No. 9, pp. 766-772.
- [11] Rayalu, S., Meshram, S.U., Hasan, M.Z. (2000). Highly crystalline faujasitic zeolites from flyash. *J. of Hazard. Mater.*, Vol. 77, No. 1-3, pp. 123-131.
- [12] Rayalu, S.S., Bansiwala, A.K., Meshram, S.U., Labhsetwar, N., Devotta, S. (2006). Fly ash based zeolite analogues: versatile materials for energy and environment conservation. *Catal. Surveys from Asia*, Vol. 10, No. 2, pp. 74-88.
- [13] Querol, X., Moreno, N., Uman, J.C., Alastuey, A., Hernandez, E., Lopez-Soler, A., Plana, F. (2002). Synthesis of zeolites from coal fly ash: an overview. *Int. J. of Coal Geology*, Vol. 50, No. 1-4, pp. 413-423.
- [14] Rios, C.A.R., Williams, C.D., Roberts, C.L. (2009). A comparative study of two methods for the synthesis of fly ash-based sodium and potassium type zeolites. *Fuel*, Vol. 88, No. 8, pp. 1403-1416.

- [15] Fukui, K., Nishimoto, T., Takiguchi, M., Yoshida, H. (2003). Effects of NaOH concentration on zeolite synthesis from fly ash with a hydrothermal treatment method. *J. Soc. Powder Technol.*, Vol. 40, pp. 497-504.
- [16] Zeng, R., Umana, J.C., Querol, X., Lopez-Soal, A., Plana, F., Zhuang, X. (2002). Zeolite synthesis from a high Si-Al fly ash from east China. *J. of Chem. Technol. and Biotechnol.*, Vol. 77, pp. 267-273.
- [17] Kim, W., Seung-Hoon, Ahn B.J. (1997). Synthesis of Na-P1 zeolite from coal fly ash. *J. of the Ind. Eng. Chem.*, Vol. 3, No. 3, pp. 185-190.
- [18] Querol, X., Moreno, N., Alastuey, A., Juan, R., Andres, J.M., Lopez-Soler, A., Ayora, C., Medinaceli, A., Valero, A. (2007). Synthesis of high ion exchange zeolites from coal fly ash. *Geol. Acta*, Vol. 5, No. 1, pp. 49-57.
- [19] Singh, D.N., Kolay, P.K. (2002). Simulation of ash water interaction and its influence on ash characteristics. *Prog. in Energy and Combust. Sci.*, Vol. 28, No. 3, pp. 267-299.
- [20] Kolay, P.K., Singh, D.N. (2001c). Physical, chemical, mineralogical and thermal properties of cenospheres from a ash lagoon, *Cem. and Concr. Res.*, Vol. 31, No. 4, pp. 539-542.
- [21] Kolay, P.K., Singh, D.N., Murti M.V.R. (2001). Synthesis of zeolites from lagoon ash. *Fuel*, Vol. 80, No. 5, pp. 739-745.
- [22] ASTM D5550-06 Standard Test Method for Specific Gravity of Soil Solids by Gas Pycnometer, West Conshohocken, United States.
- [23] ASTM C618-12 Standard Specification for Coal Fly Ash and Raw or Calcined Natural Pozzolan for Use in Concrete, West Conshohocken, USA.
- [24] Wang, H., Pinnavaia, T.J. (2006). MFI zeolite with small and uniform intracrystal mesopores. *Angew. Chem. Int. Ed.*, Vol. 45, No. 45, pp. 7603-7606.
- [25] International soil reference and information centre, Droevendaalsesteeg 3, 6708 PB Wageningen, Building 101, PO Box 353, 6700 AJ Wageningen, Netherlands.
- [26] Joint committee on powder diffraction standards. (1994), Philadelphia-19103.
- [27] Lobo, R.F. (2003). Handbook of zeolite science and technology, chapter- 3, Introduction to structural chemistry of zeolites, University of Delaware, Newark, Delaware, U.S.A, ISBN-10: 0824740203 | ISBN-13: 978-0824740207
- [28] Fazio, A.D., Brotzu, P., Ghiara, M.R., Fercia, M.L., Lonis, R., and Sau, A. (2008). Hydrothermal treatment at low temperature of Sardinian clinoptilolite bearing ignimbrites for increasing cation exchange capacity. *Per. Miner.*, Vol. 77, pp. 79-91.

NAVODILA AVTORJEM

VSEBINA ČLANKA

Članek naj bo napisan v naslednji obliki:

- Naslov, ki primerno opisuje vsebino članka in ne presega 80 znakov.
- Izvleček, ki naj bo skrajšana oblika članka in naj ne presega 250 besed. Izvleček mora vsebovati osnove, jedro in cilje raziskave, uporabljeno metodologijo dela, povzetek izidov in osnovne sklepe.
- Največ 6 ključnih besed, ki bi morale biti napisane takoj po izvlečku.
- Uvod, v katerem naj bo pregled novejšega stanja in zadostne informacije za razumevanje ter pregled izidov dela, predstavljenih v članku.
- Teorija.
- Eksperimentalni del, ki naj vsebuje podatke o postavitvi preiskusa in metode, uporabljene pri pridobitvi izidov.
- Izidi, ki naj bodo jasno prikazani, po potrebi v obliki slik in preglednic.
- Razprava, v kateri naj bodo prikazane povezave in posplošitve, uporabljene za pridobitev izidov. Prikazana naj bo tudi pomembnost izidov in primerjava s poprej objavljenimi deli.
- Sklepi, v katerih naj bo prikazan en ali več sklepov, ki izhajajo iz izidov in razprave.
- Vse navedbe v besedilu morajo biti na koncu zbrane v seznamu literature, in obratno.

datne zahteve

- Vrstice morajo biti zaporedno oštevilčene.
- Predložen članek ne sme imeti več kot 18 strani (brez tabel, legend in literature); velikost črk 12, dvojni razmik med vrsticami. V članek je lahko vključenih največ 10 slik. Isti rezultati so lahko prikazani v tabelah ali na slikah, ne pa na oba načina.
- Potrebno je priložiti imena, naslove in elektronske naslove štirih potencialnih recenzentov članka. Urednik ima izključno pravico do odločitve, ali bo te predloge upošteval.

ENOTE IN OKRAJŠAVE

V besedilu, preglednicah in slikah uporabljajte le standardne označbe in okrajšave SI. Simbole fizikalnih veličin v besedilu pišite poševno (npr. v , T itn.). Simbole enot, ki so sestavljene iz črk, pa pokončno (npr. Pa, m itn.). Vse okrajšave naj bodo, ko se prvič pojavijo, izpisane v celoti.

SLIKE

Slike morajo biti zaporedno oštevilčene in označene, v besedilu in podnaslovu, kot sl. 1, sl. 2 itn. Posnete naj

bodo v katerem koli od razširjenih formatov, npr. BMP, JPG, GIF. Za pripravo diagramov in risb priporočamo CDR format (CorelDraw), saj so slike v njem vektorske in jih lahko pri končni obdelavi preprosto povečujemo ali pomanjšujemo.

Pri označevanju osi v diagramih, kadar je le mogoče, uporabite označbe veličin (npr. v , T itn.). V diagramih z več krivuljami mora biti vsaka krivulja označena. Pomen oznake mora biti razložen v podnapisu slike.

Za vse slike po fotografskih posnetkih je treba priložiti izvirne fotografije ali kakovostno narejen posnetek.

PREGLEDNICE

Preglednice morajo biti zaporedno oštevilčene in označene, v besedilu in podnaslovu, kot preglednica 1, preglednica 2 itn. V preglednicah ne uporabljajte izpisanih imen veličin, ampak samo ustrezne simbole. K fizikalnim količinam, npr. t (pisano poševno), pripišite enote (pisano pokončno) v novo vrsto brez oklepajev. Vse opombe naj bodo označene z uporabo dvignjene številke¹.

SEZNAM LITERATURE

navedba v besedilu

Vsaka navedba, na katero se sklicujete v besedilu, mora biti v seznamu literature (in obratno). Neobjavljeni rezultati in osebne komunikacije se ne priporočajo v seznamu literature, navedejo pa se lahko v besedilu, če je nujno potrebno.

oblika navajanja literature

V besedilu: Navedite reference zaporedno po številkah v oglatih oklepajih v skladu z besedilom. Dejanski avtorji so lahko navedeni, vendar mora obvezno biti podana referenčna številka.

Primer: »..... kot je razvidno [1,2]. Brandl and Blovsky [4], sta pridobila drugačen rezultat...«

V seznamu: Literaturni viri so oštevilčeni po vrstnem redu, kakor se pojavijo v članku. Označimo jih s številkami v oglatih oklepajih.

Sklicevanje na objave v revijah:

- [1] Desai, C.S. (2007). Unified DSC constitutive model for pavement materials with numerical implementation. *Int. J. of Geomech.*, Vol. 7, No. 2, pp. 83-101.

Sklicevanje na knjigo:

- [2] Šuklje, L. (1969). Rheological aspects of soil mechanics. Wiley-Interscience, London

Sklicevanje na poglavje v monografiji:

- [3] Mettam, G.R., Adams, L.B., 1999. How to prepare an electronic version of your article, in: Jones, B.S., Smith, R.Z. (Eds.), Introduction to the Electronic Age. E-Publishing Inc., New York, pp. 281–304.

Sklicevanje na objave v zbornikih konferenc:

- [4] Brandl, H. and Blovsky, S. (2005). Slope stabilization with socket walls using the observational method. *Proc. Int. conf. on Soil Mechanics and Geotechnical Engineering, Bratislava*, pp. 2485-2488.

Sklicevanje na spletne objave:

- [5] Kot najmanj, je potrebno podati celoten URL. Če so poznani drugi podatki (DOI, imena avtorjev, datumi, sklicevanje na izvirno literaturo), se naj prav tako dodajo.

PODATKI O AVTORJIH

Članku priložite tudi podatke o avtorjih: imena, nazive, popolne poštne naslove, številke telefona in faksa,

naslove elektronske pošte. Navedite kontaktno osebo.

SPREJEM ČLANKOV IN AVTORSKE PRAVICE

Uredništvo si pridržuje pravico do odločanja o sprejemu članka za objavo, strokovno oceno mednarodnih recenzentov in morebitnem predlogu za krajšanje ali izpopolnitev ter terminološke in jezikovne korekture. Z objavo preidejo avtorske pravice na revijo ACTA GEOTECHNICA SLOVENICA. Pri morebitnih kasnejših objavah mora biti AGS navedena kot vir.

Vsa nadaljnja pojasnila daje:

Uredništvo
ACTA GEOTECHNICA SLOVENICA
Univerza v Mariboru,
Fakulteta za gradbeništvo
Smetanova ulica 17, 2000 Maribor, Slovenija
E-pošta: ags@uni-mb.si

INSTRUCTIONS FOR AUTHORS

FORMAT OF THE PAPER

The paper should have the following structure:

- A Title, which adequately describes the content of the paper and should not exceed 80 characters;
- An Abstract, which should be viewed as a mini version of the paper and should not exceed 250 words. The Abstract should state the principal objectives and the scope of the investigation and the methodology employed; it should also summarise the results and state the principal conclusions;
- Immediately after the abstract, provide a maximum of 6 keywords;
- An Introduction, which should provide a review of recent literature and sufficient background information to allow the results of the paper to be understood and evaluated;
- A Theoretical section;
- An Experimental section, which should provide details of the experimental set-up and the methods used to obtain the results;
- A Results section, which should clearly and concisely present the data, using figures and tables where appropriate;
- A Discussion section, which should describe the relationships shown and the generalisations made possible by the results and discuss the significance of the results, making comparisons with previously published work;

- Conclusions, which should present one or more conclusions that have been drawn from the results and subsequent discussion;
- A list of References, which comprises all the references cited in the text, and vice versa.

Additional requirements for manuscripts

- Use double line-spacing.
- Insert continuous line numbering.
- The submitted text of Research Papers should cover no more than 18 pages (without Tables, Legends, and References, style: font size 12, double line spacing). The number of illustrations should not exceed 10. Results may be shown in tables or figures, but not in both of them.
- Please submit, with the manuscript, the names, addresses and e-mail addresses of four potential referees. Note that the editor retains the sole right to decide whether or not the suggested reviewers are used.

UNITS AND ABBREVIATIONS

Only standard SI symbols and abbreviations should be used in the text, tables and figures. Symbols for physical quantities in the text should be written in Italics (e.g. v , T , etc.). Symbols for units that consist of letters should be in plain text (e.g. Pa, m, etc.). All abbreviations should be spelt out in full on first appearance.

FIGURES

Figures must be cited in consecutive numerical order in the text and referred to in both the text and the caption as Fig. 1, Fig. 2, etc. Figures may be saved in any common format, e.g. BMP, JPG, GIF. However, the use of CDR format (CorelDraw) is recommended for graphs and line drawings, since vector images can be easily reduced or enlarged during final processing of the paper.

When labelling axes, physical quantities (e.g. v , T , etc.) should be used whenever possible. Multi-curve graphs should have individual curves marked with a symbol; the meaning of the symbol should be explained in the figure caption. Good quality black-and-white photographs or scanned images should be supplied for the illustrations.

TABLES

Tables must be cited in consecutive numerical order in the text and referred to in both the text and the caption as Table 1, Table 2, etc. The use of names for quantities in tables should be avoided if possible: corresponding symbols are preferred. In addition to the physical quantity, e.g. t (in Italics), units (normal text), should be added on a new line without brackets.

Any footnotes should be indicated by the use of the superscript¹.

LIST OF REFERENCES

citation in text

Please ensure that every reference cited in the text is also present in the reference list (and vice versa). Any references cited in the abstract must be given in full. Unpublished results and personal communications are not recommended in the reference list, but may be mentioned in the text, if necessary.

reference style

Text: Indicate references by number(s) in square brackets consecutively in line with the text. The actual authors can be referred to, but the reference number(s) must always be given:

Example: "... as demonstrated [1,2]. Brandl and Blovsky [4] obtained a different result ..."

List: Number the references (numbers in square brackets) in the list in the order in which they appear in the text.

Reference to a journal publication:

- [1] Desai, C.S. (2007). Unified DSC constitutive model for pavement materials with numerical implementation. *Int. J. of Geomech.*, Vol. 7, No. 2, pp. 83-101.

Reference to a book:

- [2] Šuklje, L. (1969). Rheological aspects of soil mechanics. Wiley-Interscience, London

Reference to a chapter in an edited book:

- [3] Mettam, G.R., Adams, L.B. (1999). How to prepare an electronic version of your article, in: Jones, B.S., Smith, R.Z. (Eds.), Introduction to the Electronic Age. E-Publishing Inc., New York, pp. 281-304.

Conference proceedings

- [4] Brandl, H. and Blovsky, S. (2005). Slope stabilization with socket walls using the observational method. *Proc. Int. conf. on Soil Mechanics and Geotechnical Engineering, Bratislava*, pp. 2485-2488.

Web references:

- [5] As a minimum, the full URL should be given and the date when the reference was last accessed. Any further information, if known (DOI, author names, dates, reference to a source publication, etc.), should also be given.

AUTHOR INFORMATION

The following information about the authors should be enclosed with the paper: names, complete postal addresses, telephone and fax numbers and E-mail addresses. Indicate the name of the corresponding author.

ACCEPTANCE OF PAPERS AND COPYRIGHT

The Editorial Committee of the Slovenian Geotechnical Review reserves the right to decide whether a paper is acceptable for publication, to obtain peer reviews for the submitted papers, and if necessary, to require changes in the content, length or language.

On publication, copyright for the paper shall pass to the ACTA GEOTECHNICA SLOVENICA. The AGS must be stated as a source in all later publication.

For further information contact:

Editorial Board
ACTA GEOTECHNICA SLOVENICA
University of Maribor,
Faculty of Civil Engineering
Smetanova ulica 17, 2000 Maribor, Slovenia
E-mail: ags@uni-mb.si

NAMEN REVIJE

Namen revije ACTA GEOTECHNICA SLOVENICA je objavljanje kakovostnih teoretičnih člankov z novih pomembnih področij geomehanike in geotehnike, ki bodo dolgoročno vplivali na temeljne in praktične vidike teh področij.

ACTA GEOTECHNICA SLOVENICA objavlja članke s področij: mehanika zemljin in kamnin, inženirska geologija, okoljska geotehnika, geosintetika, geotehnične konstrukcije, numerične in analitične metode, računalniško modeliranje, optimizacija geotehničnih konstrukcij, terenske in laboratorijske preiskave.

Revija redno izhaja dvakrat letno.

AVTORSKE PRAVICE

Ko uredništvo prejme članek v objavo, prosi avtorja(je), da prenese(jo) avtorske pravice za članek na izdajatelja, da bi zagotovili kar se da obsežno razširjanje informacij. Naša revija in posamezni prispevki so zaščiteni z avtorskimi pravicami izdajatelja in zanje veljajo naslednji pogoji:

fotokopiranje

V skladu z našimi zakoni o zaščiti avtorskih pravic je dovoljeno narediti eno kopijo posameznega članka za osebno uporabo. Za naslednje fotokopije, vključno z večkratnim fotokopiranjem, sistematičnim fotokopiranjem, kopiranjem za reklamne ali predstavitvene namene, nadaljnjo prodajo in vsemi oblikami nedobičkonosne uporabe je treba pridobiti dovoljenje izdajatelja in plačati določen znesek.

Naročniki revije smejo kopirati kazalo z vsebino revije ali pripraviti seznam člankov z izvlečki za rabo v svojih ustanovah.

elektronsko shranjevanje

Za elektronsko shranjevanje vsakršnega gradiva iz revije, vključno z vsemi članki ali deli članka, je potrebno dovoljenje izdajatelja.

ODGOVORNOST

Revija ne prevzame nobene odgovornosti za poškodbe in/ali škodo na osebah in na lastnini na podlagi odgovornosti za izdelke, zaradi malomarnosti ali drugače, ali zaradi uporabe kakršnekoli metode, izdelka, navodil ali zamisli, ki so opisani v njej.

AIMS AND SCOPE

ACTA GEOTECHNICA SLOVENICA aims to play an important role in publishing high-quality, theoretical papers from important and emerging areas that will have a lasting impact on fundamental and practical aspects of geomechanics and geotechnical engineering.

ACTA GEOTECHNICA SLOVENICA publishes papers from the following areas: soil and rock mechanics, engineering geology, environmental geotechnics, geosynthetic, geotechnical structures, numerical and analytical methods, computer modelling, optimization of geotechnical structures, field and laboratory testing.

The journal is published twice a year.

COPYRIGHT

Upon acceptance of an article by the Editorial Board, the author(s) will be asked to transfer copyright for the article to the publisher. This transfer will ensure the widest possible dissemination of information. This review and the individual contributions contained in it are protected by publisher's copyright, and the following terms and conditions apply to their use:

photocopying

Single photocopies of single articles may be made for personal use, as allowed by national copyright laws. Permission of the publisher and payment of a fee are required for all other photocopying, including multiple or systematic copying, copying for advertising or promotional purposes, resale, and all forms of document delivery.

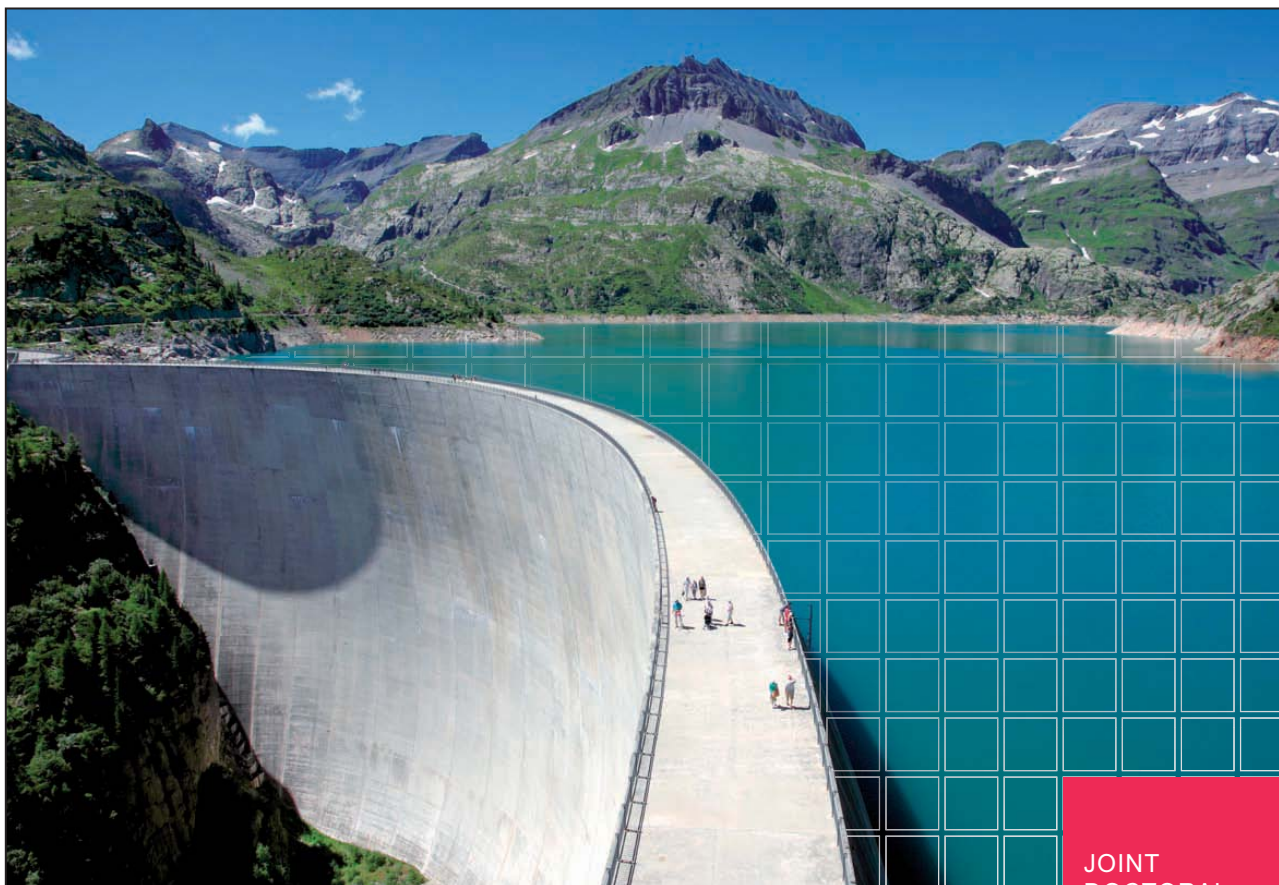
Subscribers may reproduce tables of contents or prepare lists of papers, including abstracts for internal circulation, within their institutions.

electronic storage

Permission of the publisher is required to store electronically any material contained in this review, including any paper or part of the paper.

RESPONSIBILITY

No responsibility is assumed by the publisher for any injury and/or damage to persons or property as a matter of product liability, negligence or otherwise, or from any use or operation of any methods, products, instructions or ideas contained in the material herein.



Graz University of Technology | University of Zagreb | University of Maribor | Budapest University of Technology and Economics

JOINT
DOCTORAL
PROGRAMME

Geo-Engineering and Water Management



Geo-Engineering and Water Management is a doctoral programme offered jointly by: Graz University of Technology, University of Zagreb, and in cooperation with University of Maribor and Budapest University of Technology and Economics.

The idea for this collaboration was born in a research project between Graz (Austria – Prof. Harald Kainz), Varaždin (Croatia – Prof. Božidar Biondić) and Maribor (Slovenia – Prof. Ludvik Trauner) within the research network “K-net Wasser”. To strengthen the cooperation between the universities, the establishment of a Joint Doctoral Programme was proposed. This programme offers an intense collaboration on teacher and student level. In addition, it allows doctoral students to attend specialised courses in their field of expertise in the scope of Joint Schools.

Programme Description

Doctoral students from the participating universities can apply for admission to the Joint Doctoral Programme. Students first have to fulfill all requirements for admission to the Doctoral/PhD Programme in the field of Geo-Engineering or Water Management at their home university. These requirements vary between the participating universities. In addition, the Study Council of the Joint Doctoral Programme – composing of professors and students from the participating units – decides on the final admission to the Joint Doctoral Programme. Languages of instruction: German / Hungarian / Slovenian / Croatian / English for the national part, English for the joint part of the curriculum and the doctoral thesis. Core of the Joint Doctoral Programme are the Joint Schools (Winter and Summer Schools), which will be organised twice a year (February and July) in turns at the participating universities. The host institution of the Joint School will arrange the accommodation for the incoming students and teachers.

PARTNERS OF THE JOINT DOCTORAL PROGRAMME Geo-Engineering and Water Management



Graz University of Technology
Coordinator
Rechbauerstrasse 12, 8010 - Graz, Austria



University of Zagreb
Trg maršala Tita 14, 10000 - Zagreb, Croatia



University of Maribor
Slomškov trg 15, 2000 - Maribor, Slovenia



Budapest University of Technology and Economics
Muegyetem rkp. 3., 1111 - Budapest, Hungary

Benefits and expected results

- Specialised courses offered in the Joint Schools
- International collaboration of teachers and PhD students in South-Eastern Europe
- Exchange in research and teaching
- Award of doctoral degree by their home university which is specific to each partner university; degrees will be recognised by all partners as equivalent

Scholarship

The participating universities are currently exploring scholarship possibilities for students attending the Joint Schools. Students applying for the Joint Schools will be informed about financial support available in due time. The consortium intends to make use of European and national funding schemes as well as financial support provided by the universities themselves.

Fact-Box

• Programme duration:

*Twice a year for 1 month
(4 ½ weeks) each.
Each student has to attend
3 Joint Schools.*

• Academic recognition:

*Award of the doctoral degree by
the home university, full academic
recognition by all partners as
equivalent.*

• Admission:

*For enrolment to the Doctoral/
PhD Programme, acceptance by the
Study Council and admission at the
home university are required.*

More information on:
▶ www.jdp.tugraz.at